STARS

University of Central Florida
STARS

Electronic Theses and Dissertations, 2004-2019

2010

Fundamental Study Of Mechanical And Chemical Degradation Mechanisms Of Pem Fuel Cell Membranes

Wonseok Yoon
University of Central Florida

Part of the Mechanical Engineering Commons

Find similar works at: https://stars.library.ucf.edu/etd

University of Central Florida Libraries http://library.ucf.edu

This Doctoral Dissertation (Open Access) is brought to you for free and open access by STARS. It has been accepted for inclusion in Electronic Theses and Dissertations, 2004-2019 by an authorized administrator of STARS. For more information, please contact STARS@ucf.edu.

STARS Citation

Yoon, Wonseok, "Fundamental Study Of Mechanical And Chemical Degradation Mechanisms Of Pem Fuel Cell Membranes" (2010). *Electronic Theses and Dissertations, 2004-2019*. 4205.
https://stars.library.ucf.edu/etd/4205

Showcase of Text, Archives, Research & Scholarship

www.manaraa.com

FUNDAMENTAL STUDY OF MECHANICAL AND CHEMICAL DEGRADATION MECHANISMS OF PEM FUEL CELL MEMBRANES

by

WONSEOK YOON
B.S. Hongik University, 1998
M.S. Seoul National University, 2005

A dissertation submitted in partial fulfillment of the requirements
for the degree of Doctor of Philosophy
in the Department of Mechanical, Materials, and Aerospace Engineering
in the College of Engineering & Computer Science
at the University of Central Florida
Orlando, Florida

Spring Term
2010

Major Professor: Xinyu Huang

www.manaraa.com

ABSTRACT

One of the important factors determining the lifetime of polymer electrolyte membrane fuel cells (PEMFCs) is membrane degradation and failure. The lack of effective mitigation methods is largely due to the currently very limited understanding of the underlying mechanisms for mechanical and chemical degradations of fuel cell membranes.

In order to understand degradation of membranes in fuel cells, two different experimental approaches were developed; one is fuel cell testing under open circuit voltage (OCV) with bi-layer configuration of the membrane electrode assemblies (MEAs) and the other is a modified gas phase Fenton's test.

Accelerated degradation tests for polymer electrolyte membrane (PEM) fuel cells are frequently conducted under open circuit voltage (OCV) conditions at low relative humidity (RH) and high temperature. With the bi-layer MEA technique, it was found that membrane degradation is highly localized across thickness direction of the membrane and qualitatively correlated with location of platinum (Pt) band through mechanical testing, Infrared (IR) spectroscopy, fluoride emission, scanning electron microscopy (SEM), transmission electron microscopy (TEM), and energy dispersive spectroscopy (EDS) measurement.

One of the critical experimental observations is that mechanical behavior of membranes subjected to degradation via Fenton's reaction exhibit completely different behavior with that of membranes from the OCV testing. This result led us to believe that

other critical factors such as mechanical stress may affect on membrane degradation and therefore, a modified gas phase Fenton's test setup was developed to test the hypothesis. Interestingly, the results showed that mechanical stress directly accelerates the degradation rate of ionomer membranes, implying that the rate constant for the degradation reaction is a function of mechanical stress in addition to commonly known factors such as temperature and humidity.

Membrane degradation induced by mechanical stress necessitates the prediction of the stress distribution in the membrane under various conditions. One of research focuses was on the developing micromechanism-inspired continuum model for ionomer membranes. The model is the basis for stress analysis, and is based on a hyperelastic model with reptation-inspired viscous flow rule and multiplicative decomposition of viscoelastic and plastic deformation gradient. Finally, evaluation of the membrane degradation requires a fuel cell model since the degradation occurs under fuel cell operating conditions. The fuel cell model included structural mechanics models and multiphysics models which represents other phenomena such as gas and water transport, charge conservation, electrochemical reactions, and energy conservation. The combined model was developed to investigate the compression effect on fuel cell performance and membrane stress distribution.

ACKNOWLEDGMENTS

TABLE OF CONTENTS

LIST OF FIGURES

LIST OF TABLES

LIST OF SYMBOLS

u	superficial velocity in x direction
v	superficial velocity in y direction
x	x-direction, through-plane
y	y-direction, in-plane
p	pressure(Pa)
k	gas permeability ($m^2 s^{-1}$)or rate constant (s^{-1} or $Pa^{-1} s^{-1}$)
V	volume of GDE or electrical voltage(V)
d	diameter (m)
R	ideal gas constant ($J mol^{-1} K^{-1}$)
T	temperature (K)
M	molar mass ($kg mol^{-1}$)
N	superficial flux ($mol m^{-2} s^{-1}$ or $kg m^{-2} s^{-1}$)
x	mole fraction
w	mass fraction
D	binary diffusion coefficient ($m^2 s^{-1}$)
C	concentration ($mol m^{-3}$)
i	current density ($A m^{-2}$)
n	drag coefficient
i_o	exchange current density ($A cm^{-2}$ Pt)
n	number of electrons
L	platinum loading in electrode ($g cm^{-2}$)
A	electrochemical area of Pt (cm^2_{pt}/g)
E	Young's modulus (MPa)
G	shear modulus (MPa)
EW	equivalent weight (kg/mol)
Greek letters	
η	gas viscosity (Pa s)
ρ	density ($kg m^{-3}$) or contact resistivity (ohm m)
ε	porosity
σ	electron conductivity (S/m)

κ	proton conductivity (S/m)
Φ	electric potential
α	transfer coefficient
ν	Poisson's ratio
γ	water mass transfer coefficient (m/s)

Subscripts

th	through plane
in	in plane
s	solid phase
g, GDE	gas diffusion electrode
CK	the Carman-Kozeny
f	fiber
i,j	species
m	membrane
a	anode
c	cathode or condensation
o	exchange current
H_2	hydrogen
O_2	oxygen
e	electrolyte
BPP	bipolar plate
ve	visco-elastic
ht	Hygro-thermal
w	water
v	vaporization
d	drag
+	ionic

Superscripts

eff	effective
sat	saturation
m	membrane

CHAPTER 1   INTRODUCTION

1.1   Overview of Polymer Electrolyte Membrane (PEM) Fuel cell

Fuel cells coverts energy stored in chemicals to electricity directly via electrochemical oxidation of fuel at anode and reduction of oxidant at cathode. Fuel cells can potentially reduce our dependence on fossil fuels and be used in various applications from portable power, to transport and stationary power systems[1]. Unlike batteries that need replacement or recharge after discharge, fuel cells continuously generate electricity as long as the reactants are being replenished. In addition, the advantages of fuel cell include high energy efficiency, scalability, low pollution, and quiet operation [2]. Among various fuel cell types, such as Alkaline Fuel Cell(AFC), Phosphoric Acid Fuel Cell(PAFC), Molten Carbonate Fuel Cell(MCFC), and Solid Oxide Fuel Cell(SOFC), Proton Exchange Membrane (PEM) fuel cells have been receiving the most attention for automotive and small stationary applications because of its comparatively high power density, low operation temperature($80 \sim 120^{o}C$), fast start-up capability, among others [3].

For the PEM fuel cell, gaseous hydrogen is used as a fuel and oxygen in the ambient is utilized as an oxidant. A schematic of a typical PEM fuel cell is shown in Figure 1-1[4]. The PEM fuel cell has several components such as a solid phase electrolyte, that is, an ionomer membrane, electrode catalyst layers (CL) at anode and cathode, gas diffusion layers

1

(GDL), and bipolar plates (BP). The fuel, hydrogen, is supplied into a flow field in the bipolar plate at the anode side, diffuses through the gas porous medium, and is consumed by electrochemical oxidation reaction at the anode catalyst layer, being dissociated into proton and electron. The gas diffusion layer, generally made out of carbon-fiber based materials such as non-woven papers and woven cloths, serves as a support for the polymer electrolyte membrane, a diffusion pathway of the gas reactant, and an electric conductor for electrons[5]. The catalyst in PEMFC typically uses platinum group metal/alloy nanoparticles supported on a high-surface-area carbon black[6]. The ionomer membrane conducts protons produced by anode reaction of hydrogen oxidation and serves as an electron insulator and gas separator between anode and cathode as well. Besides, the membrane can absorb the water due to a hydrophilic side chain so that swell or shrink in volume according to the water content in the membrane, which indicates the number of water molecules adsorbed by each sulfonic acid group. At the cathode side, the oxidant, oxygen in air, is fed into the cathode flow field, moves through the cathode diffusion medium, and is reduced at the cathode catalyst layer reacting with protons transferred through the ionomer membrane and electrons through the external circuit from the anode to form water.

2

Anode Reaction (Hydrogen Oxidation Reaction (HOR)):

$$2H_2 \rightarrow 4H^+ + 4e^- \qquad (1.1)$$

Cathode Reaction (Oxygen Reduction Reaction (ORR)):

$$O_2 + 4e^- + 4H^+ \rightarrow 2H_2O \qquad (1.2)$$

Overall Reaction:

$$H_2 + 1/2\ O_2 \rightarrow H_2O \qquad (1.3)$$
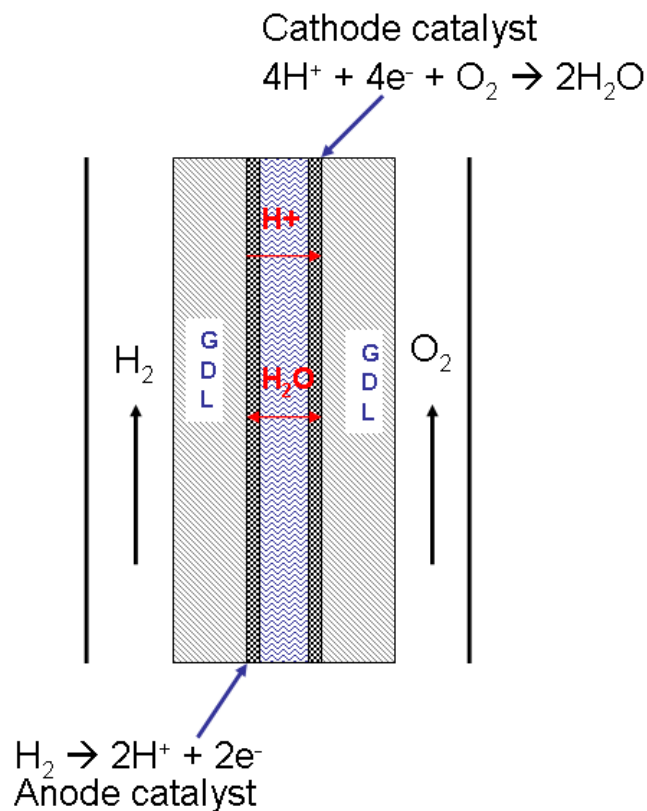
Figure 1-1   Schematic of the typical PEM fuel cell

3

Fuel cell performance is generally characterized by a polarization curve, which is a plot of cell voltage with respect to a current density as shown in Figure 1-2. The theoretical open circuit voltage (OCV) of the PEM fuel cell is around 1.23V at a standard condition (1 atm, 25°C, hydrogen and oxygen fuel cell).   However, due to an inevitable mixed potential of Pt/PtO at cathode and hydrogen gas crossover[7], the open circuit voltage between 0.9 ~ 1.0V is typically observed in a real fuel cell experiments.
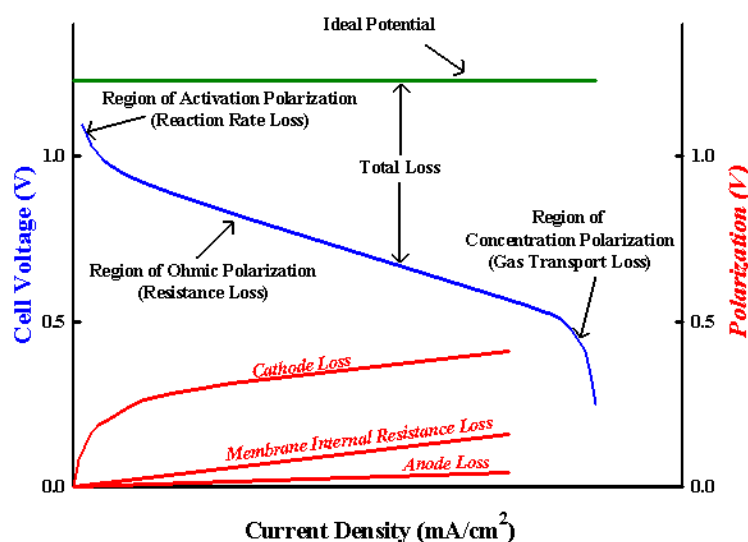
Figure 1-2   Polarization curve of the PEM fuel cell

As the current is drawn from the fuel cell, the cell voltage drops gradually from the OCV due to various losses including anode and cathode kinetic loss (sluggish oxygen reduction[8, 9]); Ohmic resistance loss by proton and electron transfer, and finally mass

4

transport loss which increase dramatically at high current density [10].

1.2 Purpose of Study

To date, considerable efforts have been made to develop and commercialize the highly efficient PEM fuel cell system for many applications. However, technical challenges still remain for reliability and durability of fuel cell components[11]. Particularly, fuel cells for automotive applications are likely to operate under various load conditions such as frequent starts and stops, acceleration, deceleration, and constant power modes and are expected to withstand variations in environmental conditions, specifically such as temperature, humidity, and contaminants. They must be also durable enough to power the system over the course of 5000hr without any significant performance loss[12, 13]. With current state-of-the-art technologies, PEM durability still falls short of meeting the targets.

5
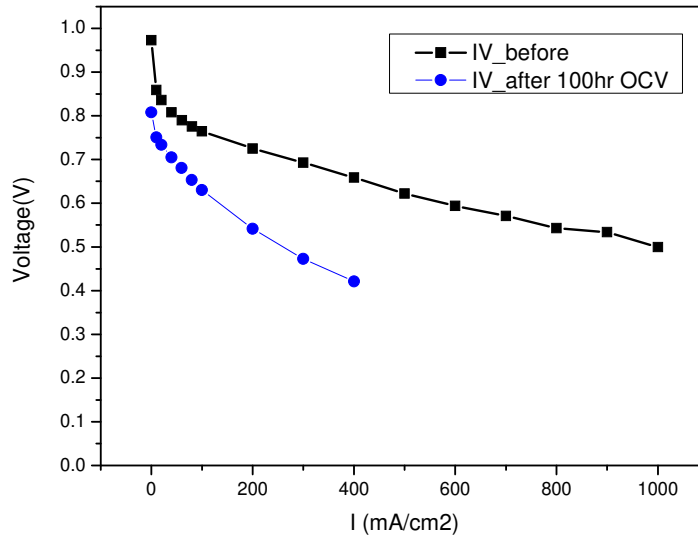
Figure 1-3   Performance drop of a PEM fuel cell after OCV condition

The performance degradation of fuel cells is a combined effect of degradations in each fuel cell components; bipolar plate, ionomer membrane, catalyst, gas diffusion layer, etc. Borup *et al.*[14] and Frisk *et al.*[15] found that operating temperature increased the loss of GDL hydrophobicity and degraded GDLs in 15wt% hydrogen peroxide(H_2O_2) at 82°C exhibited a weight loss and caused an increase of contact angle with time by oxidation of the carbon, which can induce water flooding. Metallic materials such as metal bipolar plates and end plates for a fuel cell stack assembly corrode under a warm (65~90°C), acidic (pH 2~3) and humid environment in a fuel cell. Metal cations, such as Fe^{2+}, Ni^{2+}, and Cr^{3+}, released during the corrosion process can degrade the membrane and metal oxides formed on the corroded surfaces increases electrical contact resistance, leading to reduce fuel cell

6

performance[16-20]. Also, the catalyst materials are subject to conditions that promote

oxidation, namely, high potential and the presence of gas phase oxygen and surface oxidation

of platinum has been reported to decrease the electrocatalytic activity for oxygen reduction[6,

21-24]. The kinetics of the Pt oxidation at the electrode is also affected by relative humidity

(RH) [25] and cycling parameters such as time periods and lower voltage level in the

potential cycling test[24, 25].

Platinum oxidation

$$Pt + H_2O \rightarrow Pt\text{-}OH + H^+ + e^- \hspace{4cm} (1.4)$$

$$Pt\text{-}OH \rightarrow Pt\text{-}O + H^+ + e^- \hspace{4cm} (1.5)$$

Darling *et al.* [26] and Yasuda *et al.*[27] investigated platinum dissolution and

movement from the catalyst layer to the membrane after potential cycling. This process

induces a loss in the catalytic activity, reducing the performance of the fuel cell.

Among the degradation effects from all the components of fuel cells, one of the

important factors determining the PEM fuel cells' life time is the membrane degradation and

failure[1, 11, 28, 29]. The membrane degradation is commonly classified into mechanical and

chemical degradation. The mechanical degradation manifests as a gradual reduction of

7

mechanical strength and toughness of the membrane or MEA. It can result in catastrophic membrane failure in the forms of perforations, cracks, tears or pinholes. Membrane mechanical degradation may originate from congenital membrane defects or defects formed by inappropriate membrane electrolyte assembly (MEA) fabrication processes, and most likely defects formed by localized chemical decomposition of the membrane. These defects grow due to cyclic stresses and strains in the membrane under the variations in temperature and humidity (hygro-thermal cycle) in the constrained fuel cell environment during the operation [1, 3, 11]. The membrane in the constrained fuel cell is likely to experience in-plane tension and compression resulting from membrane shrinkage and swelling under low and high RH condition. It is believed that the reduction of mechanical strength and toughness of the PEM in the fuel cell stack is one of the major causes of sudden catastrophic stack failures[3]. A formation of local pinholes and perforations in the membrane can result in reactant gases' crossover causing local hot spot via direct exothermic combustion of the hydrogen and oxygen on the catalyst layer[30, 31]. On the other hand, chemical degradation of the membrane is believed to result from an attack to polymer chain by a highly reactive free radicals (•OH, •OOH) generated via electrochemical or chemical reaction of crossover H_2 and O_2[32]. These radical attacks induce a polymer backbone and side chain scission and unzipping until a entire polymer chain is disappeared [33, 34]. In the past decade,

8

a significant amount of work have been carried out to identify the degradation mechanisms of the fuel cell membranes and MEAs, however, the mechanisms are still far from clear and controversies remain in the literature[29]. The lack of effective mitigation methods is largely due to the currently very limited understanding of the underlying mechanisms for degradations of fuel cell membranes.

It is the objective of this research to further understand the fundamental membrane degradation mechanisms by mechanical and chemical factors, such as hydroxyl/hydroperoxyl radicals attack and mechanical stress due to cyclic hydrations. The fundamental scientific understanding of the above will likely leads to new mitigation methods against premature membrane failure.

1.3   Literature Review
1.3.1   *Polymer Electrolyte Membrane (PEM)*

The most commercially available membranes used in PEM fuel cells are the perfluorosulfonic acid (PFSA) polymer membranes, e.g., Nafion®, developed and manufactured by DuPont™. The PFSA membrane selectively conducts protons. This is enabled by a sulfonic acid group (SO_3H) (hydrophilic) attached to the tetrafluoroethylene (TFE) backbone via a short side chain, as shown in Figure 1-4.

Microstructures and properties of ionomer membrane have been studied extensively

9

using Small Angle X-Ray Scattering (SAXS) and/or Small Angle Neutron Scattering (SANS) for structural changes by swelling[35, 36] and identifying the structural model of ionic domains characterized by core-shell model [37], two phase model[38], spherical ionic cluster [39, 40], rod-like network model[41, 42], elongated polymeric aggregates in bundles[43], and recently cylindrical micelle structure[44] (Figure 1-5). However, due to the extremely complex morphology of PFSA ionomer and limited microscopic characterization methods, the reported microstructure models of PFSA membranes remain ambiguous and controversial. What is widely agreed is the presence of three phase nature i.e., hydrophilic cluster, amorphous and semicrystalline perfluorocarbon phase, interdispersed at nanoscale. Also, there have been no fundamental first-principle based model for PFSA membrane that has predicted considerably new phenomena or caused significant property enhancements in a substantial way[45].

The proton conductivity of PFSA membranes is highly dependent on their water content and the orientation of ionic domains[46]. The membrane in water saturated state shows the highest proton conductivity[47]. At the same time, the water saturated membrane also swells in volume significantly as can be seen in Figure 1-6[42]; swelling can modify the micro structure of ionic clusters; spherical or cylindrical water pools are formed with the ionic groups at the polymer water interface, and the volume of clusters and diameter

increases as the water content increases. Besides conducting protons, the membrane also

separates the anode (hydrogen) atmosphere from the cathode (air) atmosphere.

In following sections, the mechanical and chemical degradation mechanisms reported

in the literatures will be reviewed.

$$-[-(CF_2-CF_2-)_n-(CF_2-CF)-]-_x$$
$$O-(-CF_2-CF-O-)_m-CF_2-CF_2-SO_3H$$
$$CF_3$$
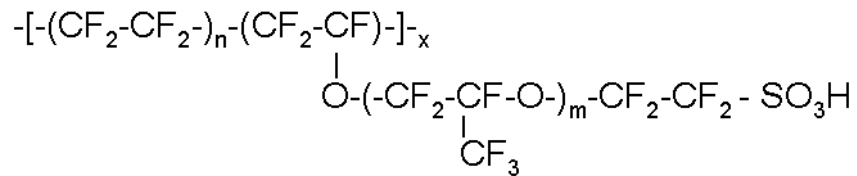
Figure 1-4   Average chemical structure of Nafion® of 1,100 equivalent weight (EW)
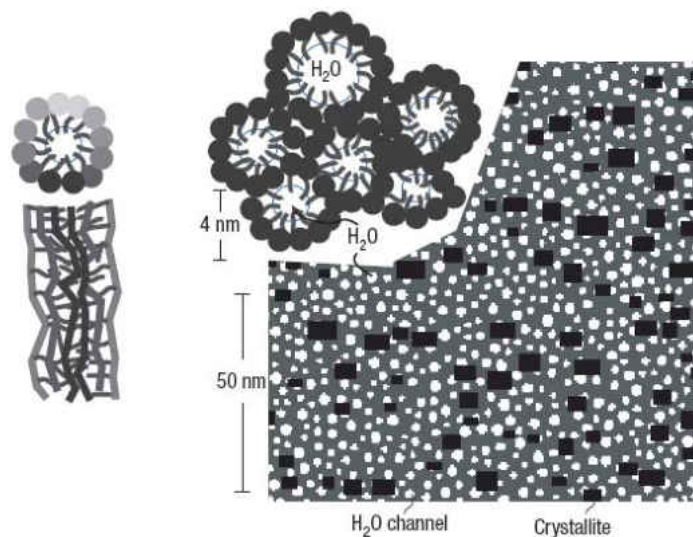
Figure 1-5   Parallel water channel (inverted micelle cylinder) model of Nafion®

(Adapted with permission from ref [44])
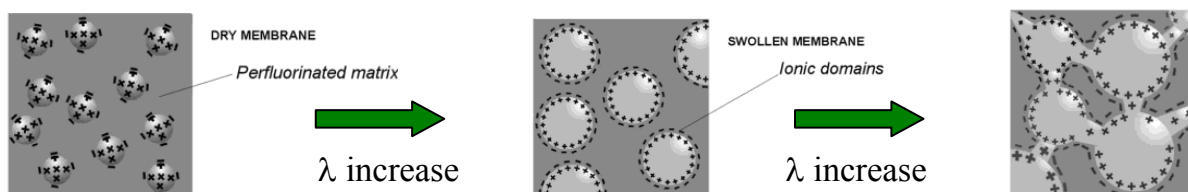
Figure 1-6   Schematic representation of the structural evolution depending on the water

content(Adapted with permission from ref [42])

1.3.2 *Polymer Electrolyte Membrane degradation*
1.3.2.1 Mechanical degradation

Mechanical degradation generally implies microscopic and macroscopic effects

induced under the influence of mechanical forces[48]. The durability of membranes is

ultimately limited by the physical breaching of the membrane in the form of pinholes or

cracks, which results in rapid reactant cross-over and subsequent cell/stack failure[29, 30, 49].

During the membrane degradation process, the thinning, weight loss, fluoride emission, and

crazing formation have been observed.   Huang *et al.*[49] reported that significant reduction

of membrane electrode assembly (MEA) ductility can be seen as drastically reduced strain-to-

failure of the RH-cycled MEAs and postmortem analysis revealed the formation and growth

of mechanical defects such as cracks and crazing in the membranes and MEAs as shown in

Figure 1-7.
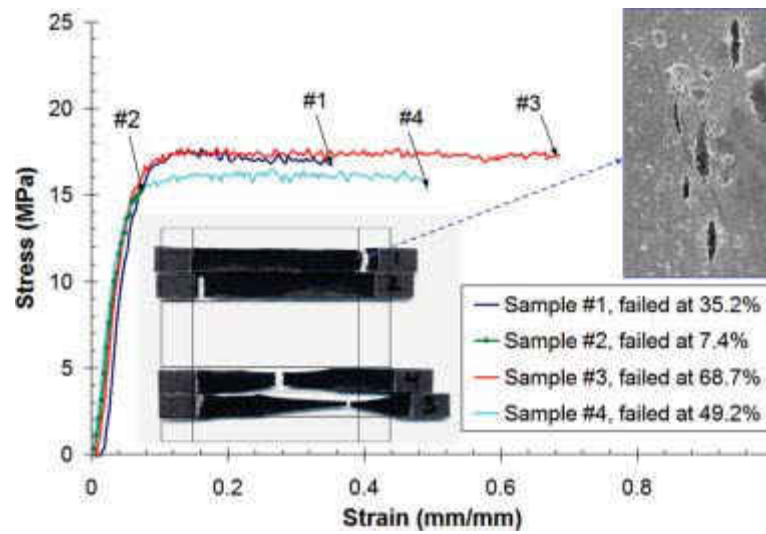
Figure 1-7   Stress-strain curves of MEA after 50 cycles from 80 to 120% RH

(Adapted with permission from ref [49])

The author [50] recently studied mechanical properties of recast reinforced composite

membranes with ePTFE (Tetratex®) and observed that the mechanical   strength and

toughness of the membrane reduced significantly after an OCV hold testing for 100hr.   SEM

analysis also confirmed that localized cracks form inside the membranes. Tang *et al.*[51]

conducted cyclic stress test on membrane and found that the significant dimensional change

of the membrane was observed and the microstructure breakdown appeared on the

membrane surface when the cyclic stress was over 3.0MPa. This result indicates that the

PEM can be fractured under much lower stress than ultimate strength when it is subjected to

the condition of fatigue. The author also reported that the stress induced by temperature

13

variations is much smaller than the stress under RH cycling tests. However, they concluded that the membrane degradation was accelerated significantly when the cyclic operations of temperature and humidity are applied to membranes simultaneously.

It is reported [31] that the repeated shrinking and swelling of a membrane accelerates gas crossover, generating local hot spots via exothermic reactions of the hydrogen and oxygen on Pt catalyst and in turn, pinholes. Inaba *et al.*[52] also revealed that the gas crossover rate increased with temperature and humidity. This results is assumed to be related with the dependence of the free volume and cluster size distribution on the water content and temperature, supported by the positron annihilation spectroscopy(PAS) data [53, 54]. Sethuraman *et al.*[55] also reported that oxygen permeability across the membrane decreased by 50% when RH was decreased from fully saturated to 25%.

The mechanical behavior of ionomer membranes is strongly dependent on the membrane water content and temperature. Up to a certain temperature, chain mobility and morphological relaxation of intermolecular chain is expected to increase with temperature, which can be explained by reptational dynamics[56]. At low temperature, the water acts as plasticizer softening the membrane and reducing load carrying capability[57]. However, at elevated temperature, surprisingly, the opposite trend is observed: that is, the more water the membrane absorbs, the stronger the membrane become [58, 59]. This abnormal behavior is

14

not yet clearly understood.

1.3.2.2 Chemical degradation

Chemical degradation refers to the chemical decomposition of the PFSA membrane. It is commonly believed that PFSA membrane is attacked by highly reactive oxygen radicals (•OH, •OOH) generated by an electrochemical or chemical reaction of hydrogen and oxygen at a platinum catalyst [32, 60-62]. The radicals are highly reactive due to their unpaired electrons and react with weak polymer endgroups in the membrane; an open shell is a valence shell which is not completely filled with electrons. Pozio *et al.*[63] postulated that the free radical attack of the perfluorinated molecular chains from weak bonds is a degradation mechanism and the radicals are derived from H_2O_2, which can form from a two-electron oxygen reduction at cathode[4, 64] as can be seen in equation (1.6) and from oxygen molecules permeated through the membrane from the cathode to anode[4] in equation (1.7) to (1.9). The hydrogen peroxide was clearly observed within a PEM fuel cell membrane when H_2 and air are present as gas inputs by an *in situ* experimental technique[60].

$$O_2 + 2H^+ + 2e^- \rightarrow H_2O_2 , \quad E^0 = 0.695V \text{ vs SHE} \tag{1.6}$$

$$H_2 + Pt \rightarrow Pt\text{-}H \text{ (at anode)} \tag{1.7}$$

$$Pt\text{-}H + O_2 \text{ (diffused through PEM to anode)} \rightarrow \bullet OOH \tag{1.8}$$

$$•OOH + Pt\text{-}H \rightarrow H_2O_2 \qquad\qquad\qquad\qquad\qquad\qquad (1.9)$$
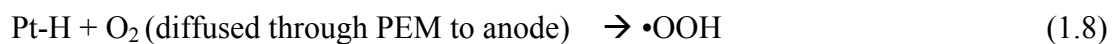
This H_2O_2 can diffuse into the membrane and chemically breaks down into hydroxyl radicals assisted by metal ions present in the membrane[63-65].   In situ radical formation has been detected at cathode side of the polymer membrane by the electron spin resonance (ESR) techniques[66].

$$H_2O_2 + M^{2+} \rightarrow M^{3+} + •OH + OH^- \qquad\qquad\qquad\qquad (1.10)$$

$$•OH + H_2O_2 \rightarrow •OOH + H_2O \qquad\qquad\qquad\qquad\qquad (1.11)$$

The decomposition mechanism of the membrane by radical attacks to the polymer weak end group such as $-CF_2COOH$ is introduced by Curtin *et al.* [28] The reaction mechanism is shown below.   Note that –COOH is regenerated in reaction (1.14). Therefore, once decomposition process begins at one end group, a whole chain unit can be decomposed to HF, CO_2, and low-molecular weight species by the radical depolymerization reactions (so called "unzipping mechanism")[4]. It has been reported that the formation of H_2O_2, SO, SO_2, H_2SO_2, and H_2SO_3 were detected by direct gas mass spectroscopy of the cathode outlet gas[67]. Others suggested that sulfonic acid groups may be the key to the radical attack

mechanism and membrane degrading species can be directly formed by molecular H_2 and O_2 on the surface of Pt catalyst subject to the surface properties of Pt catalyst [68].

$$Rf–CF_2COOH + •OH \rightarrow Rf–CF_2• + CO_2 + H_2O \qquad (1.12)$$

$$Rf–CF_2• + •OH \rightarrow Rf–CF_2OH \rightarrow Rf–COF + HF \qquad (1.13)$$

$$Rf–COF + H_2O \rightarrow Rf–COOH + HF \qquad (1.14)$$
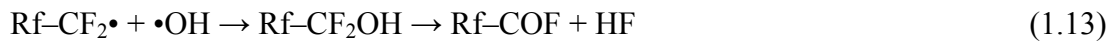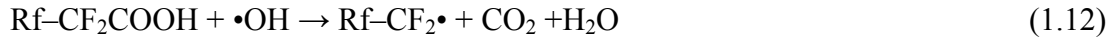
However, Cipollini[34] insisted that this reaction sequence mush be modified in a way that the attack of the membrane will occur through the peroxyle radical, rather than by the hydroxyl radical since the relative rate constants for hydroxyl radical generation is so slow as to be negligible.

$$Fe^{+2} + H_2O_2 \rightarrow Fe^{+3} + OH- + \cdot OH \qquad k = 76 \text{ L mole}^{-1} \text{ s}^{-1} \qquad (1.15)$$

$$H_2O_2 \rightarrow 2\cdot OH \qquad k = 1.2 \times 10^{-7} \text{ L mole}^{-1} \text{ s}^{-1} \qquad (1.16)$$

$$\cdot OH + H_2O_2 \rightarrow \cdot OOH + H_2O \qquad k = 8.5 \times 10^{+7} \text{ L mole}^{-1} \text{ s}^{-1} \qquad (1.17)$$
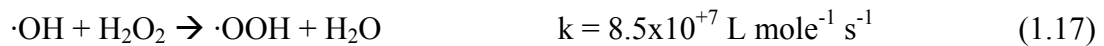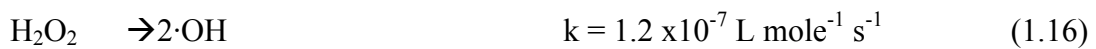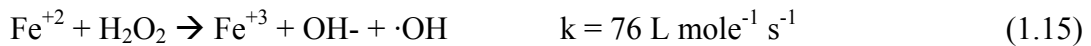
A few reports have suggested that, even without susceptible end groups, under H_2 environment, the polymer backbone of the PFSA membrane may preferentially reacts as following [69, 70]:

17

$$-CF_2-CF_2- + 2H_2 \rightarrow -CH_2-CH_2- + 4HF \tag{1.18}$$

As it has been recognized that the formation and reactivity of free radical species are a major culprit of degradation of PEMs used in fuel cells, Fenton's test, using H_2O_2 solution containing a trace amount of Fe^{2+}, has become a popular *ex situ* test for membrane durability [71-73] screening. The hydroxyl and hydroperoxyl radicals are generated from well-known Fenton reaction; hydrogen peroxide is catalyzed by a trace amount of ferrous iron. The membrane immersed in the solution can be degraded by radicals generated in the Fenton's reaction. However, due to a intrinsic drawback of the Fenton's test: the difficulty in evaluating its accelerating factor and lack of mechanical effects[34], even though the test seems to be a good accelerated test for judging chemical degradation of ionomer membrane, but the test results is not necessarily correlated with the durability of membrane in fuel cell operation.

$$H_2O_2 + Fe^{2+} \rightarrow HO\bullet + OH^- + Fe^{3+} \tag{1.19}$$

$$Fe^{2+} + HO\bullet \rightarrow Fe^{3+} + OH^- \tag{1.20}$$

$$H_2O_2 + HO\bullet \rightarrow HO_2\bullet + H_2O \tag{1.21}$$

$$\text{Fe}^{2+} + \text{HO}_2\bullet \rightarrow \text{Fe}^{3+} + \text{HO}_2^{-} \tag{1.22}$$

$$\text{Fe}^{3+} + \text{HO}_2\bullet \rightarrow \text{Fe}^{2+} + \text{H}^+ + \text{O}_2 \tag{1.23}$$

$$\text{Fe}^{3+} + \text{H}_2\text{O}_2 \rightarrow \text{Fe}^{2+} + \text{H}^+ + \text{HO}_2\bullet \tag{1.24}$$

1.3.2.3 Accelerated degradation of membrane in fuel cells

PFSA membrane is believed to degrade via two main pathways: "main chain scission" and "unzipping", as illustrated in Figure 1-8. The chain scission refers to a chemical reaction resulting in homolytic cleavage of the backbone or main chain of the macromolecule; it generates two chain radicals which can lead to a reduction in molecular weight, i.e. a diminution of chain length. On the other hand, the degradation by unzipping mechanism starts from the chain ends, resulting in successive release of the monomeric units and this process resembles the reverse of the propagation step in chain polymerization[74]. The chemical decomposition of the membrane frequently result in a weakened membrane that fails under mechanical stresses induced by RH variation in a mechanically constrained fuel cell environment [29, 49, 51, 68, 75, 76]. Preliminary evidence has shown the mechanical stress can accelerate the chemical decomposition rate of the PFSA membrane[49]. Degradation of PEM fuel cells manifests itself as a gradual irreversible performance decay followed by a catastrophic failure, typically due to excess gas cross over. An OCV durability test at relatively high temperature (e.g. 90ºC) and low RH (~30%) have been used

19

by many research groups as an accelerated degradation test [33, 50, 55, 75, 77-79]. During the OCV test, the cell voltage is held at the open circuit without an electrical load for extended periods of time. Membrane degrades severely under this condition. This is believed to be the results of high gas cross over rate due to high partial pressure of the reactant gasses [79] and high temperature and low RH condition [32]. Fluoride ion emission (FER), weight loss, membrane thinning, Pt band formation, micro crack, crazing formation, etc. are typically observed after OCV test after several tens of hours. SEM images of MEA before and after the OCV test is shown in Figure 1-9 and micro cracks and membrane thinning can be clearly observed.
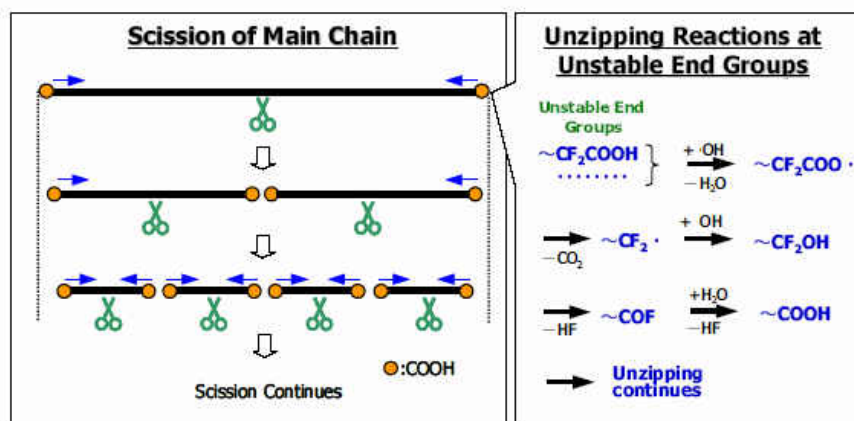
Figure 1-8   Chain scission and unzipping mechanism

(Reproduced by permission of the Journal of Electrochemical Society [77])

Recently, a vapor phase hydrogen peroxide exposure test has been developed to understand membrane degradation mechanism as a new *ex situ* accelerated test method and the test results indicated that not only unzipping of chain molecules, but also chain scission takes place in the vapor phase peroxide test and degradation become more aggressive than that in the liquid phase Fenton's test [77, 78, 80].

Based on evidences in the literatures, membrane failure is believed to be the consequences of the combined chemical and mechanical effects acting together. Reactant gas crossover, hydrogen peroxide formation and movement, cyclic stresses and strains, recrystallized Pt particles, and transition metal ion contaminants are believed to be major factors contributing to the decomposition of polymer electrolyte membranes.
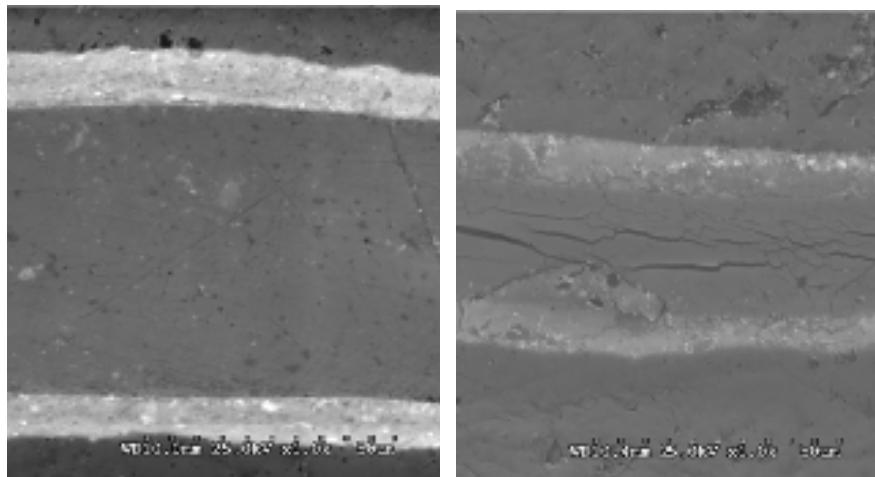
Figure 1-9   Cross-section SEM of MEA with N-112 membrane before (left) and after (right) 100 hours of OCV test

21

Besides, there are considerable experimental evidences indicating that chain scission reactions are occurring in fuel cell tests conducted under high temperature OCV testing. While chemical degradation of prefluorinated membranes has been investigated and reported extensively in literature [33, 78, 80-93], there has been little work on investigation of the interaction between the chemical and mechanical degradation.   In next chapter, author will introduce new hypothesis and experimental and numerical approach for further understanding fuel cell membrane degradation mechanisms.

CHAPTER 2   EXPERIMENTAL AND NUMERICAL METHODS FOR MEA DEGRADATION STUDY

2.1 Motivation

The fundamental idea of this research is based on an experimental observation on the mechanical properties of the degraded membrane. Strain-to-failure obtained by uniaxial stress-strain test is an indicator of membrane ductility. It was experimentally observed by Zhao *et al.* [72] that the homogeneously degraded membrane by liquid phase Fenton's test (chemical degradation) does not necessarily result in the loss of membrane ductility even though the membrane lost 31% of fluoride and this is a completely different behavior with that of chemically degraded membranes in a fuel cell environment and that of mechanically degraded membranes by the RH cycling test as shown in Figure 2-1. Given these contrasting experiment results, the author believed that the membrane mechanical weakening is likely a result of localized and inhomogeneous membrane degradation.   This motivates the author to seek experimental proof and underlying causes of localized degradation mechanisms.

(a)	(b)
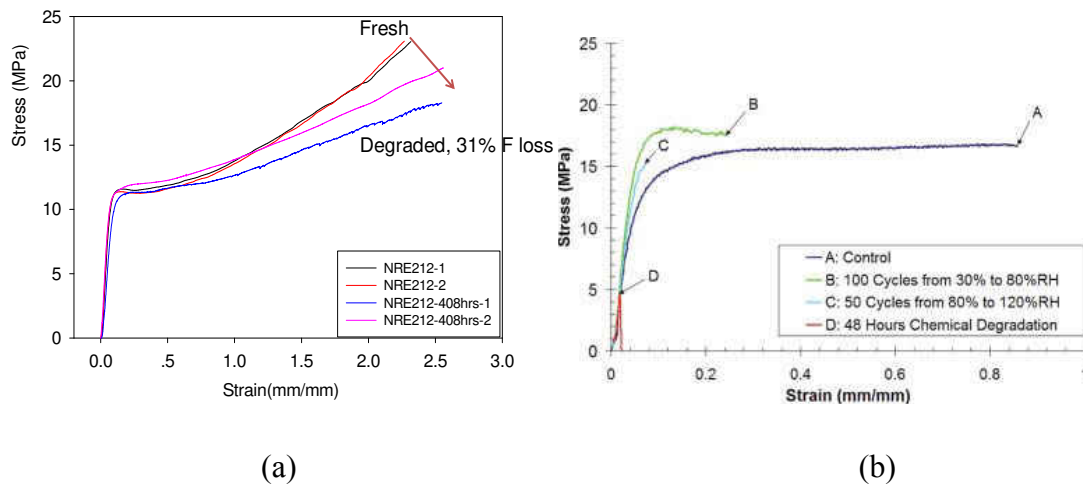
Figure 2-1   Stress-Strain Behavior of (a) NRE-212 membrane samples before and after Fenton degradation test [72]   (b) NRE-111 membrane electrolyte assembly before and after RH cycling and OCV test [49]

2.2   Methodologies

The lack of understanding of fundamental membrane degradation mechanisms can be attributed to a number of scientific barriers. At a microscopic scale, the direct observation of defect formation and growth has not been achieved due to the lack of line of sights and the lack of effective non-destructive evaluation methods. Therefore, experimental and numerical techniques needs to be developed to validate the mechanism.   This section will concentrate on introducing new *ex situ* experimental techniques and numerical modeling for ionomer membrane and fuel cells.

24

2.2.1 *Introduction*

Performance degradation mechanisms of PEM fuel cells have been discussed by many researchers. One of them is related to local hydrogen starvation, which may be present during start-stop. Before the startup of the fuel cell, air can be present on both the anode and cathode due to leakage from outside air and /or crossover through the membrane. Reiser *et al.*[94] conducted a numerical modeling to simulate the hydrogen starvation condition and reported that the electrolyte potential drops from 0 to -0.59V (vs. RHE) when the anode is partially exposed to hydrogen and partially exposed to oxygen during the start-up of the fuel cell, thereby leading to a high cathode interfacial potential; it is called "reverse-current" mechanism. This high cathode potential accelerates carbon corrosion, Pt oxidation and dissolution in catalysts and redistribution in membranes (Pt band) and eventually, decreases performance due to a loss of electrochemical area (ECA)[26, 95, 96]. Pt particles were experimentally detected by transmission electron microscope (TEM) [97]. The loss of ECA can be explained by the several mechanisms and one of them is a phenomenon known as Ostwald ripening[23]; small Pt particles dissolve in the ionomer phase in the catalyst layer and redeposit on the surface of large particles, causing particle growth, On the other hand, the dissolved Pt ions may migrate into the ionomer phase and subsequently precipitate in the membrane via reduction of Pt ions by the crossover hydrogen from the anode side (Pt band formation), decreasing membrane stability and conductivity[93, 97].

25

Carbon corrosion:

$$C + 2H_2O \rightarrow CO_2 + 4H^+ + 4e^- \qquad E^o = 0.207 \text{ vs RHE} \tag{2.1}$$

Platinum dissolution:

$$Pt \rightarrow Pt^{2+} + 2e^- \tag{2.2}$$

Platinum oxide film formation:

$$Pt + H_2O \rightarrow PtO + 2H^+ + 2e^- \tag{2.3}$$

Chemical dissolution of platinum oxide:

$$PtO + 2H^+ \rightarrow Pt^{2+} + H_2O \tag{2.4}$$

Performance degradation of fuel cells can be observed due to local fuel starvation[98] and local membrane degradation has been observed due to cathode catalyst overlap[99]. During a normal operation of fuel cells, if the fuel supply to the anode is interrupted, the circumstance can damage the membrane and catalysts by increase of cathode electric potential, thereby increasing the kinetics of the carbon corrosion, Pt oxidation and dissolution as explained above. Besides that, the cathode overlap can result in the local cathode potential in the region between the anode and the cathode edges to rise to the open-circuit potential due to the drop of the electrolyte potential as can be seen in Figure 2-2, where corrosion of the

26

carbon components occur as well. Therefore, it can be noticed that uncontrolled overlap of anode and cathode electrodes in PEMFC membrane electrode assemblies (MEAs) may lead to the development of OCV conditions at locations where the cathode electrode unintentionally overlaps the anode electrode by a distance on the order of several membrane thicknesses.

The above experimental observation also suggests that the dissolved Pt particles can play an important role in the performance degradation. Another evidence for the membrane degradation that Pt particles are involved in were investigated recently; that is, hydrogen peroxide (H_2O_2) formation at the Pt band in membranes, which is already known as the degradation specie of membranes[75, 100]. The author indicated that the location of the Pt band in membranes are correlated with the amount of the FER from both electrodes and consequently, the decomposition of an MEA during OCV hold test is enhanced by the Pt band formation in membranes; mainly determined by the gas compositions at both electrodes and gas permeability of the membranes, and the accelerated hydrogen peroxide formation rate at the Pt band due to a lower oxygen reduction rate(ORR) activity and higher 2-electron reaction rate at the band.
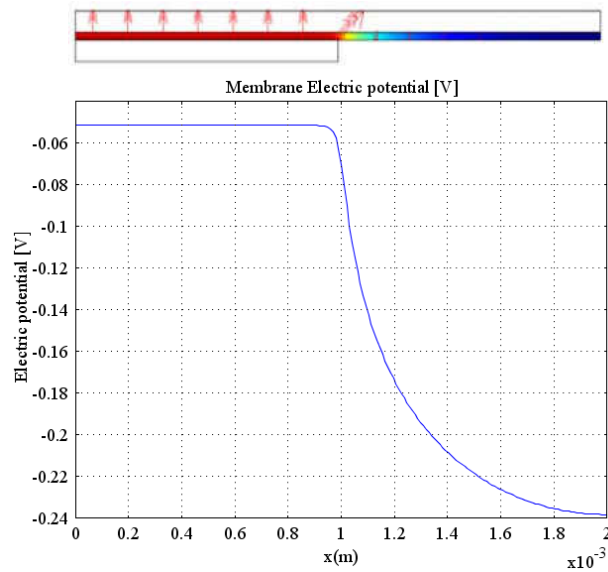
Figure 2-2   Membrane electric potential drops due to the cathode overlap

(Numerical simulation)

2.2.2 *Fuel cell test with bilayer membrane*

Once the catalyst is coated onto both sides of membranes to form a MEA or Catalyst

Coated Membrane (CCM), surface analysis of the membrane become almost impossible;

removing the catalyst layer without leaving any damages on the membrane is very difficult.

As such, in order to characterize the degraded membranes, a bilayer membrane method is

proposed for the membrane degradation study. Similar idea was already introduced in the

literature for identifying the mechanisms of the membrane degradation[62, 68], but in this

research, the configuration of bilayer membranes are somewhat different.

In Figure 2-3, two one-side coated MEAs or CCMs are fabricated by spraying a

catalyst ink onto only one side of the ionomer membrane, and two membranes is then hot-

28

pressed to bond each other, realizing a single MEA. After fuel cell test, two one-side coated

MEAs can be separated. The backside of the CCM provides access to Raman or IR

spectroscopy. Also, the technique allows one to differentiate in chemical and mechanical

properties of the membrane near the cathode and the anode side.
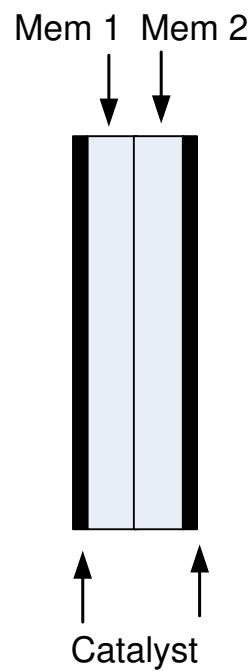
Figure 2-3   Proposed configuration of the bilayer membrane

2.2.3 *Gas phase Fenton's test*

It has been reported that the degradation of many polymers and rubber materials was

accelerated by mechanical force, and mechanically induced homolytic cleavage of the

backbone bonds was the initiator leading to the formation of two free chain radicals as the

primary degradation step of polymers: these radicals may recombine or react with oxygen

from air or attack other polymer molecules. [101-103] It is, therefore, hypothesized that the C-C bond in the TFE backbone or other chemical bonds in a fuel cell membrane may be ruptured by mechanical stress due to the mechanically constrained environment and chain radicals react with oxygen and/or impurities from the gas channel or highly reactive oxygen radicals produced by the mechanism explained previously, or attack other polymer chains.

Recently, different groups have reported results from an *ex situ* vapor phase hydrogen peroxide test[77, 78, 80] and found that gas phase hydrogen peroxide is very aggressive toward perfluorosulfonated(PFSA) membrane, causes chain scissions in the backbone and in the side chain[104]. In the test setup, an iron-impregnated membrane is exposed to the gaseous hydrogen peroxide to simulate the PEM fuel cell environment instead of the liquid in the typical Fenton's test; in a fuel cell, vapor phase hydrogen peroxide is expected be present. The hydrogen peroxide gas is supplied by the inert carrier gas, nitrogen in this setup and replenished to the chamber containing the membrane; the hydrogen peroxide gas reacts with the iron doped in the membrane to form the reactive oxygen radicals and generates reaction products such as HF. These decomposed products are collected in KOH solution for further analyses.

In order to verify the hypothesis of the stress induced chemical reaction, this test setup is modified so that the mechanical stress can be applied while the chemical reaction is

30

proceeding as shown in Figure 2-4. The stress is applied to the membrane by hanging a

dead weight.
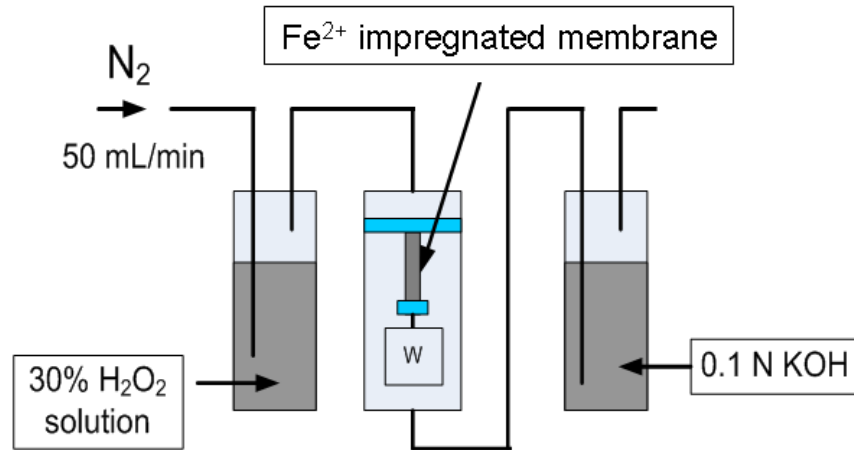
Figure 2-4 H_2O_2 gas cell for the *ex situ* accelerated degradation test of PFSA membrane

with and without applied mechanical stress

With this setup, the membrane is subjected to a controlled mechanical loading and

chemical degradation at the same time and the results can be compared with those at the

different stress level. FER will be monitored during the test.   After test, the weight loss will

be measured and the sample will be analyzed using Raman and FTIR spectroscopy.

2.2.4 *Development of constitutive model of ionomer membranes*

The stress prediction of the ionomer membrane in various conditions in fuel cells is

the key to understand the proposed mechanisms (section 2.2.3) of the membrane degradation.

31

Polymers are distinguished uniquely from other structural materials such as metals and ceramics, because of their macromolecular nature characterized by the covalent bonding and long chain structure [105]. The physical properties of polymeric systems are strongly affected by chain microstructure, i.e., isomerism, which is the organization of atoms along the chain as well as the chemical identity of monomer units [106]. Another important feature controlling the properties of polymeric materials is polymer architecture; types of polymer architectures include linear, ring, star-branched, H-branched, comb, ladder, dendrimer, or randomly branched as sketched in Figure 2-5.
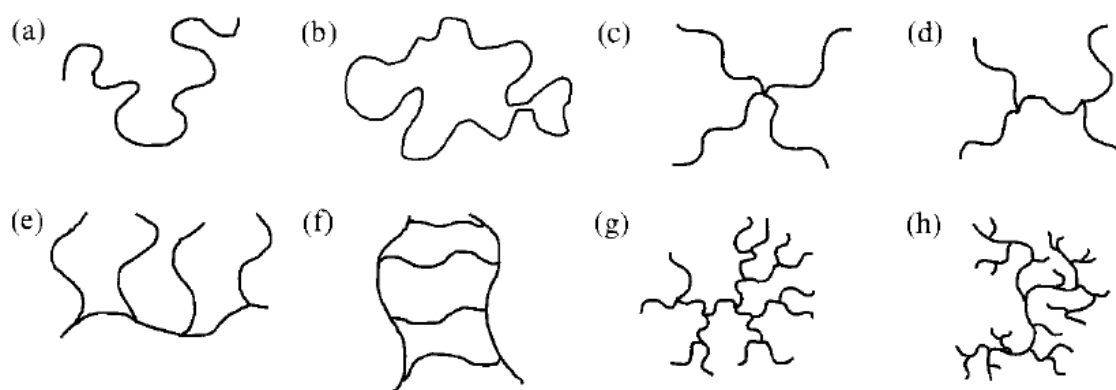
Figure 2-5   Examples of polymer architecture: (a) linear; (b) ring; (c) star; (d) H; (e) comb; (f) ladder; (g) dendrimer; (h) randomly branched[106].

The Nafion® membrane is a copolymer containing at least two monomers, i.e., a TFE back bone and perfluoro(4-methyl-3, 6-dioxa-7-octene-1-sulfonyl fluoride)[28]. A large

32

amount of polymer research work continues to be directed towards the study of molecular mechanisms governing their structure-property relationships. Among them, the stress-strain response of polymers has been recognized for a long time as one of the most informative properties [107]. Figure 2-6 shows the typical stress-strain curve for a NRE 212 membrane. Macroscopic nature of the mechanical behavior for the Nafion® membrane under the tensile stress before the rupture is characterized by an elastic response (Hook's law), followed by the strain hardening in the plastic deformation range after the yield point. These elastic and plastic deformation for the membrane is also time-dependent, i.e., viscoelastic and viscoplastic. The experimental data presented in the Solasi's work [3] clearly demonstrated the complicated non-linear time, hydration level, and temperature dependent behavior of the ionomer membrane.

33
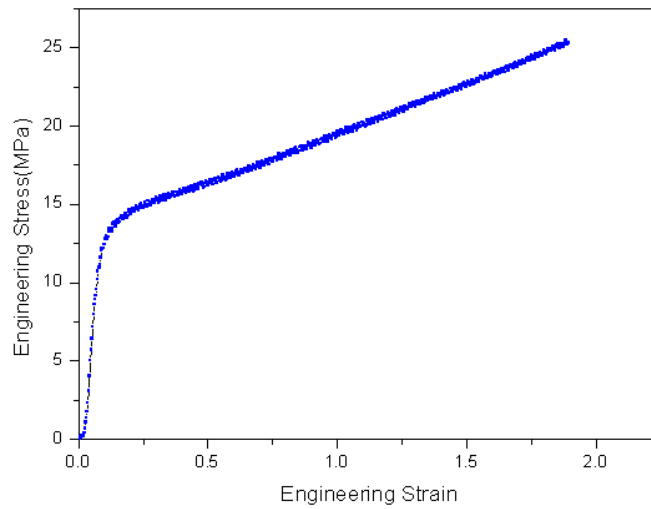
Figure 2-6   Tensile stress-strain curve of NRE 212 at room temperature with 10inch/min

strain rate

It is assumed that when an external load is applied to a polymer, the molecular bonds

experience stress, and in order to relieve themselves as much as possible, the chain segments

undergo internal rearrangements[107]; the way the polymer reacts to the external stress is

dependent on the magnitude and rate of the applied stress, chain morphology, environmental

factors such as humidity and temperature, etc. In literatures, it is believed that the Nafion®

membrane consists of at least two phases[44]; an amorphous and crystalline phase, and the

crystallinity for 1,100 EW membrane is in a range between 5 and 20%[108]. Therefore, it is

expected that each component contributes to the deformation resistance differently.

Early attempt to interpret this macroscopic behavior and establish a relevant

continuum model based on the understanding of microstructure of polymers was achieved by

Haward *et al.*[109]; the polymer's mechanical response can be described by two parallel processes acting together, one of which is the initial non-linear elastic up to yield point, governed by the secondary and intermolecular interactions, combined with the entanglement network response in parallel from interactions of the primary intramolecular and physical crosslink which give rise to an entropic contribution at large strains. As a continuous attempt for describing the mechanical behavior of polymers, specifically, ionomer membrane, the author propose a continuum model based on the Bergström and Boyce's model[110] introduced at 1998.

2.2.5 *Multiphysics modeling of PEM Fuel cell Incorporating structural mechanics*

Fundamental understanding of polymer electrolyte membrane fuel cell (PEMFC) material degradation and performance variation under various operating conditions requires numerical models that accurately describe coupled electrochemical, charge, mass, and heat transport, as well the structural response (deformation) of fuel cells. An integrated model representing the fluid, thermal, electrochemical and structural response was attempted in this work based on a finite element modeling technique that provides a unified method for analyzing these coupled phenomena.

35

The objective of the modeling work is to investigate the cell compression effect on fuel cell performance as well as the structural deformation and stress distribution. Mechanical deformation of fuel cell components, particularly the GDL, can impede gas and liquid transport due to the change of porosity and permeability via volumetric shrinkage. This, in turn, could lead to an increased mass transport loss in fuel cell performance. In addition, inhomogeneous pressure distribution on the lands and channels in the bipolar plates induces local current maximum at land area rather than the channel due to contact resistance at low current density, but the local current maximum can be shifted to the channel area if the overall load is increased because of an increase in the mass transport resistance [111]. It is attempted to develop a fuel cell model that captures the impact to cell performance due to the altered contact pressure distribution, the changed material properties as a result of cell compression. However, due to the difficulties of implementing a structural mechanics model in a commercial computational fluid dynamics (CFD) software which have been commonly used by fuel cell modelers, a little fuel cell modeling work has been reported to help understand and account for the cell compression effects. Hottinen et al.[112] considered inhomogeneous compression of GDL by utilizing experimentally evaluated parameters as functions of GDL thickness and they obtained a curve-fitted equation for porosity, permeability, and GDL in- and through-plane conductivities depending on amount of

36

compression. Su et al. [113] measured the permeability and porosity of the compressed and uncompressed GDL, and the measured data were averaged to obtain a mean average porosity and permeability value for computer simulation. In their modeling, constant values of porosity and permeability for compressed and uncompressed GDL were used, which is not the real case. Zhou et al.[114] developed a structural model to acquire the deformed geometry and material properties of GDLs and membrane in ABAQUS, and this information was implemented in a fuel cell model using COMSOL software.

In this research, we report a new scheme to build a multiphysics fuel cell model coupled with structural mechanics using COMSOL multiphysics software. COMSOL provides a deformed mesh computed from the structural mechanics that allows us to solve all the physics related to fuel cell operation in the deformed configuration. The gas transport, electrochemical reaction, charge conservation, etc. are solved in the deformed configuration, and the structural mechanics equations are solved in the reference configuration. To capture the effect of cell compression, the structure model was first solved to obtain an approximate geometry for the deformed configuration; then, the transport phenomena, electrochemical reactions, and charge conservation are solved in the deformed mesh induced by cell compression; finally the structural model is solved again to capture the stress/strain state in the PEM. This solution procedure was iterated until a converged solution is obtained.

37

CHAPTER 3   LOCALIZED MEMBRANE DEGRADATION

3.1 Introduction

Polymer electrolyte membrane (PEM) fuel cells are clean and efficient energy conversion devices, which can be used for powering future hydrogen fueled vehicles, residences, and portable electronics, among many other applications. However, cost and durability[11] are the two critical barriers for the commercialization of PEM fuel cells.   The performance degradation behavior and failure mechanisms for PEM fuel cells are strongly dependent on the specific applications/usage profile of the PEM fuel cell systems[1]. For example, fuel cells for automotive applications are expected to experience frequent variations of power output, which results in the frequent change of temperature and membrane hydration levels inside the PEM fuel cell stack.   Automotive fuel cells will also experience changes in environmental conditions, such as ambient temperature and air contaminants, etc. To be commercially viable, they must be durable enough to power the vehicle over a course of 5000 hrs without significant performance loss or catastrophic failure[12, 13]. With the current state-of-the-art technologies, PEM fuel cells still fall short of meeting the durability targets for automotive applications.

The performance degradation of PEM fuel cells is a combined effect of degradations in major fuel cell components: gas diffusion layer (GDL)[14] , bipolar plates (BP)[17], and

catalyst laery (CL)[24, 25], and ionomer membranes.   As a primary reliant component, the ionomer membrane electrolyte in the membrane electrode assembly undergoes a mechanical weakening process, which is not detectable with current in situ monitoring techniques. However, it can result in catastrophic membrane failure in the forms of perforations, cracks, tears or pinholes.   The mechanical weakening process can potentially determine the lifetime of PEM fuel cells[1, 11, 28, 29, 50].   The membrane degradation is commonly classified into mechanical and chemical degradation.   Mechanical degradation refers to the gradual reduction of mechanical strength and toughness. Chemical degradation refers to the chemical decomposition of the membrane, as evidenced in fluoride emission.   RH cycling is usually considered as a pure mechanical degradation process.   It can induce defects formation and growth due to cyclic stresses and strains in the membrane under the variations in temperature and humidity (hygro-thermal cycle) in the constrained fuel cell environment during the operation[1, 3, 11]. Chemical degradation of the membrane is believed to result from an attack to polymer chain by highly reactive free radicals (•OH, •OOH) generated via electrochemical or chemical reaction of crossover H_2 and O_2 [32] in the membrane and at electrodes[34, 115].   A recent publication by Madden *et al*[116] discussed the location of the membrane degradation, as well as the severity; it suggests a membrane degradation mechanisms based on direct radical generation on the Pt particles (dissolved from the

electrode and precipitated inside the membrane) from crossover hydrogen and oxygen. These radicals subsequently attacks the polymer by inducing the scission of polymer backbone and side chain, and the unzipping of the long-chain polymer[33, 34].

The mechanical and chemical degradation can be intertwined. A most striking effect of chemical degradation is the mechanical weakening of the membrane electrode assembly[49] and mechanical stress can potentially accelerate the rate of chemical decomposition reactions[117]. The authors believe that it may be conceptually advantageous to simply consider membrane degradation as a single process that have mechanical and chemical driving forces, and mechanical and chemical effects of consequences. Recently, the authors found evidence of membrane chemical degradation accelerated by mechanical stress with a gas phase Fenton's test[118]. This result leads the authors to believe that chemical degradation of fuel cell membranes can be related to the mechanical stress distribution, which are affected by hydration/dehydration, temperature variation, mechanical constraints, defects, etc.

It is the objective of this study to further understand the fundamental membrane degradation phenomena using a bi-layer membrane configuration. One of the difficulties in analyzing the membrane in fuel cells is that once the catalyst layer is coated onto both sides of membranes to form a MEA or Catalyst Coated Membrane (CCM), surface analysis of the

membrane becomes almost impossible; removing the catalyst layer without damaging the membrane is very difficult. As such, in order to characterize the degraded membranes, a bi-layer membrane method is proposed. More importantly, the bi-layer membrane allows us to see whether the mechanical strength/toughness loss is occurring uniformly across the thickness, or is only occurring locally in certain location of the membrane after fuel cell degradation tests. An accelerated fuel cell degradation testing was conducted under the OCV condition at 30% RH. After the OCV test, the bi-layer membrane can be separated into an anode-side and a cathode-side membrane for further analyses. The characterization methods include fluoride emission (FE), hydrogen crossover (Cross-over), and cyclic voltammetry (CV) measurement, uniaxial mechanical testing, FTIR spectroscopy, and SEM and EDS.

3.2 Experimental

Bi-layer membrane and CCM preparation— the use of bi-layer or multi-layer membrane has been reported in the literature for identifying the mechanisms of the membrane degradation. In this work, the configuration and fabrication of the bi-layer membrane are different from that of the earlier work[62, 68]. Catalyst inks were prepared by mixing a carbon-supported catalyst (TKK, TEC10EA50E, 47%wt Pt) with 5% Nafion solution (1100EW, Ion power, Inc), DI water, and methanol. The inks were stirred in

41

homogenizer for 3 hours and sprayed onto one side of a perfluorosulfonic acid (PFSA) membrane (NRE-211 from DuPont) using an semi-automatic spraying system built in house. Two one-side coated membranes thus prepared were stacked back-to-back and hot-pressed together for 30 minutes to realize one piece of bi-layer MEA as shown in Figure 3-1. The active area of the MEA was about 25 cm^2. The Pt loading as determined by weighting membrane before and after spraying is about 0.5 mgPt/cm^2 for the cathode and the anode catalyst layer. After our accelerated fuel cell degradation tests with the specified durations of tests, the two one-side coated membranes in the bi-layer MEA can be separated fairly easily and this procedure does not induce any damage on the samples. The backside of the MEA provides access to IR spectroscopy analysis.
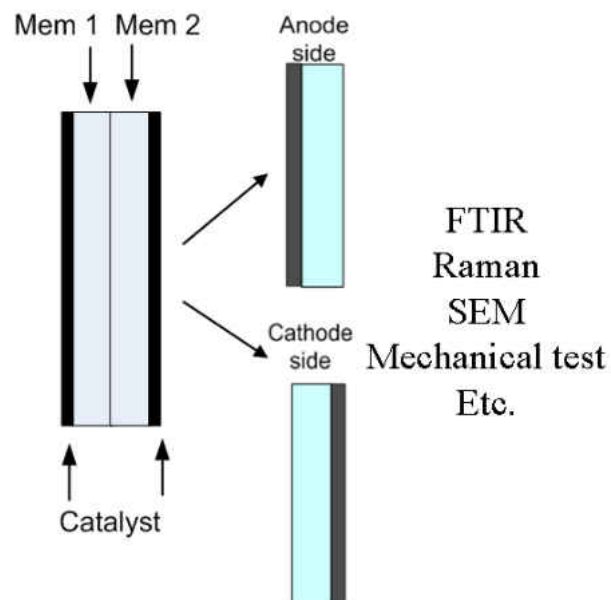
Figure 3-1 Schematic of the bi-layer membrane electrode assembly

42

OCV Hold Testing — The bi-layer MEAs were tested in a fuel cell test hardware (from Fuel Cell technologies, Inc.) with 25 cm^2 active area, single serpentine flow channels in a cross flow arrangement.   To assemble the test cell, carbon paper based gas diffusion media (10 BB from SGL Carbon Group) and PTFE gaskets were used; the pinch of the cell assembly was set at 0.125 mm (5 mils) per side.   Two OCV hold tests were performed. For both tests, the inlet gas humidity was set at 30% RH, the gas flow rate was set at 0.2 SLPM (dry base) without back pressure, the cell temperature was set at 80ºC, and the cell was hold at OCV.   In one test, H$_2$ and air were used for the anode and cathode gas feed, respectively; the test was run for 50 hrs.   The duration of the test was selected so that the two layers in the bi-layer MEA can still separated after the test.   It was found that longer OCV test (e.g. 100 hrs) under this condition would result in severely degraded MEA, which cannot be separated into two layers.   In the other test, 4% H$_2$ (balance nitrogen) and 100% O$_2$ were used for the anode and cathode side, respectively; and the test was run for 117 hrs. The duration of the OCV test with dilute hydrogen was longer than 50hrs because the membrane degradation in this test condition was not nearly as severe as that in the H$_2$/air OCV test, the two-layer MEA can still be separated and analyzed after 117 hrs of test.   The purpose of using different gas composition in the OCV hold test is to induce the platinum band formation at different locations in the membrane; it is expected that the platinum band

43

will form close to the cathode electrode in case of H_2 / air test, and close to the anode catalyst in the case of dilute hydrogen and pure oxygen test[27, 75].   Before the OCV hold test, the cell was wet up at 80 ℃ and 100% RH under H_2 / N_2 for three hours, then conditioned at 80 ℃ and 100% RH under H_2 / air with a load of 0.55V for three hours.   Cell diagnostic tests were performed after the break-in procedure; these include cell polarization curve, hydrogen cross-over rate, and cyclic voltammetry (CV).   Both cross-over and CV tests were conducted at 25 ℃ and 100% RH.   A scan rate of 30 or 40mV/s from 0 to 0.8V was used for CV test and a scan rate of 2mV/s was used for the hydrogen cross-over test. Electrochemical area (ECA) was calculated using the specific capacity of 210 $\mu C/cm^2$ for the hydrogen under-potential adsorption-desorption on the platinum surface.   The ECA values reported in this paper is the average of the hydrogen adsorption and desorption areas.   Water was condensed and collected from the anode-side and the cathode-side exhaust gas steams. The fluoride ion concentration in the water was measured by a fluoride ion selective electrode (ISE).   After the OCV hold test, the cell diagnostic tests were performed again.

Uniaxial Mechanical Testing — After the OCV hold, mechanical tests were conducted to measure the residual mechanical strength and toughness of the membrane. The bi-layer membrane was carefully delaminated into two one-side coated membranes, namely the anode-side and the cathode-side membrane.   The membrane was cut into the

44

multiple test strips approximately 4~6mm wide and about 60mm long.   The test strips still contain the catalyst layer on one side.   Then, each strip was mounted on and tested with an in-house built mechanical testing system consisting of two clamp-type sample grips, a linear actuator, a load cell, data acquisition instrument, etc.   The uniaxial stress-strain curve for each strip was obtained at 254 mm/min pulling rate at ambient conditions.   The stress was calculated based on a cross-section area calculated from the measured width of the strip and the nominal thickness of the membrane.   For comparison purpose, the stress-strain curves of the one-side coated membrane in as-fabricated condition (control sample) and the bare membrane (without catalyst layer) were also obtained.

FTIR spectroscopy — For the FTIR measurement, the membrane sample was converted to the potassium salt form via the procedure as explained in the literature [80] to measure the C=O peak.   The FTIR spectra were obtained for the bare side (without catalyst) of the MEA samples using an FTIR spectrometer (HORIBA, LabRam-IR) with an Attenuated Total Reflectance (ATR) contact probe.   The FTIR spectra were collected as the average of 32 scans with a resolution of 4 cm^{-1} in a range from 600 to 4000 cm^{-1} in absorption mode.

SEM & EDS — Scanning Electron Microscopy (SEM) and Energy Dispersive X-ray Spectroscopy (EDS) were used to characterize the microstructural and compositional change of MEA before and after the accelerated degradation testing.   The MEAs were cut and

45

potted in epoxy, ground with abrasive papers, and finally wet polished using diamond suspension.   The polished and dried samples were sputter-coated with Au-Pd coating.   The SEM image was taken on a Hitachi S3500N scanning electron microscope using a back-scattered electron detector.   A Thermo Scientific Noran system 7 with a SiLi EDS detector was used to characterize Pt distribution across MEAs with an accelerating voltage of 25 KeV. EDS scan was carried out on small rectangular region with an area about 38.5 ($\pm$ 1.48) μm^2. For each rectangular area analyzed, the percentage of Pt atoms with respect to the total number of Pt and Au atoms was obtained.   Five rectangular areas across the electrolyte sample were examined and the atomic percentage of Pt for each area was plotted versus the distance between the geometric center of the rectangle to the electrode/electrolyte interface.

3.3   Results and discussions

H$_2$ / Air fuel cell

The OCV decay profile is shown in Figure 3-2 and pre- and post-performance diagnostic data are tabulated in Table 3-1.   The fluoride content was measured in the anode side and the cathode side effluent water collected periodically during the OCV hold test.   It is found that the cathode side exhaust water contains more fluoride than the anode side, which is consistent with trend observed in similar tests[119].   The hydrogen cross-over rate increased by a small amount (<1 mA/cm^2) after the OCV testing, the observed OCV decay

46

can not be solely attributed to the slight increase of the hydrogen crossover. The polarization curves and cell ohmic resistance before and after the OCV hold test are plotted in Figure 3-3. The cell resistance of the fuel cell after the OCV hold test appeared to be comparable with that before the test and therefore, the performance decay would result mainly from a combination of an increase of electrode proton resistance, and oxygen kinetic and mass transport loss due to the electrode morphology changes and/or adsorption of membrane degradation species[120].
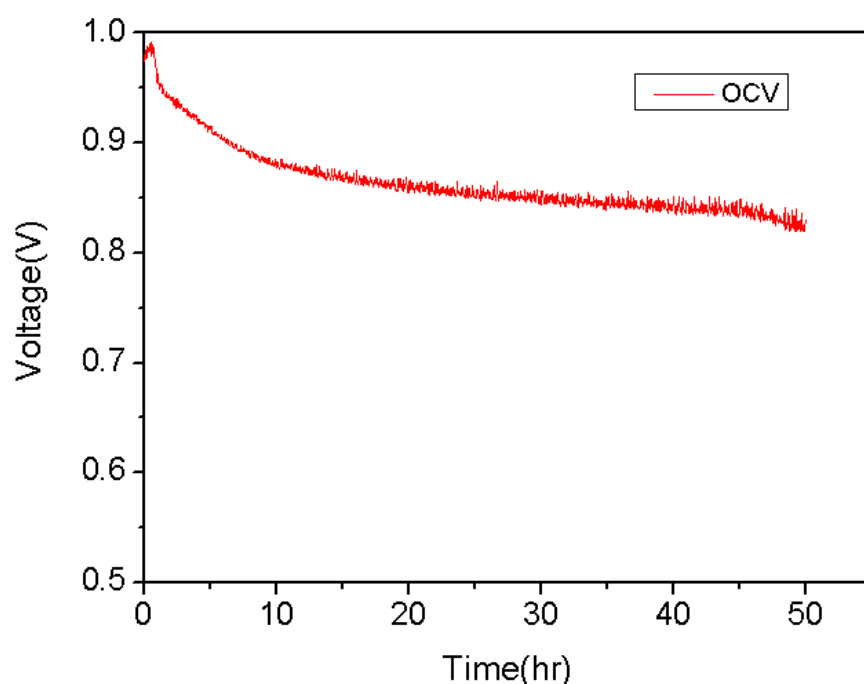
Figure 3-2 Open circuit voltage decay during the 50hr OCV test with H_2 and air as reactants.

Table 3-1 Performance diagnostic data of the bi-layer membrane fuel cell before and after the

H$_2$/Air 50hr OCV hold test

Sample	Fluoride loss (μmol/cm^2)		Cross-over rate before / after OCV test (mA/cm^2)	ECA changes after OCV test (m^2 Pt/ g Pt)
	Anode	Cathode		
Bi-layer membrane	19.45	30.95	0.6 ($\pm$0.014) / 0.67($\pm$0.036)	4% decreased
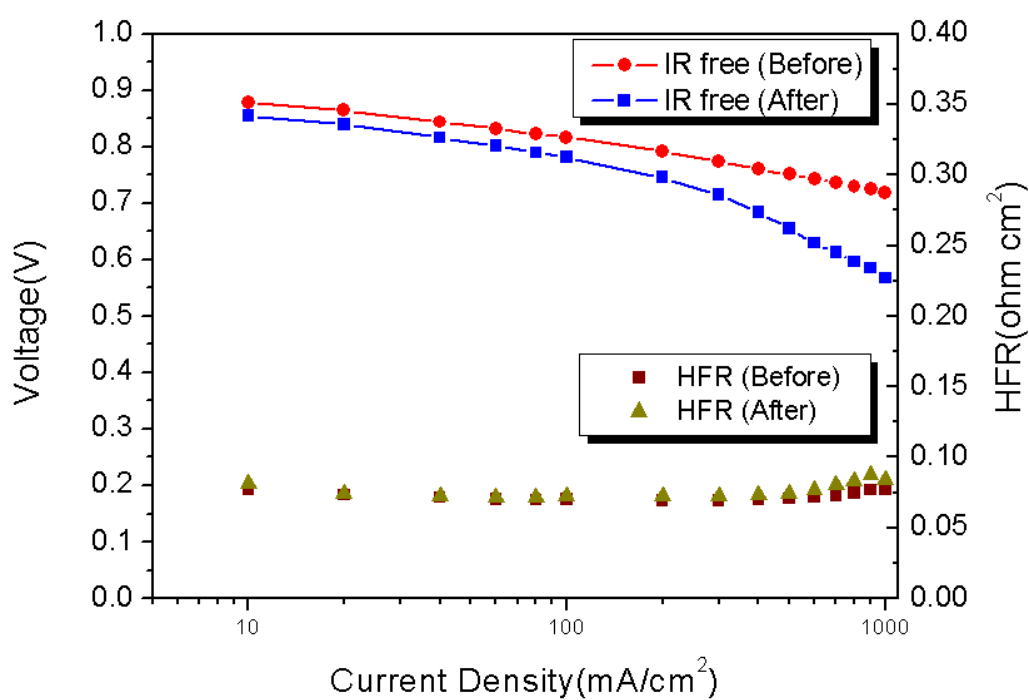
Figure 3-3   Semi-log plot of IR-free cell voltage before and after the 50hr OCV test

48

The life time of an MEA is frequently limited by the mechanical breaches, such as pinholes or cracks, which result in rapid reactant cross-over and subsequent cell/stack failure[29, 30, 49]. The material weakening and formation of mechanical defects can be revealed by a stress-strain testing. Figure 3-4 shows the stress strain behavior of the anode- and the cathode-side of the bi-layer membrane and the behavior of the control samples are superimposed in each graph.

(a)

Cathode side membrane
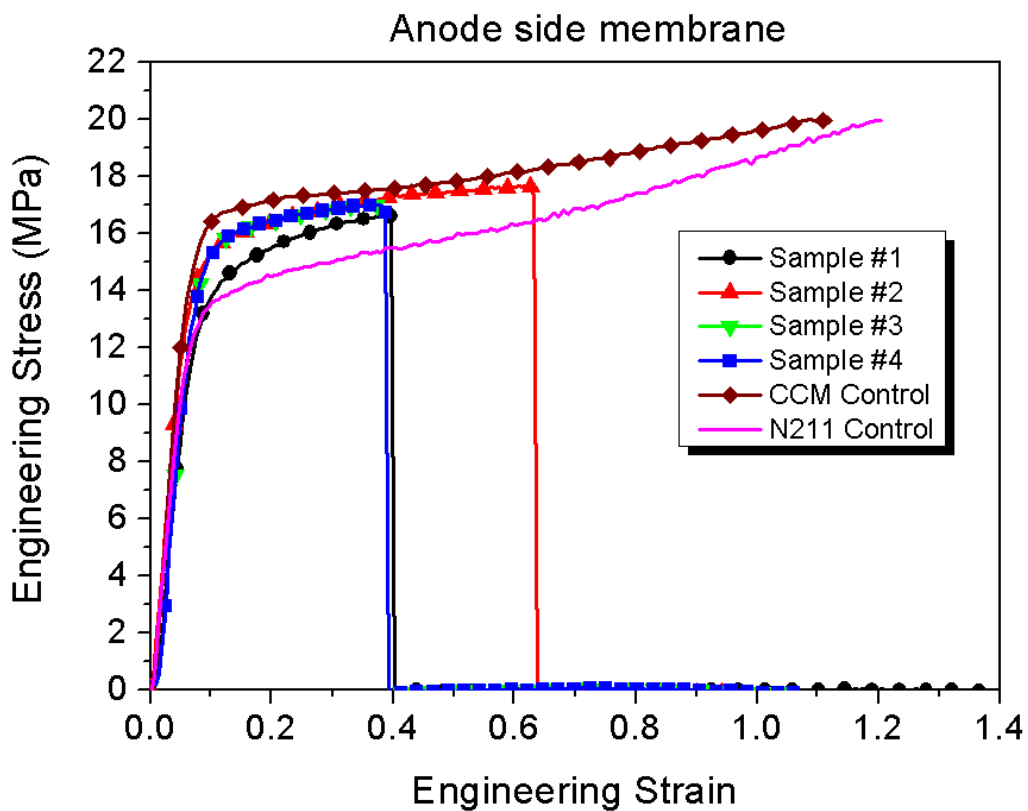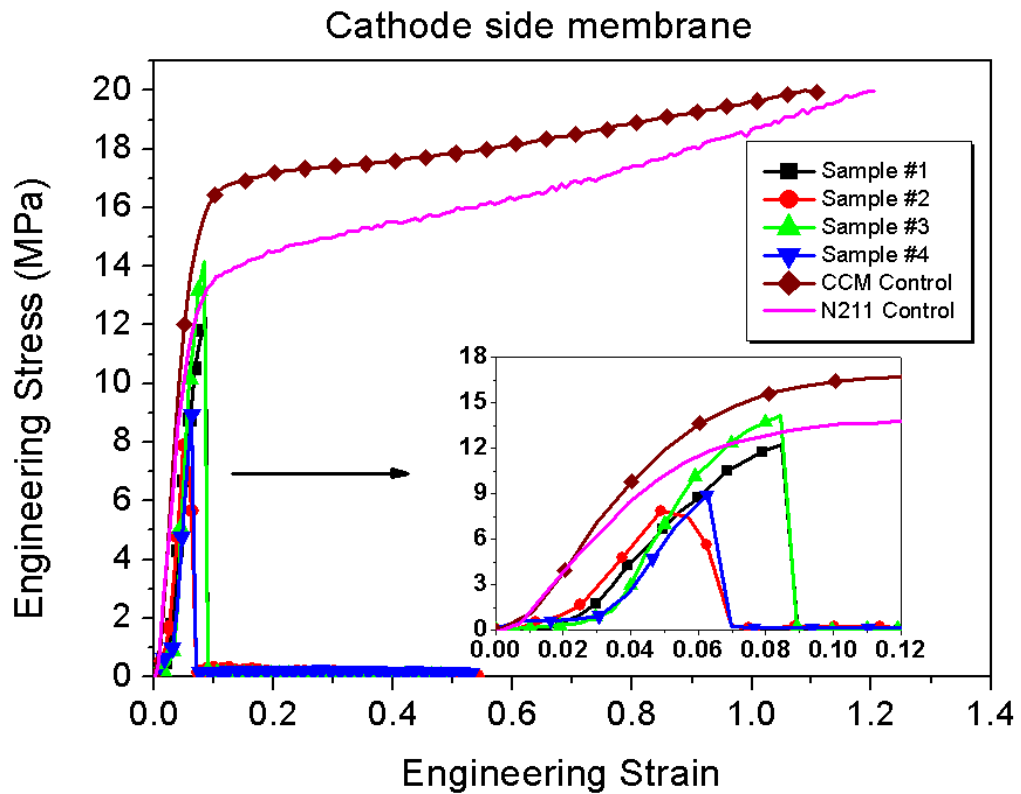
Figure 3-4 The stress-strain curves (a) for the anode and (b) cathode side of the bi-layer

membrane at room temperature after OCV test with H_2 / Air

The apparent increase of the yield strength of CCM control samples compared to that

of the NRE-211 control membrane is due to the fact that catalyst electrode thickness are not

factored into the nominal cross-section area of the sample. The strain-to-breaks for control

samples were reproducible to 3% for the N211 samples and 6% for the CCM control samples.

The strain-to-break for the CCM control is comparable to that of the NRE-211 control sample,

indicating that the catalyst layer bonded to the membrane does not introduce mechanical

defects to the assembly.   The typical stress-strain behavior in Figure 3-4 can be qualitatively

described by the initial Hookean elasticity until the stress developed becomes sufficiently

large to produce a plastic deformation at the imposed rate and as the elongation proceeds, the

stress increases with strain referring to the strain hardening, eventually leading to its final

rupture; it is generally believed that the rupture of the polymer is induced by a defect

formation and accumulation such as microcracks and crazing[121, 122]. As can be noticed

easily, it is observed that the mechanical strength and toughness of both the anode-side and

the cathode-side membrane were reduced from the initial values.   The modulus of toughness,

an indicator of the mechanical toughness of the membrane, can be calculated by the area

under the stress-strain curve and represents energy per unit volume needed to rupture the

material. When comparing the anode-side and the cathode-side membrane, the cathode-side

membrane lost more mechanical toughness than the anode-side membrane. Also, the

behavior at the cathode side membrane exhibited the similar behavior with the degraded

single MEA [50]. These results suggest that the membrane degradation is not uniform

through the thickness direction, and the membrane close to the cathode side is degraded more

than the membrane close to the anode side.   This observation is consistent with other

experimental evidences in literatures[34, 75, 100].   The platinum band formation is close to

the cathodes under H_2 / Air OCV test condition.   Based on the theory of direct radical

51

formation on Pt, it is expected that the formation of the radicals at the cathode side membrane is accelerated by the platinum particles. This results in the more severe decay of the mechanical toughness for the cathode-side membrane.

Each one-side coated membrane was examined under the FTIR before the ion-exchanging, it was confirmed that the spectrum from the two CCM of the anode- and the cathode-side are identical with that of the control sample. This suggests that the interface of the bi-layer CCM does not show any differences in chemical composition compared to the control sample and it is difficult to study membrane degradation under the FTIR without ion-exchanging. The FTIR spectra of the samples after ion-exchanging are shown in Figure 5.

The results indicate that the concentration of the carboxylic end group increased in the degraded membrane, which can be identified by the C=O peak at 1690 cm-1 for both anode-side and cathode-side of membranes; however it is not observed in the control sample.   The band at 1630 cm-1 is assigned to the HOH fundamental bending mode [123-125]. Note that the intensity of C=O peak in the cathode-side membrane is only slightly higher than that in the anode-side membrane, even though the cathode-side membrane exhibited more severe degradation than the anode-side membrane.   Some of the degradation species might have been washed out by effluent water and disappeared.   Also the penetration depth of the ATR probe is not deep enough to reveal the overall state of degradation; the typical penetration

52

depth of the ATR ranged from 0.1 ~ 2μm. So the FTIR results do not reveal the concentration

of C=O peak within the bulk of the 25 μm thick membrane.
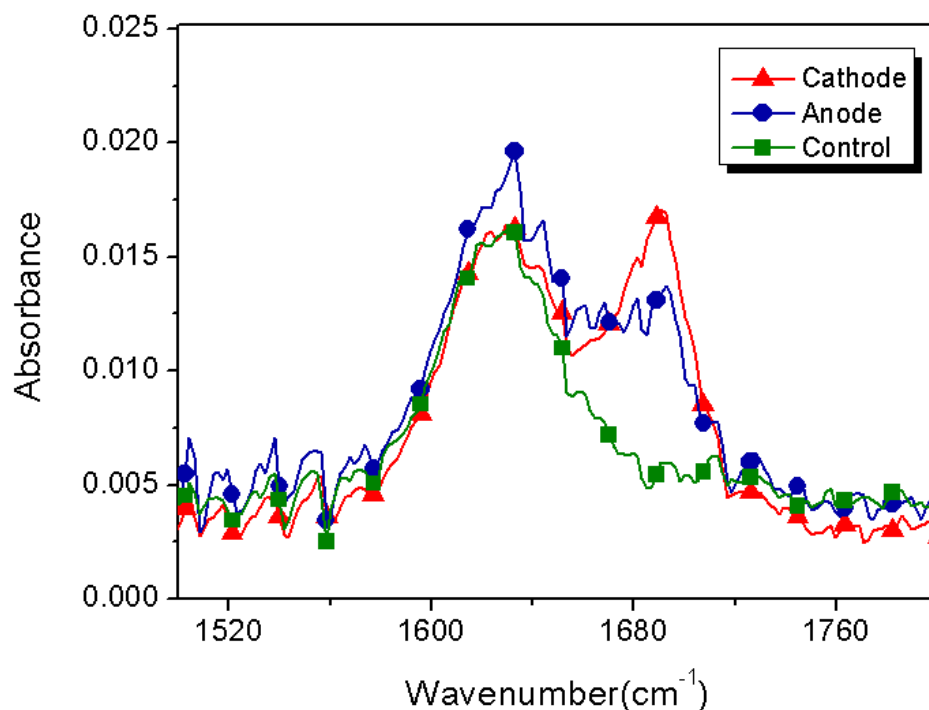
Figure 3-5 C=O peak (1690 cm^{-1}) in FTIR spectra of the bi-layer membranes after the 50hr

OCV test

FE and mechanical test results reveal that the cathode-side membrane has degraded

more than the anode-side membrane under 50hr OCV test in the H_2/air OCV hold test.   The

SEM images for that membrane were shown in Figure 6(a~c) for comparison. Based on the

53

images, a 10 ~ 20% reduction of thickness was found for both the cathode-side and anode-side membrane in Figure 6(a~b).

(a)

(b)

54
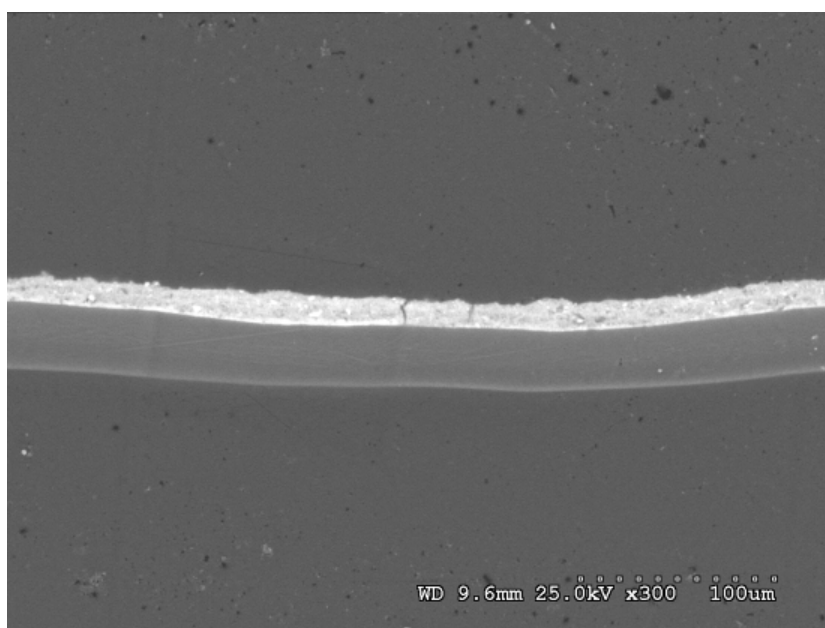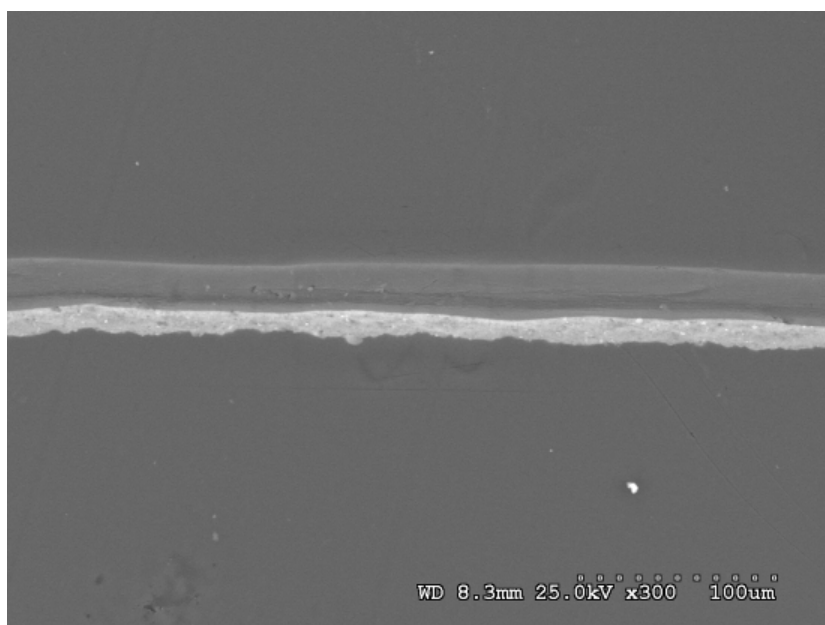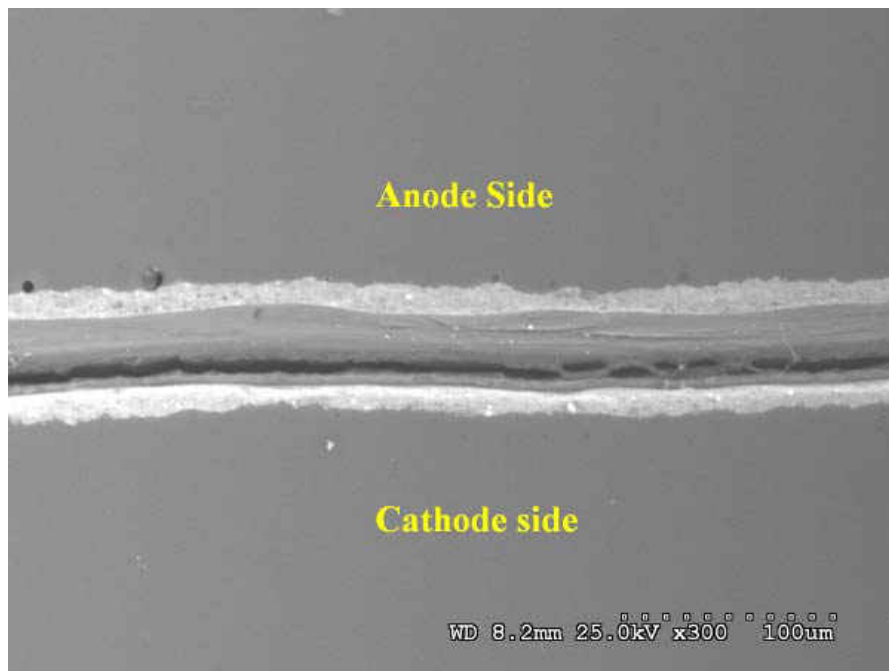
(c)

Figure 3-6 SEM images of (a) anode side membrane, (b) cathode side membrane after 50hr

OCV test, and (c) both side of membrane after 100hr OCV test

In a preliminary test to verify the application of the bi-layer configuration, the bi-layer

cell was tested under OCV hold for 100hr.   After this test, the bi-layer membrane showed

severe degradation and can not be separated into two integral pieces.   The SEM image of

this MEA (with bi-layer membrane still bonded together) after the OCV test is shown in

Figure 3-6(c).   A long crack and some micro-cracks were observed close to the cathode side

electrode. The SEM sample preparation includes mounting the MEA sample in the holder,

polishing, and storing in the vacuum before running the SEM and it is, therefore, believed that the macro and micro-crack in the cathode side membrane in Figure 3-6(c) was likely caused by a tensile stress inside the membrane due to the drying out of the membrane in the storing phase. It is also indicative of degraded membrane, because crack was not observed in the other SEM samples being processed by the same procedure. Based on the SEM images, without noticeable membrane thinning, the brittle behavior of the degraded membrane in the uniaxial tensile test is likely caused by defect formation due to the localized membrane degradation.

Last but not least, the atomic ratio of Pt and Au distributions across the anode and cathode membrane were collected by SEM-EDS in Figure 3-7 and the results showed clearly the peak location of Pt atomic ratio close to the cathode electrode. The Pt peak was not observed in the anode side membrane considering the relatively large standard error of the EDS technique. This means that the Pt elemental concentration is too low to be quantified by EDS measurement. The Pt atomic ratio in electrodes is $87 \pm 0.55\%$ with respect to Au and the standard error for Pt ratio in the cathode membrane is within ± 2.16. This inhomogeneous distribution of Pt particles in the membrane is believed to be a contributor to the localization of membrane degradation confirmed by FE, and mechanical testing results.
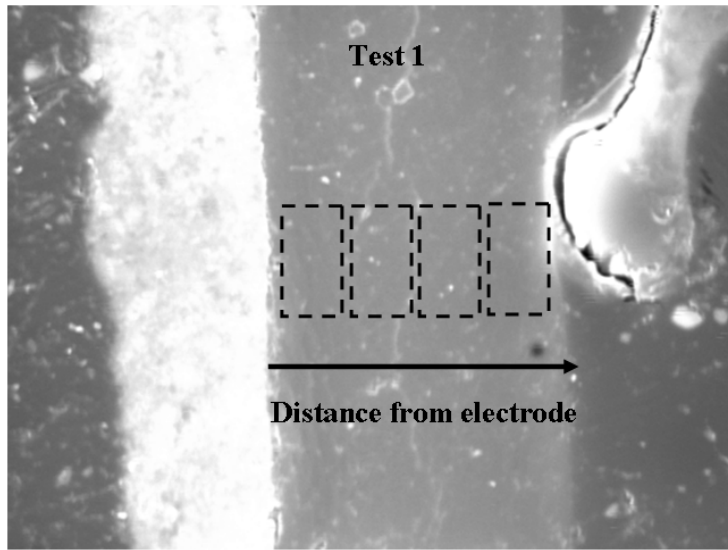
(a)
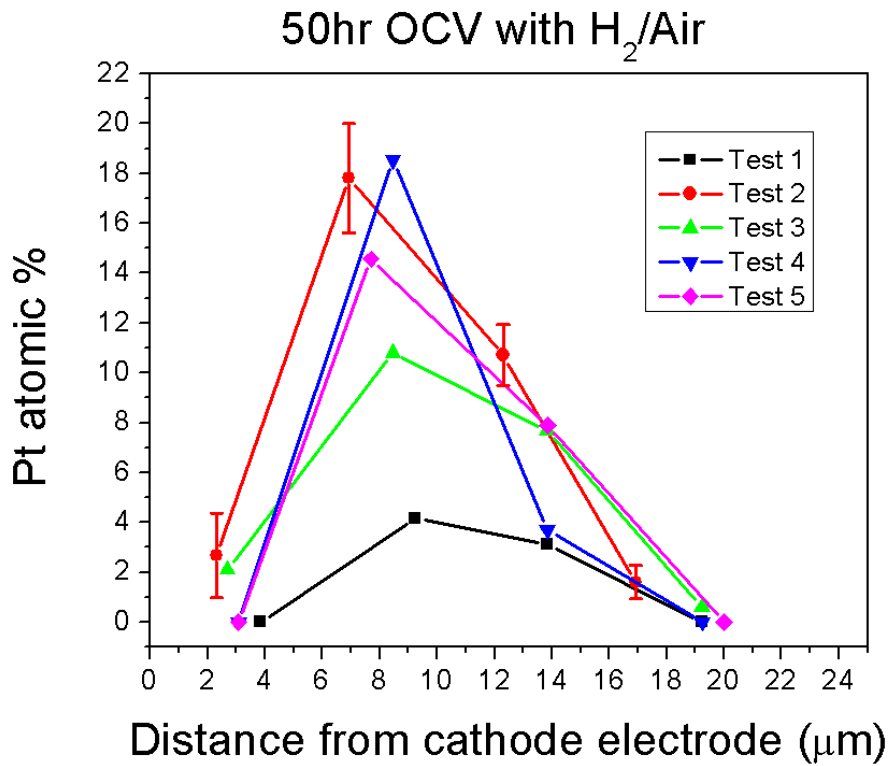
(b)
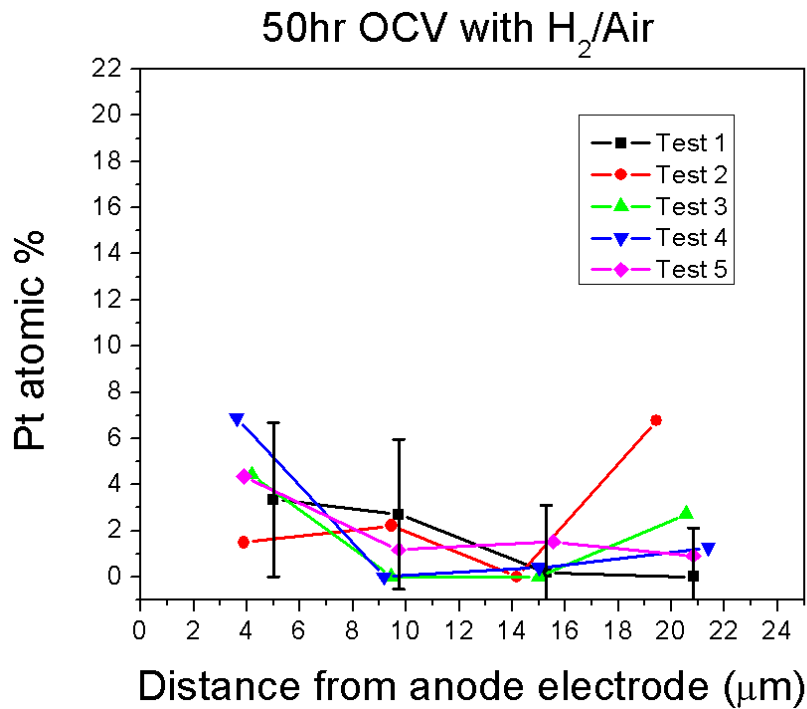
(c)

Figure 3-7 (a) The areas (rectangles) analyzed in the cathode-side membrane ; (b) Pt atomic

distribution measured from the SEM-EDS in the cathode-side membrane and (c) the anode-

side membrane after 50hr OCV test with H_2 / Air

4% H_2 (Balance Nitrogen) / 100% O_2 cell

The membrane degradation under the OCV condition of H_2 and air fuel cell is found

to be more severe in the cathode-side membrane rather than the anode-side membrane. In

order to further investigate the platinum band effect on membrane degradation, an experiment

is designed to induce the formation of platinum band in anode-side membrane. Experimental

results from several groups have proven that the concentration or partial pressure of hydrogen

58

and oxygen (on the anode- and the cathode-side respectively) can affect the location of the platinum band in the membrane.   The location of the Pt band moves toward the anode with a decrease in the hydrogen concentration and an increase in the oxygen concentration [22, 27, 75].   In this experiment, dilute hydrogen is fed into anode and pure oxygen into cathode to induce the platinum band formation in the membrane layer close to the anode side.   The cell was held under the OCV condition for 117 hrs.
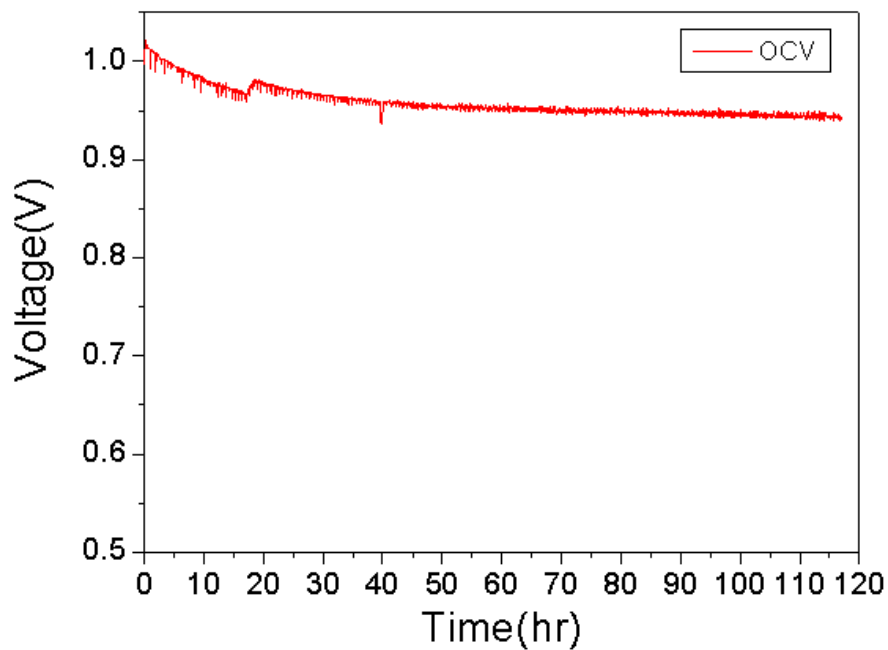
Figure 3-8 Open circuit voltage profile during the OCV test with 4%H_2 (balance N_2) / 100% O_2

The anode inlet gas contains a stream of nitrogen with a controlled amount of hydrogen mixed in via a precision mass flow controller; the ratio of the volume flow rates of

59

hydrogen to nitrogen gas is maintained at 1:24. The observed OCV decay behavior is shown in Figure 3-8. Interestingly, the OCV starts at a relatively high value around 1.02 ~ 1.03V, it decays slightly for a first 30hrs, and then stays at a constant value around 0.94V till the end of the test end. This OCV decay behavior is very different with the large drop of OCV observed in the 50-hrs H_2/air OCV test. The high OCV at start results from the high oxygen partial pressure at cathode which is very close to the theoretical mixed potential of 1.06V [126]. The drastic change of OCV decay behavior is thought to be directly or indirectly related to the reduced amount of H_2 cross over from the anode to the cathode side. Comparing to the H_2/Air OCV test, the hydrogen cross-over rate in the 4%H_2/Air test will be likely 25 times lower. One explanation for this change of the decay behavior can be linked to the recent work of Sugawara *et al.*[120], who have shown that sulfate ions (as a result of membrane degradation) migrated and specifically adsorb onto the platinum catalyst is a major contributor to the OCV decay. The lower hydrogen concentration, the lower the rate of membrane degradation, and the less the sulfate ion produced. The lower hydrogen concentration can also shift the location of membrane decomposition sites closer to the anode, hence more sulfate ion will migrate and adsorb onto the anode-side catalysts rather than the cathode-side catalyst. Adsorption of the sulfate ions on the anode electrode should not affect the OCV significantly because of the intrinsic high activity for hydrogen oxidation reaction.

60

The much reduced OCV decay rate at low H_2 partial pressure is believed to be the results of these effects.

Table 3-2 Performance decay of the bi-layer membrane fuel cell with $4\%H_2$ (balance N_2) /$100\% O_2$ during the 117hr OCV hold test

Sample	Fluoride loss (μmol/cm2)		Cross-over rate before / after OCV test (mA/cm^2)	ECA changes after OCV test (m^2 Pt/ g Pt)
	Anode	Cathode		
Bi-layer membrane	50hr		0.98 ($\pm$ 0.03)/ 0.77 ($\pm$0.044)	8% decreased
	6.78	3.14		
	50 ~ 100hr			
	16.60	7.16		

The polarization curves and cell ohmic resistance before and after the OCV hold test are plotted in Figure 3-9. Table 3-2 summarizes the test results.   It is interesting to find that the FE of anode side was greater than that from the cathode side, contrary to the pattern observed in the OCV test with H_2/Air as reactants.   The OCV hold test under $4\% H_2 /O_2$ resulted in much lower FE (even over a longer period of time) than the OCV hold test under H_2/Air.   This behavior is believed to be the result of a lower rate of radical generation due to a lower H_2 crossover rate. The FE data also suggests that in $4\%H_2 / O_2$ test, the degradation rate of the anode side membrane was higher than that of the cathode side. The decrease in the

ECA can partially support the platinum loss. However, cross-over rate after the test did not

increase at all, even though the FE results show the evidences of membrane degradation.
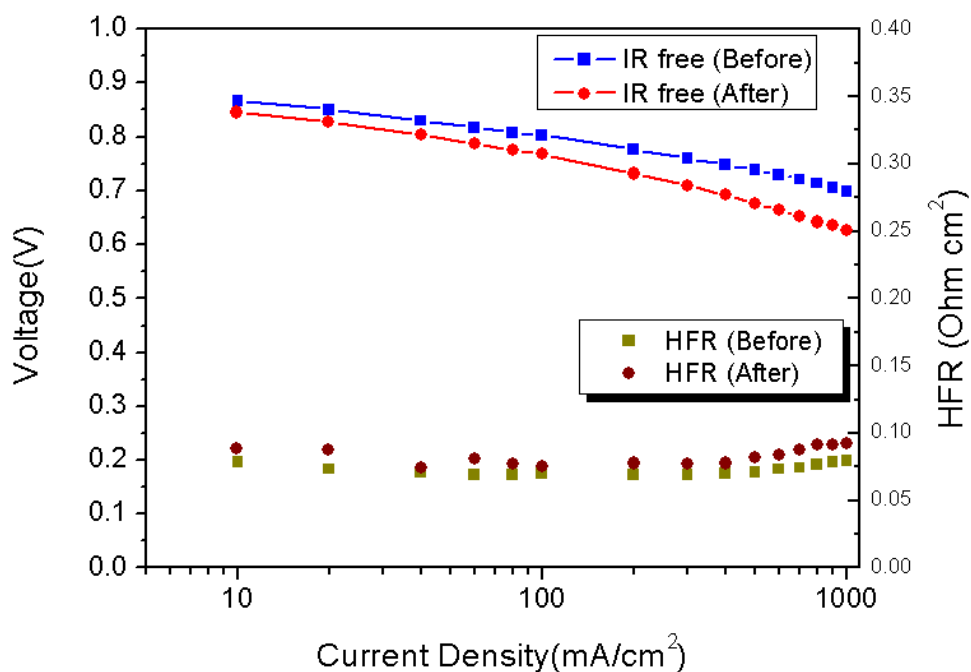
Figure 3-9 Semi-log plot of IR-free cell voltage before and after 117 hrs of OCV test with

4%H_2 (balance N_2)/ 100% O_2

The mechanical test results of the membranes are shown Figure 3-10. For the

comparison purposes, the results from the control samples were also plotted in the same

graph. From the stress-strain curves, the ductility of the anode-side membrane degraded

severely; however the cathode-side membrane did not show any sign of mechanical

degradation, and this is rather surprising.

62
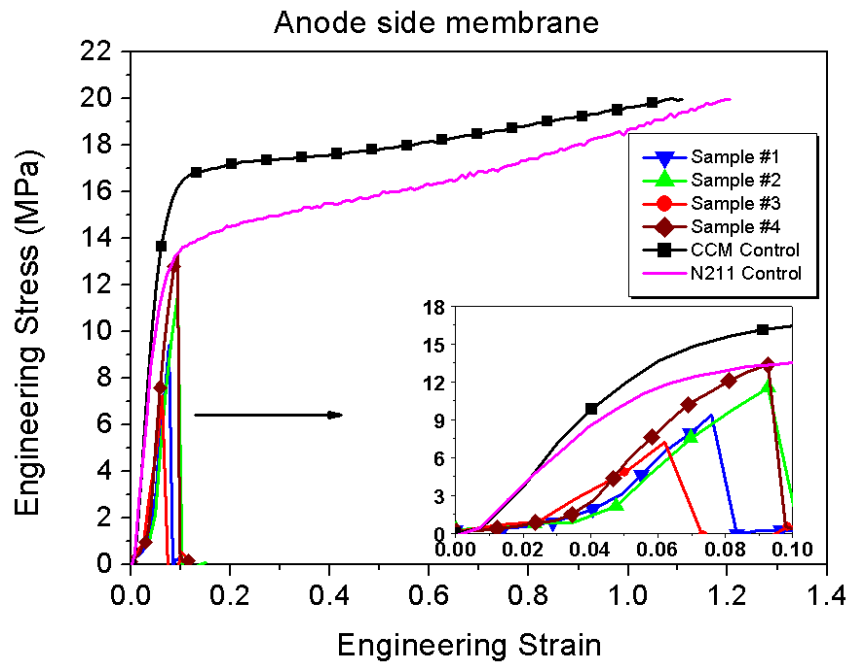
(a)
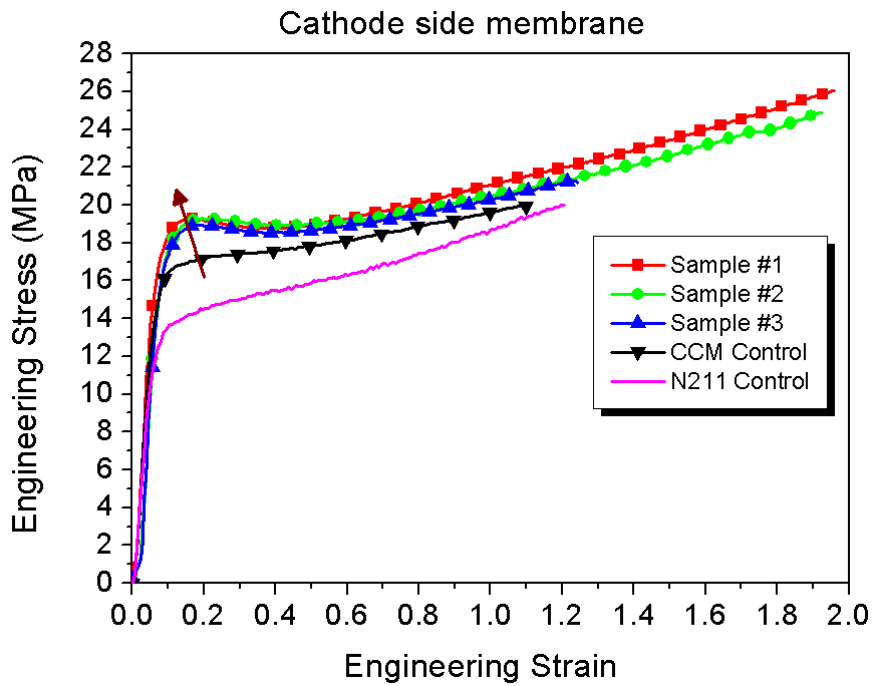
(b)

Figure 3-10 The stress-strain curves (a) for the anode and (b) cathode side of the bi-layer

membrane at room temperature after 117hr OCV test with 4%H_2 (balance N_2)/ 100% O_2

63

Both the FE and mechanical test data suggested that the loci of membrane degradation have shifted to the membrane near the anode side. This is very likely related to the platinum band shift. The mechanical properties of the cathode-side membrane has improved rather than deteriorated, which can be characterized by an increase of the yield strength (denoted by an arrow) and the strain-to-break. The increase of the yield strength was not observed for membranes after the OCV test with H_2/Air shown in Figure 3-4. Mechanical property changes of polymer materials with time, such as the yield strength, elastic modulus, etc, are commonly the result of physical aging, which can cause the increase of yield strength, followed by strain softening[105, 127]; it is distinguished from the chemical aging (degradation) relating to permanent chemical structure modification and breakdown of primary atomic bonds. Physical aging is a slow process for polymer to establish equilibrium from a non-equilibrium state. During the processes, many properties of the material such as creep and stress relaxation rates, electrical properties, etc. can be affected and change with time[127]. Aging polymer even entails a decrease in the diffusivity of gases in the polymer and this might be part of the reason why the hydrogen crossover rate did not increase after the OCV test, even though an observable membrane thinning has occurred.

64
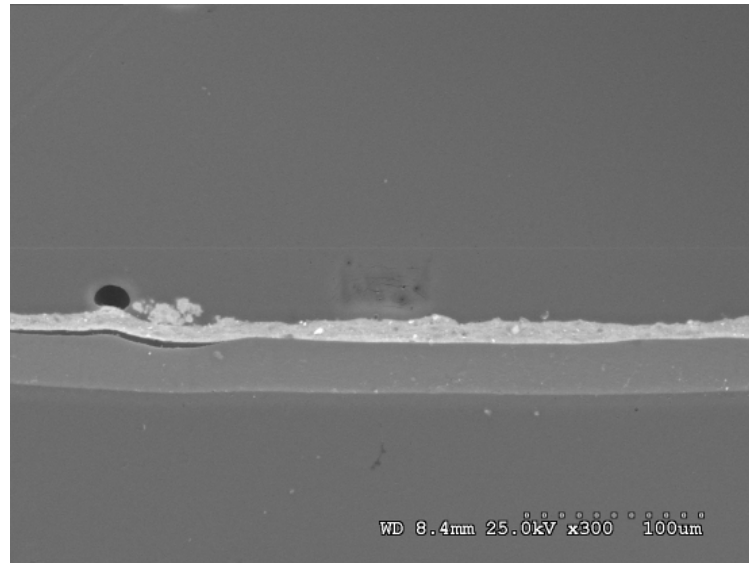
(a)
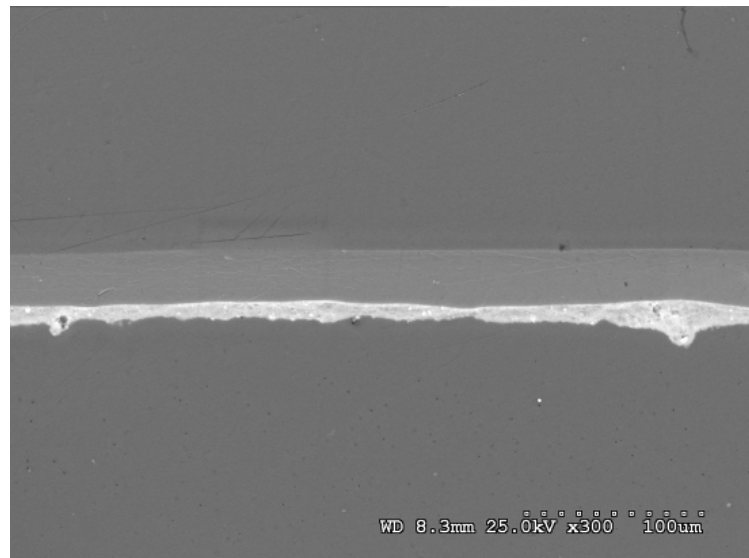
(b)

Figure 3-11 SEM images of (a) the anode-side membrane and (b) the cathode-side membrane

after 117 hrs of OCV test with 4%H_2 (balance N_2)/ 100% O_2 fuel cell

65

SEM images of both the anode-side and the cathode-side membrane are shown in Figure 3-11. The images indicate about 10% thinning of the anode-side membrane. FTIR analysis did not reveal any C=O peak in either membrane, again this is likely due to the low penetration depth of ATR probe. The entire spectra from both membranes are as similar as that of the control sample. Further more, the lower chemical degradation rates indicated by FE implies low concentration of residual carboxylic acid groups. For the anode-side membrane, the location of membrane degradation is likely closer to the anode electrode. Note that the Pt band will also form closer to the anode electrode in the anode-side membrane. The EDS spectra of the anode-side and the cathode-side membrane are shown in Figure 3-12. The Pt atomic ratio in the vicinity of anode electrode has a peak that is higher than any other locations; the spectra for the cathode-side membrane did not show any Pt peak. Further material characterizations, such as EPMA, TEM, have been planned. The authors hopefully can acquire a more precise picture of the Pt distribution in these membranes after the OCV test.

66
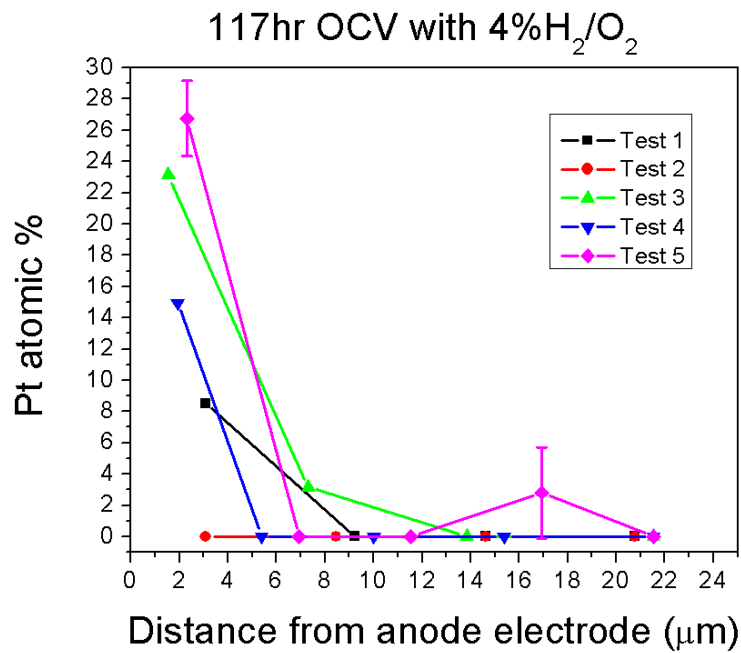
(a)
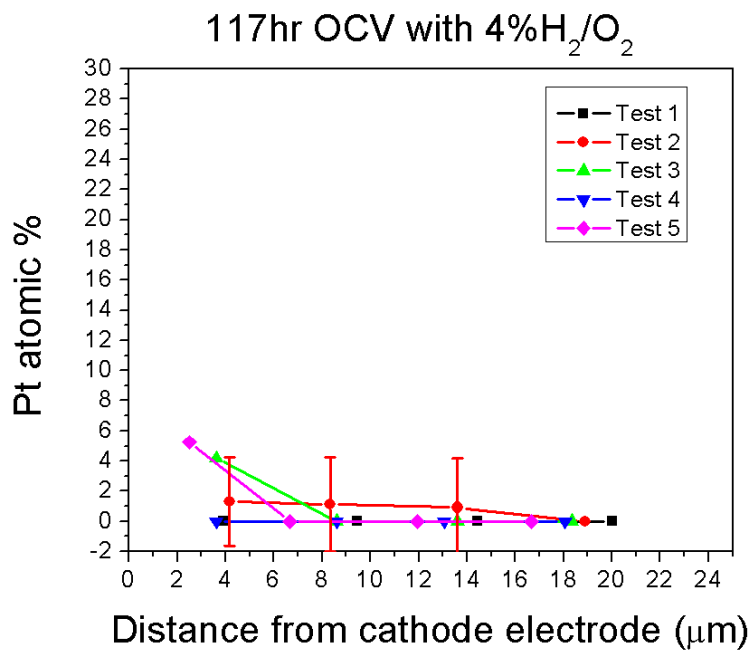
(b)

Figure 3-12 Pt atomic distribution measured from the SEM-EDS (a) in the anode-side membrane and (b) the cathode-side membrane after 117 hrs of OCV test with $4\%H_2$ (balance N_2)/ 100% O_2

CHAPTER 4   MECHANICAL STRESS INDUCED CHEMICAL DEGRADATION

4.1 Introduction

The durability of membranes is ultimately limited by the physical breach of the membrane in the form of pinholes or cracks, which results in rapid reactant cross-over and subsequent cell/stack failure[29, 30, 49]. During the membrane degradation process, thinning, weight loss, fluoride emission, and crazing formation have been observed.   Huang *et al.*[49] reported that significant reduction of membrane ductility can be identified as considerably reduced strain-to-break of the membrane after open circuit voltage (OCV) hold and relative humidity (RH) cycling tests. Post-mortem analysis indicated the formation and growth of mechanical defects such as cracks and crazing in the membranes and MEAs after RH cycling. The authors [50] recently studied mechanical properties of recast reinforced composite membranes with ePTFE (Tetratex®) and observed that the mechanical strength and toughness of the membrane reduced significantly after an OCV hold testing for 100 h.   SEM analysis also confirmed that localized cracks form inside the membranes. Tang *et al.*[51] conducted cyclic stress tests on membranes and found that the dimensional change of the membrane was observed and the microstructure rupture was identified on the surface of the membrane at the cyclic stress over 3.0 MPa. This result indicates that the PEM can be fractured under much lower stress than ultimate strength when it is subjected to the condition

of fatigue. The author also reported that the stress induced by temperature variations is much smaller than the stress under RH cycling tests. However, they concluded that the membrane degradation is accelerated significantly when the membrane was subjected to temperature and humidity cycling conditions simultaneously.

Chemical degradation refers to the chemical decomposition of the perfluorosulfonic acid (PFSA) membrane. It is commonly believed that PFSA membrane is attacked by highly reactive oxygen radicals ($\cdot OH$, $\cdot OOH$) generated by an electrochemical or chemical reaction of hydrogen and oxygen on the platinum catalysts[32, 60-62] or decomposition of H_2O_2 catalyzed by transition metal ions[63]. Pozio *et al.*[63] postulated that the free radical attacks of the perfluorinated molecular chains with weak bonds are responsible for the membrane degradation. The radicals are derived from H_2O_2, which can form from a two-electron oxygen reduction at the cathode[4, 64] and from oxygen molecules permeated through the membrane from the cathode to anode[4]. The hydrogen peroxide was clearly observed within a PEM fuel cell membrane when H_2 and air are present as gas inputs by an *in situ* experimental technique[60]. This H_2O_2 can diffuse into the membrane and chemically breaks down into hydroxyl radicals assisted by metal ions present in the membrane[63-65]. *In situ* radical formation has been detected at the cathode side of the polymer membrane by electron spin resonance (ESR) techniques[66].

The decomposition mechanism of the membrane by radical attacks to the polymer weak end group such as $-CF_2COOH$ is introduced by Curtin *et al.*[28]. Others also suggested that sulfonic acid groups may be the key to the radical attack mechanism[104, 128] and it is recently reported that the chemical degradation rates of PFSA based membranes under OCV conditions are dramatically reduced by incorporating cerium and manganese ions into the MEA structure [129].

Based on evidence in the literature, membrane failure is believed to be the consequence of the combination of chemical and mechanical effects acting together. Reactant gas crossover through ionomer membranes, hydrogen peroxide formation and movement, cyclic stresses and strains, recrystallized Pt particles, and transition metal ion contaminants are appeared to be major contributors to the degradation of polymer electrolyte membranes. Additionally, there is considerable experimental evidence indicating that chain scission reactions are occurring in fuel cell tests conducted under high temperature OCV testing. While chemical degradation of perfluorosulfonated ionomer membranes has been extensively studied and reported in literature[33, 78, 80-82, 84-93], there has been a little work on investigation of the interaction between the chemical and mechanical degradation.

Chemical reaction induced by mechanical stress— Investigations on the polymer degradation under mechanical stress have shown the possibility that mechanical force may

70

directly induce chemical reactions[130-132]. Aktah *et al.*[131] showed that mechanical

stress can cause not only a simple homolytic bond breakage, but also considerably more

complicated reactions in single molecules of poly(ethylene glycol) in water based on a

density functional theory (DFT) study. The author also revealed that the heterolytic breaking

of a stretched bond in solution is initiated by the attack of a solvent molecule. Wiita *et

al.*[132] studied the mechanical force effect on the kinetics of a chemical reaction of

thiol/disulfide exchange in an engineered protein using single-molecule force clamp

spectroscopy and concluded that the exchange reaction is a force-dependent chemical

reaction and mechanical force has something to do with the kinetics of any chemical reaction

that results in bond lengthening. By theoretical calculation, even the proton affinity of a

dimethyl ether turned out to be a function of an external mechanical force[133] and the

author mentioned that a energy profile of the reaction can be altered by a small force,

although they appear to be too small to cause a large geometrical change. Sohma[134]

reported the conversion of mechanoradicals in bimolecular reactions under mechanical stress.

Poly(methylmethacrylate) (PMMA) forms two mechanoradicals by main-chain scission, one

of which is converted into a new radical by a bimolecular reaction with another polymer

molecule. The author has interpreted this result in terms of the direct effect in

mechanochemistry, which he considers as a process that mechanical energy can induce

71

chemical reaction without going through any thermal path.   The field dealing with studies of chemical reactions by mechanical force has been coined as "Mechano-Chemistry".

Zhurkov *et al.*[117, 135] developed a kinetic theory for the fracture of solid polymers, which is based on an experimentally established relationship between the lifetime of the material, the tensile stress acting on the material, and the temperature.   The rate constant, K, of bond scission reaction under mechanical stress has been appeared to be governed the modified Arrhenius equation:

$$K = K_0 \exp[-(E_A - \alpha\sigma)/RT] \tag{4-1}$$

where, σ is the tensile stress, α is a coefficient with the dimension of m^3 / mol; determined experimentally, and their product is the mechanical work. Physically, this equation implies that the kinetics of bond scission is affected by the mechanical stress by reducing the activation energy of the reaction. The results of the experimental data indicated that the kinetics of mechanochemical bond scission of the polymer molecular chains can determine the strength and mechanical lifetime of polymers.

It has been reported that the degradation and decomposition of many types of polymer materials can be accelerated by mechanical force. Mechanically induced homolytic cleavage of the backbone bonds was the initiator leading to the formation of two free chain radicals as the primary degradation step of polymers: these radicals may recombine or react with oxygen

72

from air or attack other polymer molecules[101-103]. It is, therefore, hypothesized that the C-C bond in the TFE backbone or in the side chain in a PFSA membrane may be ruptured by mechanical stress and free chain radicals become the weak sites for subsequent attack by highly reactive oxygen radicals. In this research, the authors investigate the intrinsic interaction of mechanical stress and chemical decomposition rate of PFSA membrane using an experimental approach.

4.2 Experimental

Introduction to Gaseous H_2O_2 cell test.— Recently, a vapor phase hydrogen peroxide exposure test has been used as an *ex situ* accelerated membrane degradation test. The results indicated that not only are chain molecules unzipped, but that chain scission also takes place in the vapor phase peroxide test and degradation become more aggressive than that in the liquid phase Fenton's test[77, 78, 80]. In the test setup, an iron-impregnated membrane is exposed to the gaseous hydrogen peroxide to simulate the PEM fuel cell environment instead of the liquid in the typical Fenton's test; in a fuel cell, vapor phase hydrogen peroxide is expected to be present. The hydrogen peroxide gas is supplied by the inert carrier gas, nitrogen in this setup, and replenished to the chamber containing the membrane. The hydrogen peroxide gas reacts with the iron doped in the membrane to form the reactive

73

oxygen radicals and generates reaction products such as HF. These decomposed products are

collected in KOH solution for further analyses.

Cell fabrication/ modification/ test condition.— In order to verify the hypothesis of

the stress accelerated chemical degradation, this test setup is modified so that the mechanical

stress can be applied while the chemical reaction is proceeding as shown in Figure 4-1 and

the stress was applied to the membrane by hanging a dead weight.
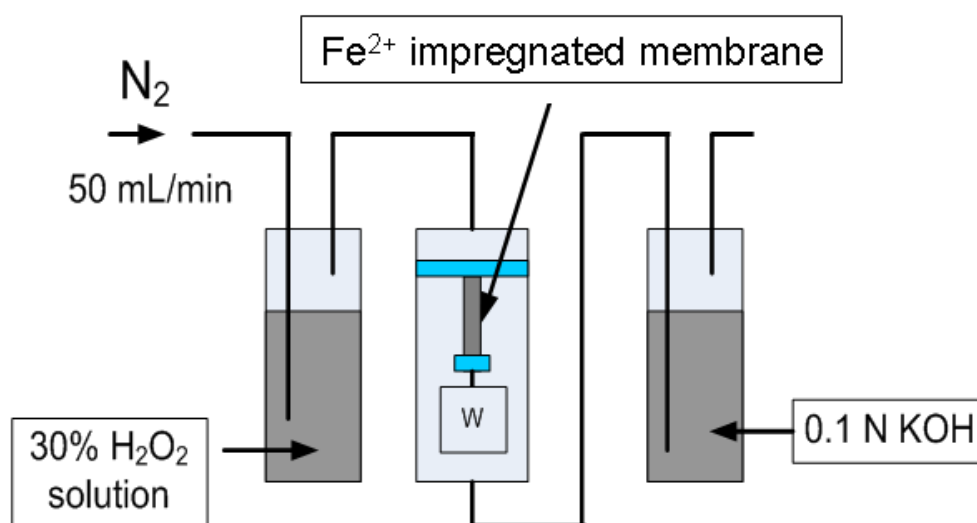
Figure 4-1 H_2O_2 gas cell for the *ex situ* accelerated degradation test of PFSA membrane with
and without applied mechanical stress

74

With this setup, the membrane is subjected to a controlled mechanical loading and chemical degradation simultaneously. Two identical gas cell setups were fabricated for parallel testing of two samples. The membrane chamber was made of polycarbonate (PC) tube to be compatible with the hydrogen peroxide [136] and the weight was applied by a high density polyethylene (HDPE) bottle with stainless steel balls sealed inside. The mechanical grip for holding the sample strip under stress is made of aluminum and the aluminum grip was coated with PTFE dispersion (TE3859, DuPont) [137]. The chamber was heated by heater cartridges inserted in a cylindrical aluminum tube fitted outside the polycarbonate tube chamber. The temperature of the hydrogen peroxide solution bottle was set to 60 ºC, and that of the membrane chamber to 80 ºC. Gas transfer lines from the H_2O_2 bottle to the membrane chamber were heated and thermally insulated to avoid condensation.

Sample preparation.— For the sample preparation, as-received NRE211 (Nafion 1 mil thickness, Equivalent weight (EW) = 1100 g/mol) membrane was cut into a size of 1.5 cm * 10 cm (sample type 1 in Figure 4-2(a)) and dried for 4 hours in the vacuum oven at 80 ºC. Then, the weight of the dried membrane was measured quickly. The membrane was doped with 25.3 mg Fe^{2+} per gram (dry base) of the membrane by soaking the sample in the iron sulfate solution overnight with continuous nitrogen purging. The amount of Fe^{2+} is expected to exchange all proton sites in the membranes (EW 1100). In order to further

confirm the chemical degradation induced by the mechanical stress, a membrane sample with

holes (sample type 2) was prepared to create a stress concentration around the hole, as shown

in Figure 4-2(b). This sample allows us to observe concentration of the end group at

locations with different stress levels around the hole. This sample was also doped with Fe^{2+}

with the same doping procedure as described above.

(a)
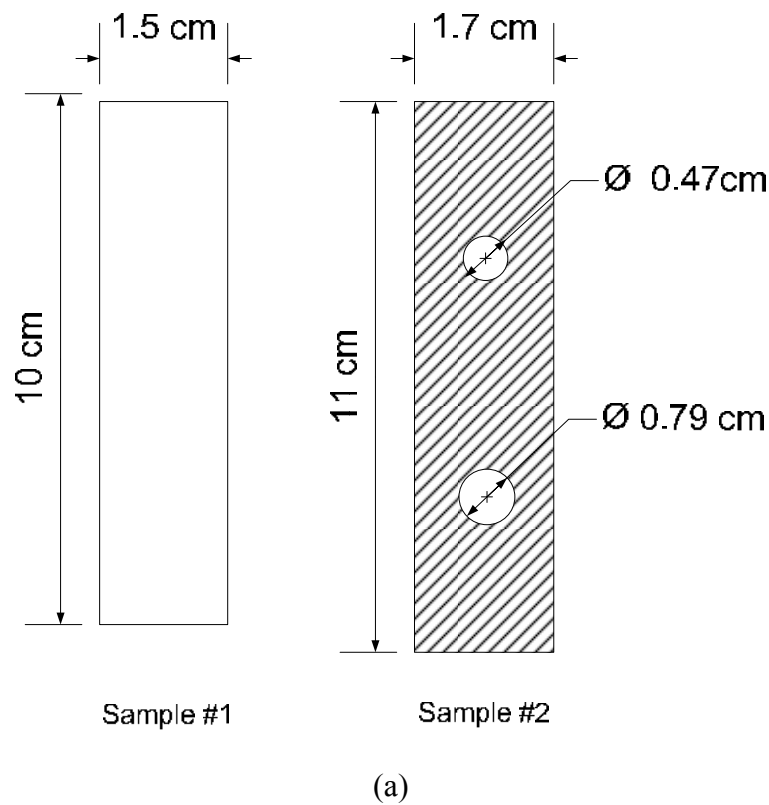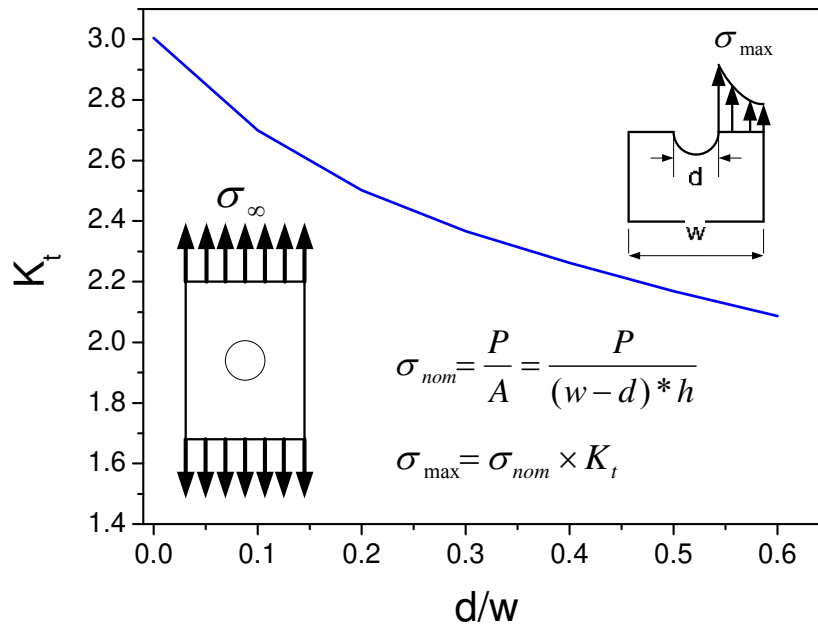
(b)

Figure 4-2 (a) Sample geometry for the H_2O_2 gas chamber test and (b) stress concentration factor around the hole in the sample

Applied stress level.— It is desirable to avoid the large deformation due to the creep response of the sample in this test. Therefore, a nominal stress of 5 MPa was applied to the sample type 1; the stress level is approximately equal to the yield stress of a membrane in the proton form at 80 ºC in 50% RH condition[57]. For sample type 2, an appropriate dead weight was applied so that the maximum stress (estimated at the stress concentration site) is below 5 MPa to avoid the large deformation around the hole due to the creep; permanent plastic deformation for all samples after the tests is less than 5% of the initial length of the

77

membrane sample. It was reported that stretching of Nafion does not lead to a significant change in membrane's crystalline morphology[138]; it was measured by WAXD, and also overhaul structure change by mechanical stress is negligible at small range of deformation, which is confirmed by SAXS and WAXS measurements[139]. These imply that we can eliminate possibilities of increase of chemical degradation rate due to gas permeability and/or pore size increase by the small deformation, potentially leading to higher peroxide exposure.

Stress concentration factors in Figure 4-2(b) based on linear elastic theory of solids were used to estimate the peak stress near the edge of the hole[140].   However, mechanical response of Nafion subjected to tensile force exhibits more likely viscoelastic-viscoplastic behavior and small compression force without geometrical constraints can cause material buckling easily. Therefore, the stress concentration that we estimated from the linear elastic theory does not represent actual stress level and distribution inside the membrane. Rather, the authors attempted to generate inhomogeneous stress distribution to see if different stress can generate different concentration of carboxylic end groups. The applied dead weight for sample type #2 was determined to be 54 g, which generates a nominal stress of 1.22 MPa in the sample, a maximum stress of 4 MPa around the small hole, and a maximum stress of 5 MPa around the large hole based on the linear elastic theory.

Post-analysis.—After the test, the fluoride ion (F⁻) concentration in the KOH solution was measured by a fluoride ion selective electrode (ISE, Orion 4 star), and the total fluoride emission (FE) from the sample was calculated based on the measured fluoride ion concentration in the trap. In preliminary testing, the fluoride concentration from the samples after 24hrs is too small to measure the concentration accurately by the ion electrode (less than 1 ppm), so we decided to measure the concentration of the solution after the adequate amount of time. The samples were also analyzed using FTIR spectroscopy for detection of the carboxylic end group concentration, which is believed to be a strong evidence of chain scission.   Tests were repeated several times for credibility of test results and proof of the hypothesis.   For the FTIR measurement, the membrane sample was converted back to proton form by soaking the sample in 0.5 M H_2SO_4 at 80 °C for at least 2 h and then converted to the potassium salt form as explained in the literature[141] to measure the C=O peak.   The attenuated total reflectance FTIR (ATR-FTIR) spectroscopy was employed for the analysis of the samples using the FTIR spectrometer (HORIBA, LabRam-IR) with ATR unit. The spectral range was from 600 to 4000 cm⁻¹. The measurement was performed at several points and the representative data is reported in this paper.

Mechanical tests were conducted to measure the decay of membrane mechanical strength and toughness after the test. The sample doped with Fe^{2+} after test #2 in Table 4-1

were cut into 4 strips (6 mm wide and 5cm long) and the strips were mounted at a grip of a mechanical testing machine built in house, consisting of a linear actuator, a load cell, data acquisition instruments, etc. The uniaxial stress-strain curves for the strips were obtained at 4.23 mm/s pulling rate at ambient conditions.

4.3 Results and discussions

Using two test chambers, comparative tests were conducted in pairs simultaneously; one sample was kept stress-free and mechanical stress was applied to the other sample. Two pairs (test #1, and #2) of comparative tests were conducted for sample type 1 and one pair (test #3) of comparative test was conducted for sample type 2. During the test, the hydrogen peroxide solution was refreshed every 3 or 4 days from the start of the test to avoid significant reduction of H2O2 concentration, with the exception of test #2; the authors didn't change the solution for the test #2 to see if the result can be affected by the solution change.

The FE results are tabulated in Table 4-1. Interestingly, the FE from the sample with stress after the 137 h test in test #1 is almost five times higher than that from the sample without stress. KOH solution was collected and FER was measured from the solution after the 137 h test, and a subsequent test for 166 h followed with the new KOH solution.

Table 4-1 The fluoride emission from the sample type 1 and 2 subjected to the H_2O_2 gas chamber test

Sample type 1		FE (μ mol/cm^2)		Time (hr)	Notes
		No stress	5 MPa		
Test #1	1st	1.445	7.087	137	
	2nd	3.245	6.91	166	
	Total	4.69	13.997	303	Sum of 1st and 2nd
Test #2		0.687	2.750	144	H_2O_2 solution not refreshed
Sample type 2		No stress	1.22 MPa (nominal)	Time (hr)	
Test #3		1.226	4.l23	144	

The second test (Test #2) was conducted to confirm the reproducibility and the load was applied to the new membrane sample in the chamber where the previous membrane sample in test #1 had been under no stress in order to get rid of any effects from differences in testing setup of the two identical cells. As can be seen in Table 4-1, even though the FE was lower than those in test #1 (we believed that it is because the solution was not refreshed), the FE from the sample with the stress is four times higher than that from the sample without stress.   This FE data from the test #2 was verified by ion chromatography to confirm that ISE measurement is correct.

These results were also confirmed by the FTIR spectra from two samples after Test #1 in Figure 4-3. The spectra from a control sample is superimposed in the Figure; the control sample was prepared by ion exchanging of as-received NRE 211 with potassium. The C=O stretch can be found at around 1690 cm-1[51, 73, 80] and the absorbance intensity from the sample with stress is clearly stronger than that from the sample without stress. This experimental evidence obviously indicates that the mechanical stress affects the chemical degradation of the membranes.
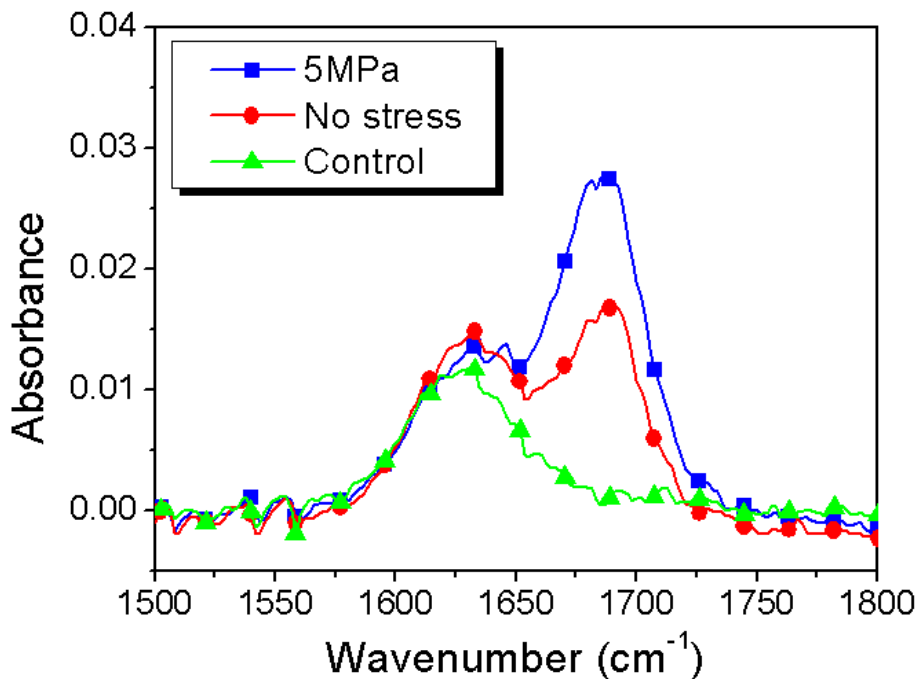
Figure 4-3 FTIR spectra of the membrane with and without stress after the test #1

82
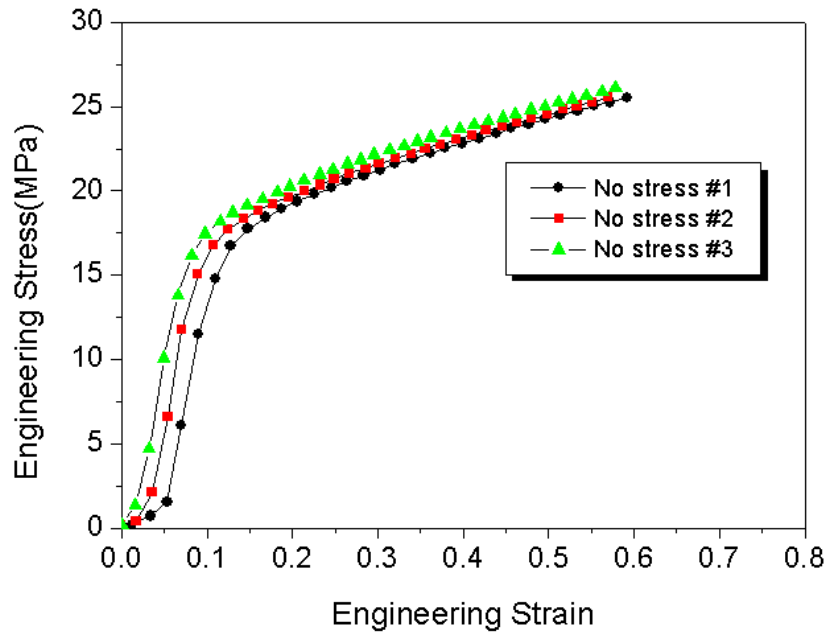
(a)
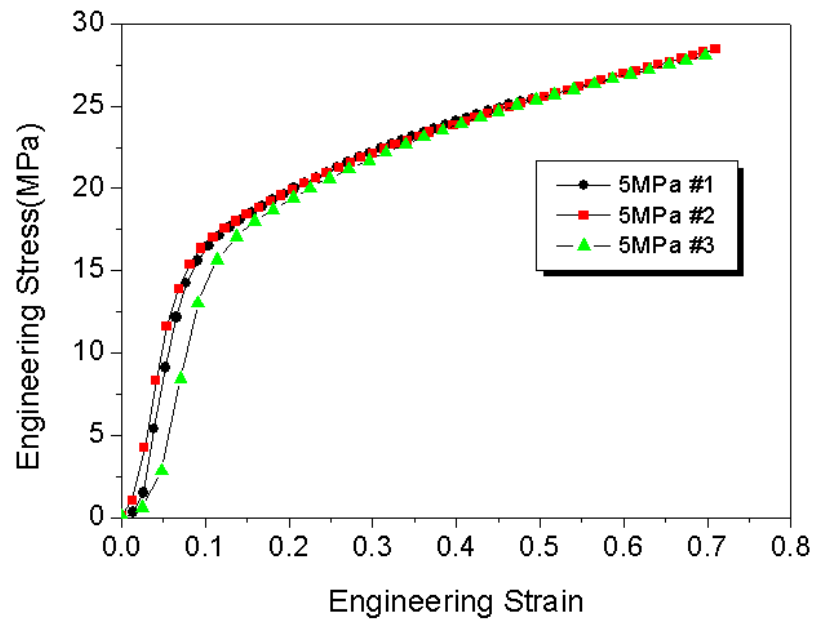
(b)

Figure 4-4   Mechanical behavior of the membrane doped with Fe^{2+} (a) aged without stress and (b) aged with stress

Figure 4-4 shows the stress-strain behavior of the Fe^{2+} doped membrane after test #2; the yield strength of the pure membrane doped with Fe^{2+} is slightly higher than that of the membrane with the proton form because of stronger ionic interactions, but the overall behavior is similar to each other. Although the two membranes had been put under degradation test for 144 h and the membrane with stress lost its fluoride material more than samples without applied stress, there are not significant differences in mechanical behavior between them. The membrane samples still show ductility to some extent after the aging test. This is quite different behavior from that of membranes after the accelerated degradation test in fuel cell such as the OCV hold test [50, 142]. This suggests that there must be factors other than membrane material losses and the morphology changes due to the radical attacks (crystallinity, entanglement density) that contribute to the brittle behavior of membrane after the accelerated degradation test in fuel cells.

To further confirm our hypothesis, two of sample type 2 (Figure 4-2(a)) were prepared and tested in the same way. The only difference in this test from the test before is that the sample geometry was designed to induce different stress levels inside the membrane in order to examine a variation of end group concentrations due to the different stress. Stress distribution from the Finite Element Modeling (FEM) of a Nafion membrane with a hole subjected to constant load is demonstrated in Figure 4-5. Absolute stress values from the

84

FEM results may not be real values that the membranes in our test were subjected to, but the results can predict at least the stress distribution over time and provide some insights to elucidate the test results from this experiment.
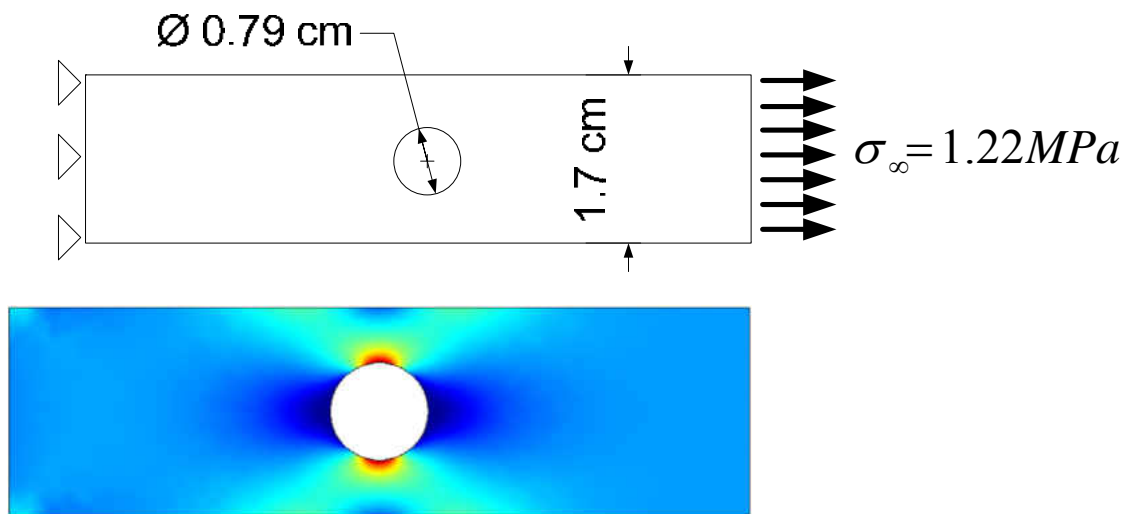
Figure 4-5 Stress distribution (Max = 4.67MPa,. Min = -0.27MPa) in the Nafion membrane with hole subjected to the tensile stress σ_∞

The FEM model was developed using visco-elasto-plastic constitutive model of Dual Network Fluoropolymer (DNF) proposed by Bergström and Boyce [143], based on the eight chain model of Aruda and Boyce[144] for rubber elastic materials. The parameters for the modeling were fitted to the uniaxial test results of the NRE 211 conducted at room temperature. The detail about the modeling is reported in the next chapter.

The points for the FTIR measurement and the spectra after the test are shown in Figure 4-6(a). It is quite interesting that not only is the intensity of the C=O peak in the membrane with stress higher than that in membrane without stress (Figure 4-6(c)), but the intensity of the C=O peak (Figure 4-6(b)) also varies with measurement points in even the same sample. This result is strong evidence that membrane experienced higher stress degraded more than that subjected to lower stress.
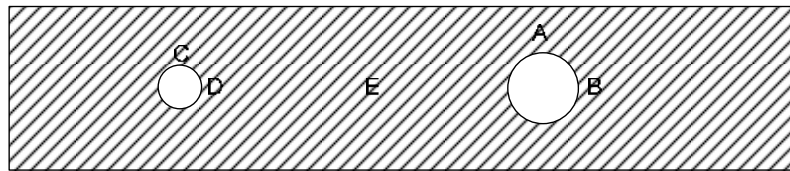
(a)
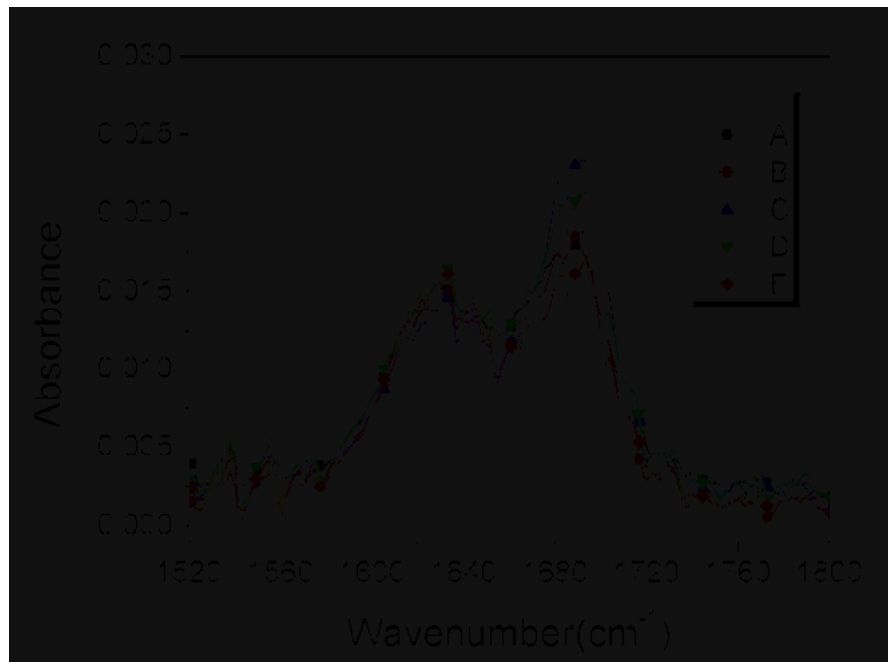
(b)
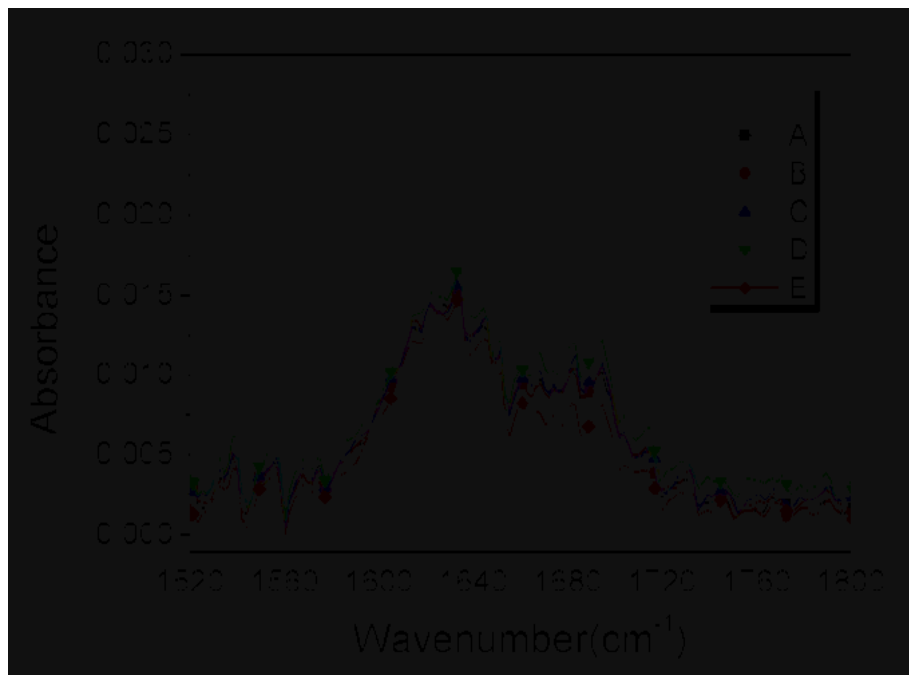
(c)

Figure 4-6 (a) Measurement points for FTIR, (b) FTIR spectra of the membrane with stress and (c) FTIR spectra of the membrane without stress after the test #3

PFSA membranes are believed to degrade via two main pathways: "main chain scission" and "unzipping"[77, 104, 128]. Based on the experimental results above, the membrane degradation by the two mechanisms can be definitely accelerated by the mechanical stress, even though the mechanical stress is not strong enough to break the chemical bonds by itself; 5 MPa is below the ultimate strength of the PFSA membrane. For the past few years, the reason why the membrane degradation in fuel cells at OCV and low humidity conditions is more severe than other cases has remained unclear. It is expected that the stress applied to the polymer would not be distributed uniformly in the polymer, which is

87

mostly due to the heterogeneous structure of the polymer; entanglement of polymer chains, boundary between crystalline and amorphous phase, etc., and would cause overstressed bonds [117, 135, 145-147]. Furthermore, stress distribution in the polymer such as polypropylene (PP), poly(ethylene terephthalate) (PETP), and nylon 6 was found to be extremely heterogeneous via infrared spectroscopy performed in the early 1970's [145, 147]. Assuming that this inhomogeneous stress distribution is the case in the ionomer membrane as well, it is anticipated that overstressed polymer backbones and/or side chains could be easily attacked by detrimental oxygen radicals formed by hydrogen and oxygen reactions on platinum bands and/or catalyst layers, because the activation energy of bond scission would be decreased by the form of mechanical energy. Also, in the author's recent paper about membrane degradation study using bi-layer membrane configuration after the OCV hold condition [142], it was revealed that the cathode side membranes, which is expected to have a Pt band inside, have shown brittle mechanical behavior in a uniaxial tension test, despite the membrane not losing its material significantly. This indicates that the Pt band might cause stress concentration around the Pt particles inside the membrane as well as radical formation, and the stress concentration accelerates the chemical degradation by the oxygen radicals due to the mechanical stress driving force. The stress around Pt particles in the membrane as well as high concentration of peroxide and radicals can generate the synergistic effect on the

degradation. This may be the reason why the localized membrane degradation is observed around the Pt band in the membrane and the liquid Fenton's test for membrane does not necessarily correlate with the degradation of membrane in fuel cells, where the peroxyl radicals can only attack the end group[34] and there is no stress effect. Further investigation is needed to identify exact role of Pt band on membrane degradation.

CHAPTER 5   A CONSTITUTIVE MODEL FOR IONOMER MEMBRANE

5.1 Introduction

Mechanical behavior of polymer electrolyte membrane (PEM) has been studied for a past decade over the wide range of temperature and relative humidity (RH) conditions by many research groups due to the significance of the membrane durability in fuel cell operation[57-59, 148-153]. Nafion®, one of the most popular proton exchange membranes, is employed in the PEM fuel cell and it is believed that membrane failure is the major fuel cell life determining factor, which, in turn, can have influence on the fuel cell durability[118, 142]. The existence of hydrophilic ionic clusters in hydrophobic perfluorinated ionomers allows the membrane to have not only a high proton conductivity, but also different mechanical property with respect to temperature and hydration level. At low temperature below 90°C, water acts as plasticizer softening the membrane and reducing load carrying capability. However, at elevated temperature above 90°C surprisingly, the opposite trend is observed; the more water a membrane absorbs, the stronger the membrane become [58, 59, 150]. This abnormal behavior was attributed to transitions in viscoelastic response of Nafion to microphase structural transitions driven by changes in temperature and water activity[150].

Mechanical stress prediction of ionomer membranes in various conditions in fuel cells is a key to understand mechanisms of the membrane degradation. The author recently

investigated the mechanical stress effect on chemical degradation of ionomer membrane and it was revealed that the mechanical energy directly accelerates the chemical reaction, which is chemical decomposition of the PEM by oxygen radical attacks on polymer chains in fuel cells[118]. The physical properties of polymeric systems are strongly affected by chain microstructure, i.e., isomerism, which is the organization of atoms along the chain as well as the chemical identity of monomer units [106]. Another important feature controlling the properties of polymeric materials is polymer architecture. The Nafion® membrane is a copolymer containing at least two monomers, i.e., a TFE back bone and perfluoro(4-methyl-3, 6-dioxa-7-octene-1-sulfonyl fluoride)[28]. A large amount of polymer research works continue to be directed towards the study of molecular mechanisms governing their structure-property relationships. Among them, the stress-strain response of polymers has been recognized for a long time as one of the most informative properties [107]. Figure 5-1 shows the typical stress-strain curve for a NRE 212 membrane. Macroscopic nature of the mechanical behavior for the Nafion® membrane under the tensile stress before rupture is characterized by an elastic response (Hook's law), followed by the strain hardening in the plastic deformation range after the yield point. These elastic and plastic deformation for the membrane is also time-dependent, i.e., viscoelastic and viscoplastic. Experimental data

presented in the Solasi's work [3] clearly demonstrated the complicated non-linear time, hydration level, and temperature dependent behavior of the ionomer membrane.
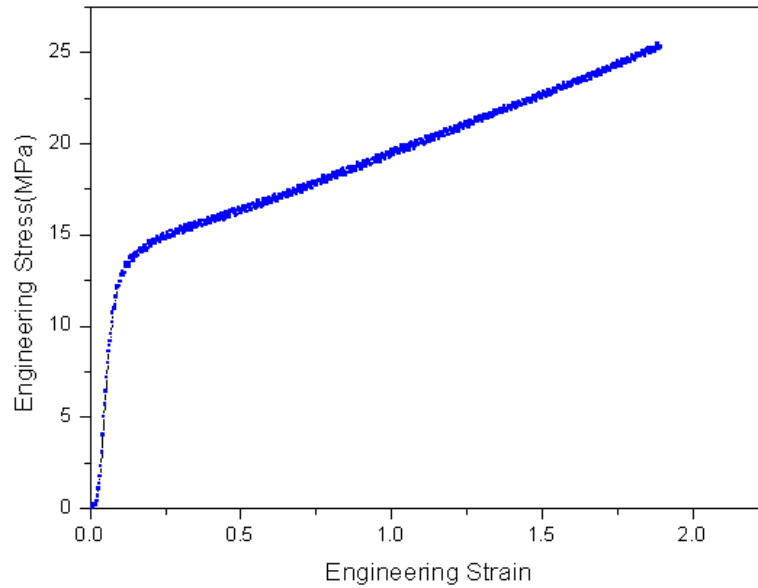
Figure 5-1 Tensile stress-strain curve of NRE 212 at room temperature with 4.23mm/s pulling rate

It is assumed that when an external load is applied to a polymer, the molecular bonds experience stress, and in order to relieve themselves as much as possible, the chain segments undergo internal rearrangements[107]; the way the polymer reacts to the external stress is dependent on the magnitude and rate of the applied stress, chain morphology, environmental factors such as humidity and temperature, etc. In literatures, it is believed that the Nafion® membrane consists of at least two phases[44]; an amorphous and crystalline phase, and the

crystallinity for 1,100 EW membrane is in a range between 5 and 20%[108]. Therefore, it is

expected that each component contributes to the deformation resistance differently.

Early attempt to interpret this macroscopic behavior and establish a relevant

continuum model based on the understanding of microstructure of polymers was achieved by

Haward *et al.*[109]; the polymer's mechanical response can be described by two parallel

processes, one of which is the initial non-linear elastic up to yield, interpreted as response

from the secondary and intermolecular interactions, with a combination of the entangled

network response in parallel from the interactions of primary intramolecular and physical

crosslink giving rise to an entropic contribution at large strains. As a continuous attempt for

describing the mechanical behavior of polymers, specifically, ionomer membrane, the author

propose a continuum model based on Bergström and Boyce's model[110] introduced at 1998.

5.2   Constitutive modeling of ionomer membrane
5.2.1   *Micro-mechanism of polymer deformation*

The constitutive model of ionomer membranes is needed for continuum mechanics

model to predict the distribution of the stress and strain in the fuel cell membrane. Typical

stress-strain behavior in Figure 5-1 can be qualitatively described by the initial Hookean

elasticity until the stress developed becomes sufficiently large to produce a plastic

deformation at the imposed rate and as the elongation proceeds, the stress increases with

strain referring to strain hardening with a reduction in the cross-section called "necking" during the finite plastic deformation, eventually leading to its final rupture; it is generally believed that the rupture of the polymer is induced by a defect formation and accumulation such as microcracks and crazing[121, 122]. In order to understand the mechanical behavior of the polymer membrane subjected to uniaxial stretching, many researchers have attempted to use existing linear elasticity[154], visco-plasticity[155], and elasto-plastic theory[49, 148, 151], but none of the models take into account the unique micromechanism of the polymer, such as a reptational plastic flow, chain entanglement, and entropic effect on deformation.

Figure 5-2 shows a hypothetical and hierarchical structure of the ionomer membrane consisting of the amorphous network, crystalline regions, and water clusters. It has been studied by many researchers that the molecular chain re-orients with the application of strain , thus producing strain hardening in polymers [144, 156]. The polymer macromolecular structure forming a network by means of physically entangled molecular chains are developed during deformation as a result of dissociation of secondary interactions with plastic strain[157]. Entanglements, a topological constraint, developed from the interpenetration of random-coil chains and are of great importance in determining rheological, dynamic, and fracture properties[158, 159].
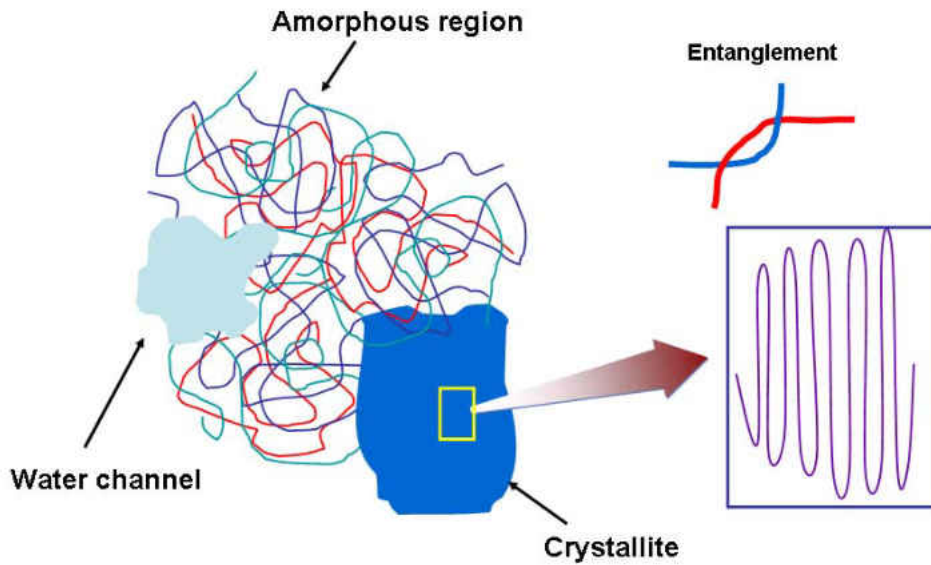
Figure 5-2   Schematic of hierarchy of ionomer membrane structure

Up to a certain temperature, chain mobility and morphological relaxation of intermolecular chain are expected to increase with temperature, which can be explained by reptational dynamics[56]. Also, it is reported that the mechanical stress increase the molecular mobility during plastic deformation[160].

Considering the morphology and microstructure of the ionomer membrane based on the various of researches in the papers [107, 161, 162], the mechanical deformation mechanisms is hypothesized as following:

1. The physical crosslinks formed by molecular entanglements, ionic interaction in sulfonic acid groups and intermolecular, secondary (Van der Waals) interactions in crystalline phase bear the low stresses in the elastic region of the stress-strain curve, leaving the major portion of bonds unaffected.

2. When the external load is increased beyond a certain level, ionic domains start to permanently deform, elongate and reorient[162]; as the stress develop, some chains in the amorphous and/or crystalline phase can overcome the secondary interactions and develop irreversible slippage and reorientation, yielding occurs. As stress/strain increases further, the permanently entangled chains (which can not slip out of physical entanglements) become taut and start locking up, resulting in strain hardening. As strain increases further, small crystallites can disintegrate [161].

Based on the hypothesized deformation micromechanism of the ionomer membrane, a 1-D rheological representation of the constitutive model is proposed, as shown in Figure 5-3. The original idea was initially developed by Bergström for the modeling of fluoropolymers[143], which is called Dual Network Fluoropolymer (DNF) model. Based on

the model, the mechanical behavior for ionomer membranes can be decomposed into two parts: a viscoplastic response, which is relevant to irreversible molecular chain slippage and a time-dependent viscoelastic response. The viscoelastic response can be separated into two different molecular responses combined in parallel: a first network (A) describes the nonlinear equilibrium of the viscoelastic response and a second network (B) represents the time-dependent response from the viscoelastic equilibrium state. The decomposition idea was introduced by Boyce[163] and Bergström[164, 165]. The Cauchy stress acting on the network A and B can be modeled by any of the classical models based on nonlinear hyperelasticity of elastomers. However, in this research, the Cauchy stress which is a function of the Cauchy Green deformation tensor is obtained from the Bergström and Boyce's model[110] for elastomers based on the eight-chain model of Arruda and Boyce [144]. Also, the plastic flow rule for the network B is motivated by reptational dynamics of a polymer[56, 166]. The DNF model, however, does not account for the hydration effect on mechanical properties of ionomer membranes originated from the water channel by sulfonic acid groups and therefore, for modeling of ionomer membranes, it is assumed that hydration effect can be incorporated implicitly into the empirical equation for the elastic modulus, which will be explained in the modeling section later.

$$T^{tot} = T^A + T^B$$
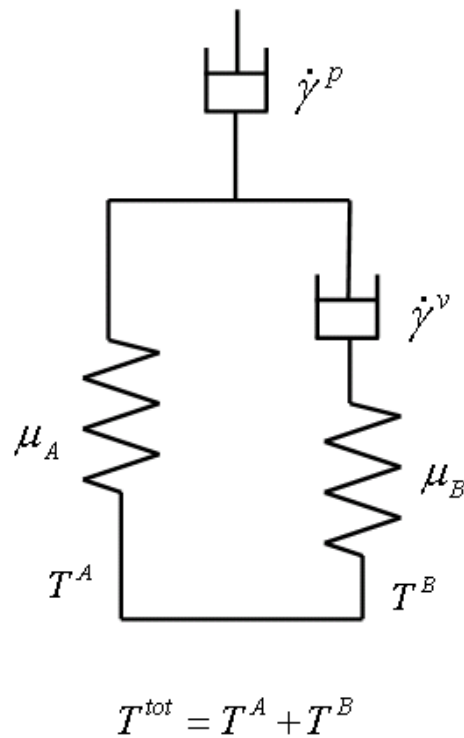
Figure 5-3 One dimensional rheological representation of the constitutive model for the

ionomer membrane

5.2.2 *Constitutive modeling*

The mathematical description of the constitutive model for ionomer membranes is

based on the breakdown of the overall deformation into the viscoelastic and viscoplatic

deformation which is referred to as the Kröner-Lee decomposition. For the analysis of the

large deformation of polymer, the concept of multiplicative decomposition of the deformation

gradient into elastic and plastic parts had been typically employed instead of an additive

decomposition [156, 163-165, 167-171]. The deformation gradient F is multiplicatively decomposed into viscoplastic and viscoelastic parts as shown below[143]:

$$F = F^{ve}F^{p} \tag{5-1}$$

,where F^{p} is the deformation purely due to the plastic flow representing irreversible chain motion and $F^{ve} = F^{A} = F^{B}$ is the remaining contribution to F associated with distortion and reorientation of crystallites and entanglement of polymer chains. The viscoelastic deformation gradient is further decomposed into elastic and viscous parts:

$$F^{ve} = F^{e}F^{v} \tag{5-2}$$

Here, F^{e} is the reversible (elastic) deformation gradient and F^{v} indicates the viscous deformation gradient. The spatial velocity gradient L is given by $L = \dot{F} \cdot F^{-1}$. By inserting $F = F^{ve}F^{p}$ into $L = \dot{F} \cdot F^{-1}$, the corresponding rate kinematics can be decomposed into viscoelastic and viscoplastic contributions:

$$\begin{aligned} L &= \dot{F} \cdot F^{-1} = (\dot{F}^{ve}F^{p} + F^{ve}\dot{F}^{p})(F^{ve}F^{p})^{-1} \\ &= \dot{F}^{ve}F^{p}F^{-p}F^{-ve} + F^{ve}\dot{F}^{p}F^{-p}F^{-ve} = L^{ve} + F^{ve}L^{p}F^{-ve} = L^{ve} + \widetilde{L}^{p} \end{aligned} \tag{5-3}$$

where $\widetilde{L}^{p} = \widetilde{D}^{p} + \widetilde{W}^{p}$. The rate of deformation, $\widetilde{D}^{p}$ and spin tensors, $\widetilde{W}^{p}$ are defined as the symmetric and skew-symmetric parts of $\widetilde{L}^{p}$. Likewise, the velocity gradient of viscoelastic parts can be decomposed into elastic and viscous components:

$L^{ve} = \dot{F}^{ve} \cdot F^{ve-1} = L^{e} + \widetilde{L}^{v}$, where $\widetilde{L}^{v} = \widetilde{D}^{v} + \widetilde{W}^{v}$. It should be noted that the intermediate configurations described by p and v are, in general, not uniquely

99

determined, since an arbitrary rigid rotation can be superimposed on it and leave it stress free[172] . The intermediate state can be determined uniquely in different ways and one convenient way is to prescribe $\widetilde{W}^v = 0$ and $\widetilde{W}^p = 0$, which means that the flow is irrotational[173]. In addition to that, plastic and viscous deformation are assumed to be incompressible, i.e., $\mathbf{det}(F^v) = 1$ and $\det(F^p) = 1$. In our study, the volumetric swelling and shrinkage behavior of the Nafion as function of the hydration level and temperature are not considered in the kinematics yet, and during the deformation, it is assumed that the hydration level and temperature are constant. Also, the deformation of Nafion over the whole strain range is assumed to be nearly incompressible, $\mathbf{det}(\mathbf{F}) \approx 1$ as well.

The Cauchy stress tensor for network A is described by the eight-chain representation[144, 164]:

$$T^A = f_{8ch}(F^{ve}) = \frac{\mu_A}{J^{ve}\overline{\lambda^{ve}}} \cdot \frac{\mathcal{L}^{-1}(\overline{\lambda^{ve}}/\lambda^{lock})}{\mathcal{L}^{-1}(1/\lambda^{lock})} \mathbf{dev}[\mathbf{B}^{ve*}] + \kappa[J^{ve} - 1]\mathbf{1}$$

(5- 4)

where $J^{ve} = \det[\mathbf{F}^{ve}]$, μ_A is a temperature and hydration level dependent initial shear modulus, λ^{lock} is the chain locking stretch, $B^{ve*} = (J^{ve})^{-2/3}F^{ve}(F^{ve})^{T}$ is the left

Cauchy Green tensor, $\overline{\lambda^{ve}} = \sqrt{tr(\mathrm{B}^{ve*})/3}$ is the effective chain stretch based on the eight-chain assumption, $\mathcal{L}^{-1}(x)$ is the inverse Langevin function, where $\mathcal{L}(x) = \coth(x) - 1/x$, and κ is the bulk modulus. To obtain the inverse, a curve fit of the inverse Langevin function is used for all x [166]:

$$\mathcal{L}^{-1}(x) \approx \begin{cases} 1.31446\tan(1.58986x) + 0.91209x, & if\ |x| < 0.84136 \\ 1/(sign(x) - x) & if\ 0.84136 \le |x| \le 1 \end{cases} \quad (5\text{-}5)$$

The Cauchy stress tensor for network B can be calculated from the eight-chain representation used for network A and computed by multiplication of the eight-chain expression on the elastic deformation gradient $\mathbf{F}^e$ with a scalar factor s_B which can be considered as a specific material parameter.

$$T^B = s_B \cdot f_{8ch}(F^e) = s_B \cdot \left(\frac{\mu_B}{J^e\,\overline{\lambda^e}} \cdot \frac{\mathcal{L}^{-1}(\overline{\lambda^e}/\lambda^{lock})}{\mathcal{L}^{-1}(1/\lambda^{lock})} \mathrm{dev}[\mathrm{B}^{e*}] + \kappa[J^e - 1]\mathbf{1} \right)$$

$$(5\text{-}6)$$

Then, the total Cauchy stress is the sum of the two resultants, namely $T = T^A + T^B$. The First Piolar Kirhoff stress, P which relates forces in the present configuration with areas in the reference configuration can be calculated from conversion between two stress, $P = J \cdot \mathbf{T} \cdot \mathbf{F}^{-\mathbf{T}} = J \cdot (T^A + T^B) \cdot \mathbf{F}^{-\mathbf{T}}$. In order to incorporate the hydration and temperature dependent mechanical property such as μ_A and μ_B for ionomer membranes, empirical relationship of elastic modulus as a function of membrane water content, λ_m and

temperature, θ ($^{\circ}C$) was used. It should be noted that the bulk modulus κ is the function of the water content and temperature as well, but due to the difficulty in obtaining the value experimentally, it is assumed to be a constant and its magnitude was taken as a reasonable value in the analysis. Also, the simulated stress is not significantly varied by the bulk modulus because of incompressibility assumption. Earlier attempt for the empirical relation of the elastic modulus was already made by Hsu et al., [174] but for our research, the uniaxial testing data for N111 membrane was collected by Zou [175] under the well controlled environmental chamber and these data sets were used for fitting the exponential type function as shown below [175]:

$$E(\lambda,\theta) = \exp\{(A_1 \cdot \theta + B_1) \cdot \lambda_m + (A_2 \cdot \theta + B_2)\} \tag{5-7}$$

where $\lambda_m = 0.043 + 17.81a_T - 39.85a_T{}^2 + 36.0a_T{}^3 \quad for \ 0 < a_T \le 1$ [176] and a_T is the water activity (RH) defined by $a_T = p_w / p_{sat}(\theta)$, where p_w is water vapor pressure and p_{sat} is saturation water vapor pressure at the temperature. From the elastic modulus equation, the initial shear modulus for network A and B can be described by

$$\mu_B = s_{0B} \cdot E(\lambda,\theta) = s_{0B} \cdot \exp\{(A_1 \cdot \theta + B_1) \cdot \lambda_m + (A_2 \cdot \theta + B_2)\} \tag{5-8}$$

$$\mu_A = s_{0A} \cdot \mu_B \tag{5-9}$$

where s_{0A} and s_{0B} are material parameters and A_1, B_1, A_2, and B_2 are fitting constants listed in Table 5-1.

Table 5-1 Fitting constants for elastic modulus equation

A_1	B_1	A_2	B_2
0.000645	-0.058673	-0.014673	10.534189

The rate of viscoplastic flow of network B can be described by $\widetilde{D}^v = \dot{\gamma}^v N^v$. The tensor N^v is the direction tensor of the driving deviatoric stresses of the relaxed configuration [143] and the terms $\dot{\gamma}^v$ indicates the flow rates, given by the reptation-inspired equation[164]:

$$\dot{\gamma}^v = \dot{\gamma}_0 [\bar{\lambda}^v - 1]^c \cdot \left(\frac{\tau^e}{\tau_{base} + \beta p^e} \right)^m \cdot \left(\frac{\theta}{\theta_{base}} \right)^n \qquad (5\text{-}10)$$

where, $\tau^e = \left\| \mathbf{T^{e'}} \right\|_F \equiv (tr[\mathbf{T^{e'}} \mathbf{T^{e'}}])^{1/2}$ is the Frobenius norm of $\mathbf{T^{e'}} = \mathbf{dev}[\mathbf{T^e}]$, the direction of the driving stress is described by $\mathbf{N}^v = \mathbf{T}^{e'} / \tau^e$, $\overline{\lambda^v} = \sqrt{tr(\mathbf{B}^{v*})/3}$ is an effective viscous chain stretch, $\mathbf{B}^{v*} = (J^v)^{-2/3} \mathbf{F}^v (\mathbf{F}^v)^{\mathbf{T}}$ is the left Cauchy Green deformation tensor, $p^e = -(T_{11}^e + T_{22}^e + T_{33}^e)/3$ is the hydrostatic pressure, and $C \in [-1,0], m > 0, n, \beta, \dot{\gamma}_0, \theta_{base}$ and τ_{base} .are material parameters. As pointed out by Bergström, the term $[\bar{\lambda}^v - 1]^c$ captures a strain dependence of the effective viscosity and this might cause the term to grow numerically very large if the effective stretch $\overline{\lambda}^v$ is unity or close to unity in both the unloaded state and when the applied strain switches between tension

103

and compression. One way to resolve this problem is to introduce a parameter $\varepsilon \approx 0.01$ to avoid the singularity and the equation (5-10) can be modified as follows:

$$\dot{\gamma}^v = \dot{\gamma}_0 [\overline{\lambda}^v - 1 + \varepsilon]^c \cdot \left(\frac{\tau^e}{\tau_{base} + \beta p^e}\right)^m \cdot \left(\frac{\theta}{\theta_{base}}\right)^n$$

(5-11)

Another way to eliminate the numerical difficulty is to use certain differentiable smooth ramp function[177] which is adapted for our research as shown in Figure 4 and replace $[\overline{\lambda}^v - 1]$ by $R(\overline{\lambda}^v - 1)$

where,

$$R(\alpha) = 2.8853 \cdot \varepsilon \cdot \left(0.3466 + 0.1733 \frac{\alpha}{\varepsilon} - 0.5 \cdot \ln\left\{ \frac{1}{\cosh\left[0.3446 \cdot \frac{\alpha}{\varepsilon} \right]} \right\} \right)$$

(5-12)

satisfying

$$\lim_{\alpha \to -\infty} \left(\frac{\mathbf{d}R(\alpha)}{\mathbf{d}\alpha} \right) = 0, \quad R(0) = \varepsilon, \quad \lim_{\alpha \to +\infty} \left(\frac{\mathbf{d}R(\alpha)}{\mathbf{d}\alpha} \right) = 1.$$

104
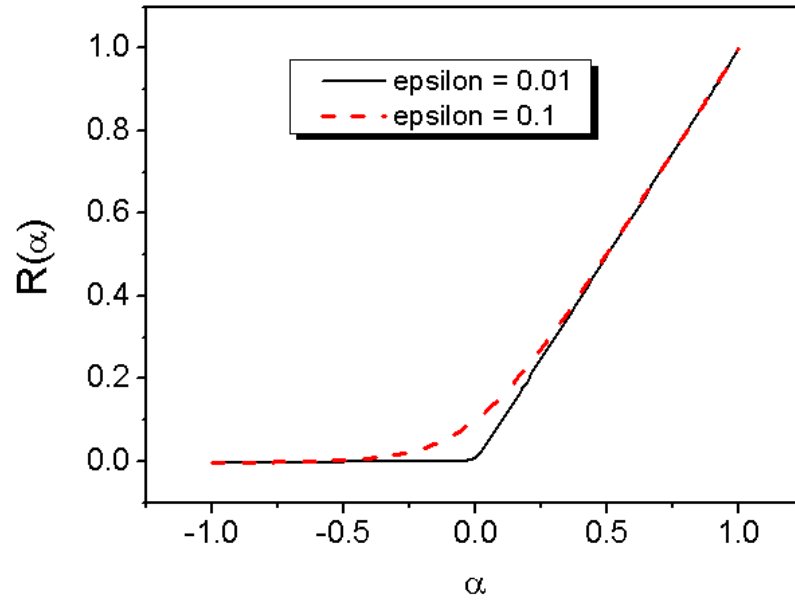
Figure 5-4 Smooth ramp function

As a result, the velocity gradient of the viscous flow can be expressed as:

$$\widetilde{\mathbf{L}}^v = \mathbf{F}^\mathbf{e}\mathbf{L}^\mathbf{v}\mathbf{F}^{\mathbf{e}^{-1}} = \widetilde{\mathbf{D}}^v = \dot{\gamma}^v\,\frac{\mathbf{T}^{\mathbf{e}'}}{\tau^\mathbf{e}}$$

$$\therefore\,\dot{\mathbf{F}}^v = \mathbf{F}^{\mathbf{e}^{-1}}\left(\dot{\gamma}^v\,\frac{\mathbf{T}^{\mathbf{e}'}}{\tau^\mathbf{e}}\right)\mathbf{F}^\mathbf{e}\mathbf{F}^\mathbf{v}$$

(5-13)

The rate of plastic flow is described by a phenomenological equation[143]:

$$\dot{\gamma}^p = \begin{cases} a\,b(\varepsilon - \varepsilon_0)^{b-1}\dot{\varepsilon} & if\ \tau > \sigma_0 \\ 0 & otherwise, \end{cases}$$

(5-14)

where, $a > 0, b > 0$ and $\sigma_0 > 0$ are material parameters, $\tau = \left\|\mathrm{dev}[\mathrm{T}]\right\|_F$ is the

Frobenius norm of the deviatoric part of the Cauchy stress T, and ε_0 is the effective strain

when τ is equal to σ_0; the effective strain can be calculated from $\varepsilon = \left\|\mathrm{E}_{\ln}\right\|_F$,

105

where $E_{ln} = ln[V]$ and V is the left stretch tensor, and $\dot{\varepsilon}$ is the effective strain rate. For our research, ε_0 is considered as a constant and the engineering strain rate was used for $\dot{\varepsilon}$ for the simplicity since the plastic flow rate can be controlled by choosing the appropriate parameters, a and b. As can be noticed in the equation (14), the plastic flow rate is a function of the strain rate and magnitude of current strain.

In summary, the velocity gradient of the plastic flow can be expressed as:

$$\widetilde{L}^p = F^{ve}L^pF^{ve^{-1}} = \widetilde{D}^p = \dot{\gamma}^p \frac{dev[T]}{\tau}$$

$$\therefore \dot{F}^p = F^{ve^{-1}}\left(\dot{\gamma}^p \frac{dev[T]}{\tau}\right)F^{ve}F^p \qquad (5\text{-}15)$$

5.3 Experimental

The mechanical data used in this work originally obtained by Solasi [3] and Zou [175], as part of their graduate research work at Connecticut Global Fuel Cell Center of University of Connecticut. A brief introduction of the mechanical testing procedure is given below. Mechanical testing of Nafion membrane was performed on MTS Tytron[TM] 250, a horizontal material testing frame designed especially for membrane testing. Due to the strongly dependence of mechanical properties for ionomer membrane on the water content and temperature, all the uniaxial tension tests were conducted under well controlled environmental conditions of humidity and temperature. An environment chamber with RH

and T was built to fit the horizontal rail of Tytron machine load frame and the RH control was achieved by mixing dry and saturated gas stream. Steady state RH values were taken from a chilled mirror dew point sensor (EdgeTech Dew Prime II) continuously sampling the RH of the gas existing the chamber and temperature was measured by a platinum RTD probe installed closely to the membrane sample inside the chamber. The membrane samples, N111, a commercially available from DuPont, were cut into rectangular shape with about 50mm length and 6.5mm wide. The specimens were placed in the chamber and allowed to stay for at least 1hr in order to achieve equilibrium state before the tests. Mechanical testing data at three different condition, which were 25ºC and 80%RH, 25ºC and 50%RH, and 65ºC and 75%RH were used for comparison with FEM results. The stress-strain curve for the samples is obtained by applying a tensile force at a uniform strain rate of 0.0132/s.
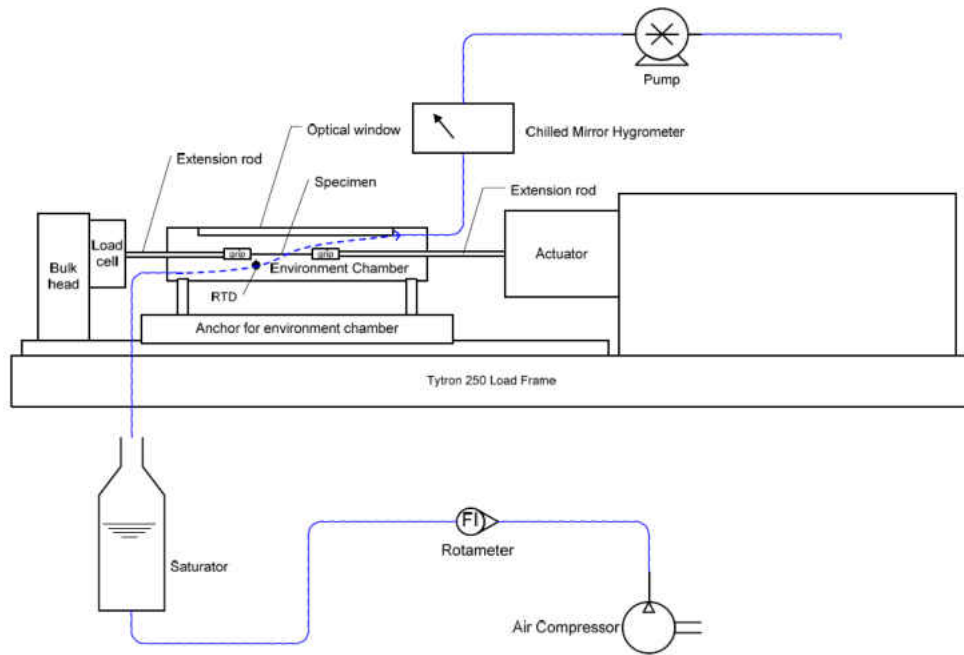
Figure 5-5 Schematic diagram of membrane mechanical testing setup

To study the material properties in liquid water hydrated state, a water bath tray together with a U-type pulling rod were designed to conduct uniaxial tension tests with the immersed membrane samples in water.

The stress-strain data were calculated from load and displacement data for the vapor-equilibrated membrane using original cross-sectional area and gauge length of the samples and linear expansion rate of 15% from the Dupont's product information[178] were applied to compensate the volumetric expansion in the calculation of the area for the water-equilibrated membrane at 80°C

108

5.4 Finite element simulation

Mathematical modeling of the mechanical behavior using a finite element method could help us understand the physical mechanisms of material deformation under various conditions. In our model, the material parameters in shear modulus, and viscous and plastic flow rules need to be calibrated and therefore we developed a one-dimensional model to facilitate the calibration process [179]. This model can allow us to determine approximate material parameters that can be used in a FEM software and provides us with a broad insight of an overhaul mechanical behavior with respect to variations of each parameter. For this simple model, the viscoplastic term was ignored and only viscoelastic deformation was considered. Newton method was employed to update time dependent viscous deformation gradient. Experiment data were obtained from as-received NRE 212 at ambient condition with 10 in/ min pulling rate and comparison of simulation result and experiment data is shown in Figure 5-6. The fit was implemented by adjusting material parameters iteratively to get the best approximation of loading response. Clearly, it appears that one-dimensional approximation can predict loading response accurately. From this result, the authors can determine which parameter dominates on the shape of stress-strain response and decide an approximate range of parameter values at various conditions.

www.manaraa.com
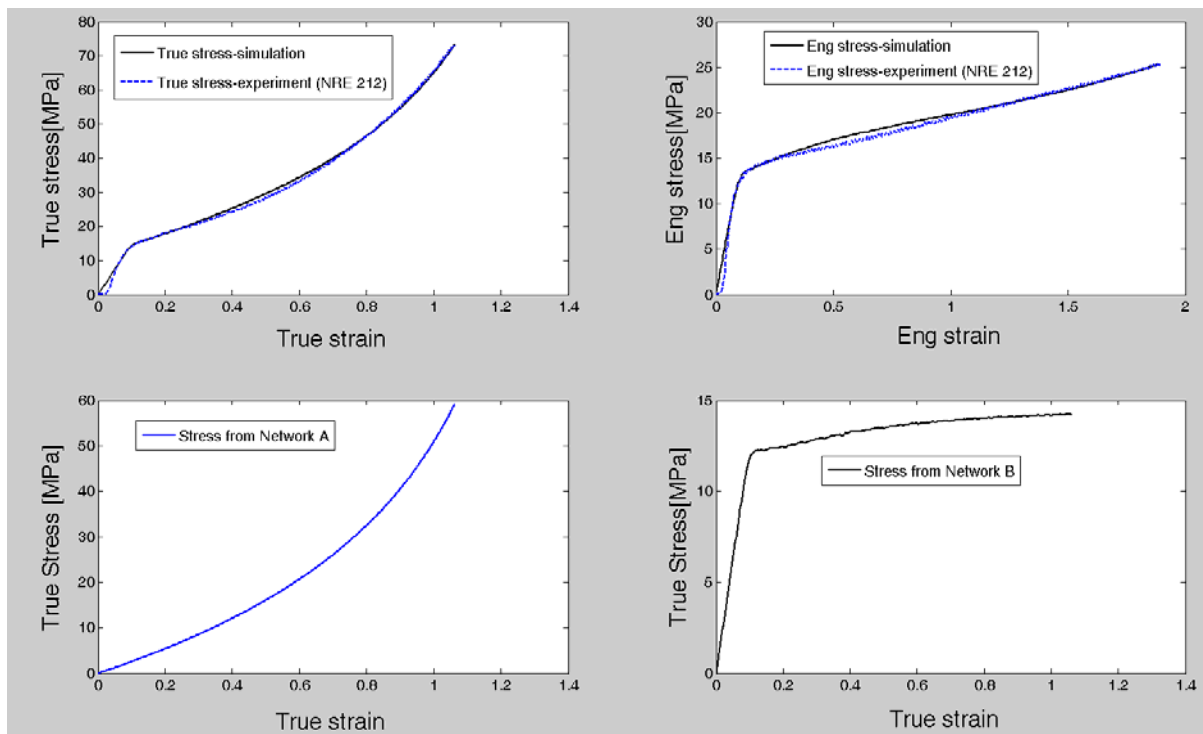
Figure 5-6   A one dimensional viscoelastic constitutive model of Nafion materials

With the results from one dimensional approximation in mind, two dimensional constitutive model for ionomer membrane was implemented into Comsol Mutiphysics 3.5 software package. The structure mechanics and PDE modules were utilized for the simulation of time dependent behavior of the membrane in an application module of plane stress. The PDE module was used for the integration of the time evolution equation for viscous flow and plastic flow. At every time step, the viscous and plastic deformation gradient were calculated and used for computing the Cauchy stress components on the network A and B. When the material response is nearly incompressible, the pure displacement formulation behave poorly.

110

To overcome this problem a mixed U-P formulation provided in the software was used for calculation of independent variable, pressure p .

5.5   Results and discussions

Figure 5-7 (a) shows the engineering stress-strain curves of as received N111 membrane at three different conditions. Plastic deformation sets in at a strain around 0.1 and the material hardens as the strain further increase. If the strain is large, the elastic component of strain is considered negligible compared to the plastic deformation. It seems that the yield strength and elastic modulus are decreasing with increasing temperature, and temperature appears to play a significant role on mechanical properties such as yield strength, and ultimate stress as already pointed out by many researchers[49, 58, 59, 155]. The secondary slope, strain hardening seems to change slightly with respect to temperature and humidity, but their effect appears to be less significant comparing to the elastic modulus and yield strength.

The stress-strain curves from FEM simulation (Figure 5-7 b~d) shows fairly good qualitative agreement with experimental behavior of vapor-equilibrated ionomer membranes. The FEM predicts temperature and hydration dependent mechanical behavior of membrane and overall shape of the strain hardening behavior conforms to the experiment results. The proposed constitutive model can accurately describe the mechanical behavior of the vapor

111

equilibrated membrane. Material parameters and other constants used at the simulation are tabulated in Table 5-2 and Table 5-3.

From the rheological representation in Figure 5-3, the true stress components can be dissociated into the stress acting on network A and network B. As mentioned earlier, the true stress from network A captures the equilibrium response of the material and network B represents time dependent separation from viscoelastic equilibrium state. As generally accepted, physical resistances which are related with intermolecular and intramolecular interactions controlling the activation energy barrier must be surmounted to yield the material and to deform it up to large plastic strain[180]. This micro-structure induces the rate and temperature effects governing the material behavior.

112
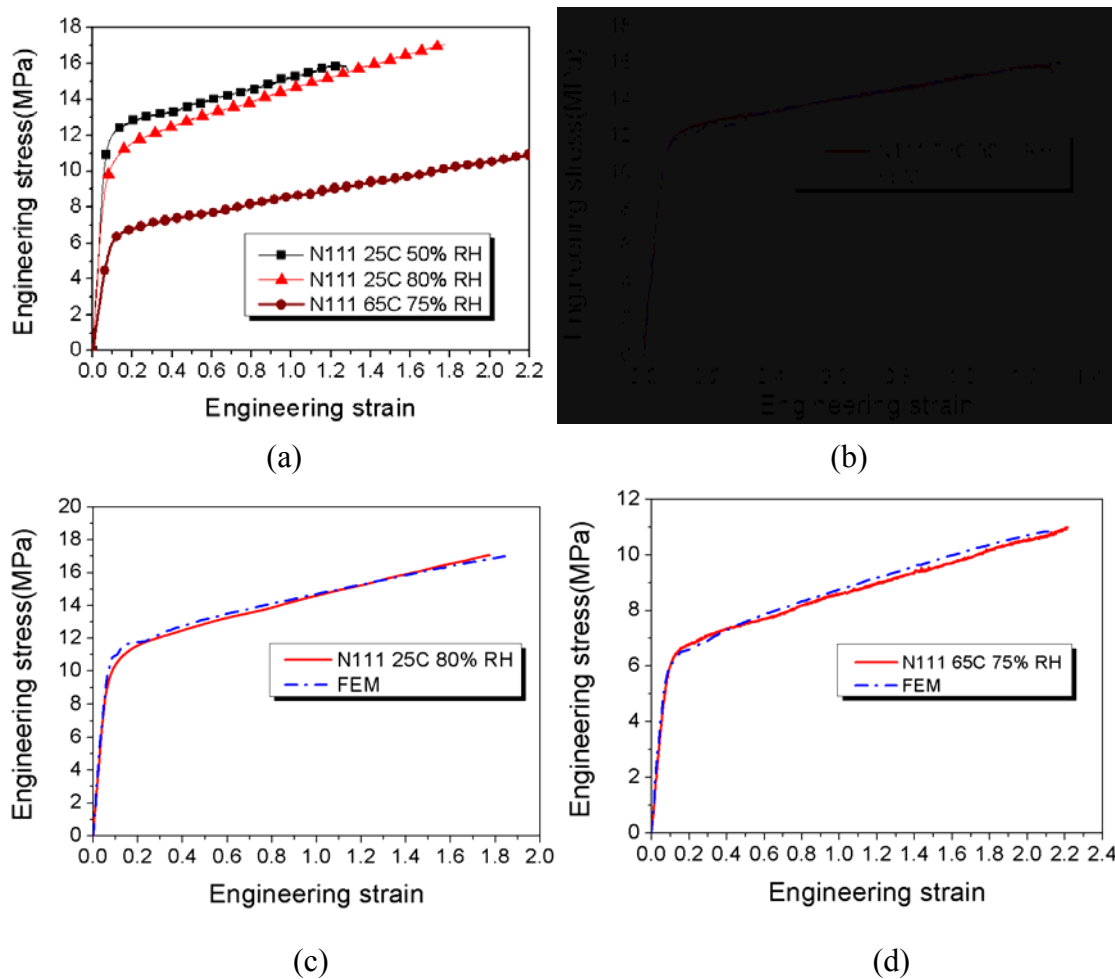
Figure 5-7 (a) Experiment results of stress-strain curves of Nafion N111 membrane under the various test conditions , (b) FEM simulation results of N111 at 25°C and 50%RH, (c) 25°C and 80%RH, and (d) 65°C and 75%RH

Figure 5-8 and Figure 5-9 show the each true stress component from the stress-strain curve calculated from FEM. At low strain, the stress is dominantly exerted by the intermolecular interactions (network B) in crystallites, amorphous phase, and ionic domain.

113

However, at high strains, network B can no longer bear the stress due to the molecular relaxation and/or crystallite disintegration, and the rubber-like network A are superior resulting in the strain hardening behavior, which can be explained by deformation, reorientation, and tout of entangled chain molecules. In Figure 5-8, it is noticed that at the same temperature and different RH(25°C 50% and 80%), the mechanical behavior of the rubber-like network A does not show discernable difference, but the whole curve of network B is shifted downward as the RH increase, which indicates that the water vapor weakens the network A component more than network B. This, in turn, can imply that the water vapor interferes with intermolecular network such as secondary interaction of PTFE back bone and strong ionic interaction in the hydrophilic domain, and deteriorates their interactions[181]. However, in Figure 5-9, the temperature appears to influences critically on both mechanical behavior of network A and B at a given RH condition; it reduces load carrying capability of membranes by softening intermolecular interactions and enhancing the chain mobility in the material. There has been recent attempt to interpret the mechanical behavior by microstructure transition[150, 153] due to the temperature and water activity, and it is reported that the combined effects of temperature and water alter the structure of the hydrophilic domains changing the number, strength and flexibility of cross-links between domains. The attractive interactions between sulfonic acid groups are likely to aggregate and

114

form cross-links that stiffen membrane at the low temperature. However, increase of the temperature causes the sulfonic acid groups to become randomly dispersed and break the cross-links. Our FEM results show the consistency in mechanical behavior with theoretical hypothesis.
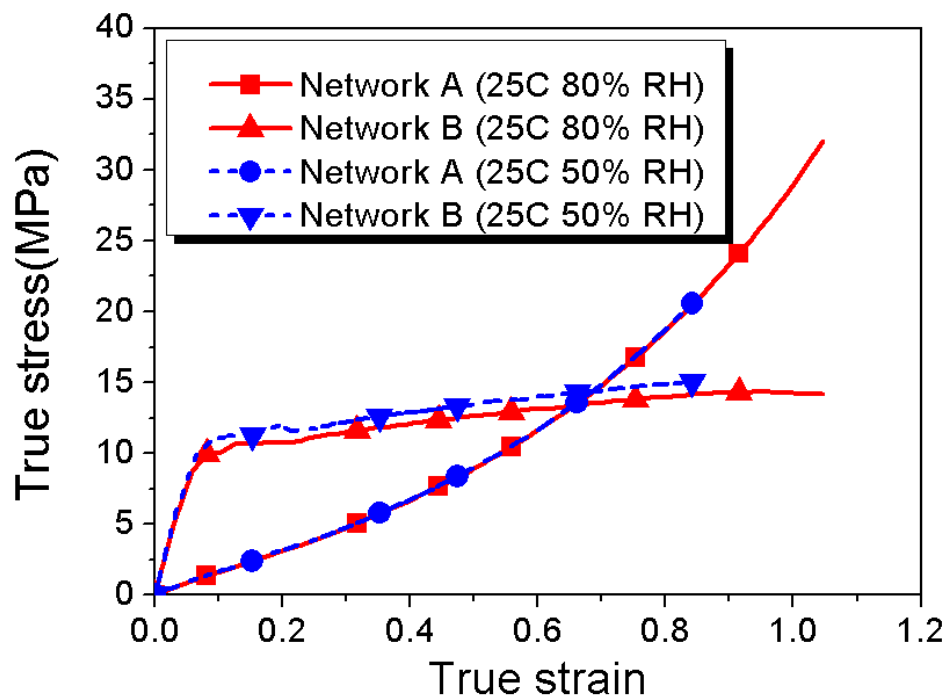
Figure 5-8 Comparison of contribution of each stress components for viscoelastic network A and B from FEM simulation results for N111 at 25°C, 50 %and 80% RH
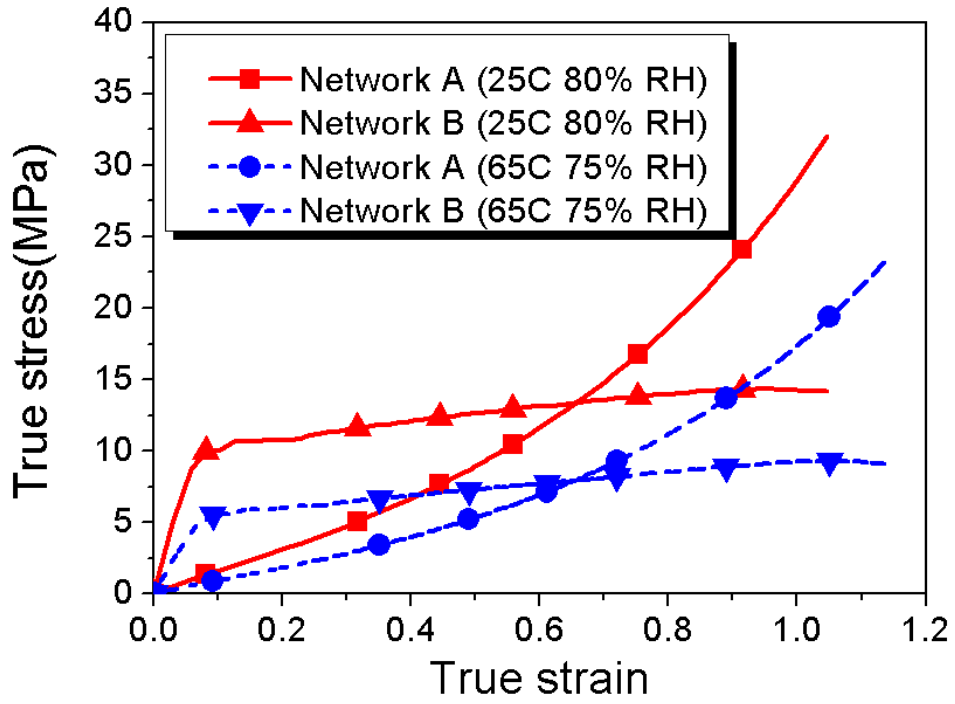
Figure 5-9 Contribution of each stress components of viscoelastic network A and B from

FEM simulation results for N111 at 25°C , 80%RH and 65°C, 75% RH

Table 5-2 Material parameters for FEM simulation of vapor-equilibrated membranes

C	-0.5
m	6
n	4.5
β	0.6
$\dot{\gamma}_0$	1
a	0.01
b	0.78
ε_0	0.01
σ_0	5 MPa
s_B	8
$\dot{\varepsilon}$	0.0132
θ_{base}	100
κ	97MPa
λ_{lock}	6

Table 5-3 Material parameters adjusted for FEM simulation of vapor-equilibrated membranes

	25°C, 50% RH	25°C, 80% RH	65°C, 75% RH
τ_{base}	$\mu_B * 1.42$	$\mu_B * 1.42$	$\mu_B * 3$
s_{0A}	0.75	0.8	1
s_{0B}	0.0256	0.0384	0.033

To evaluate the effectiveness of the proposed constitutive model, it was applied to fit stress-strain behavior of water-equilibrated Nafion samples at 80 ºC. The stress-strain curves were obtained from the uniaxial tests at strain rates of 0.3/s and 0.0045/s. The elastic modulus of water-equilibrated Nafion, E, was determined from the linear curve fit to the experimental results measured from the uniaxial tension tests. The material parameters are listed in

Table 5-4 and Table 5-5, and the results of the stress-strain curves are plotted in Figure 5-10. The simulated stress versus strain results show that the model can predict the rate dependence of the mechanical behavior as expected. The true stress components of network A and B at the two different strain rate are plotted in Figure 5-11, showing that the fast strain rate stiffens the time-dependent network A and B and increase the stress at the same strain.
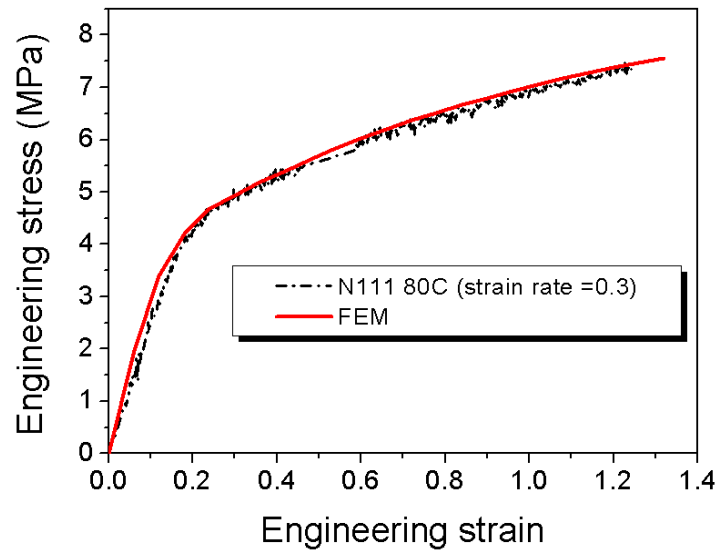
(a)
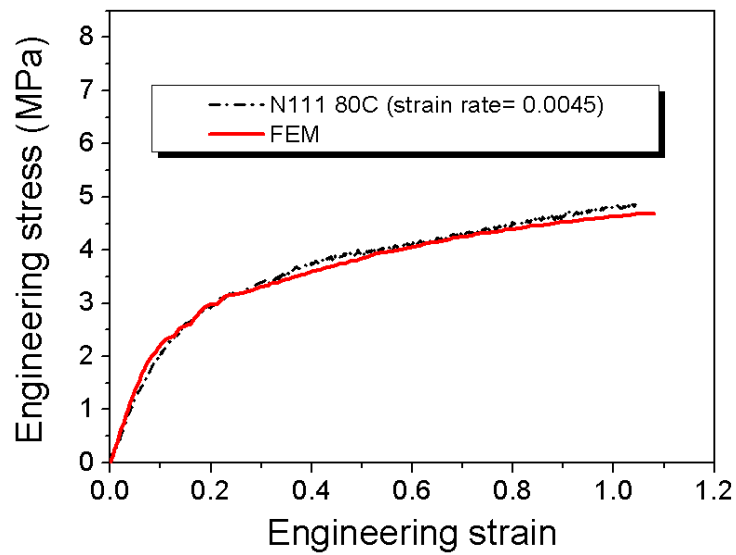
(b)

Figure 5-10   Comparison the experimental data from unaxial tension test with FEM results

(a) at the strain rate 0.3/s and (b) the strain rate 0.0045/s under the water at 80 ℃
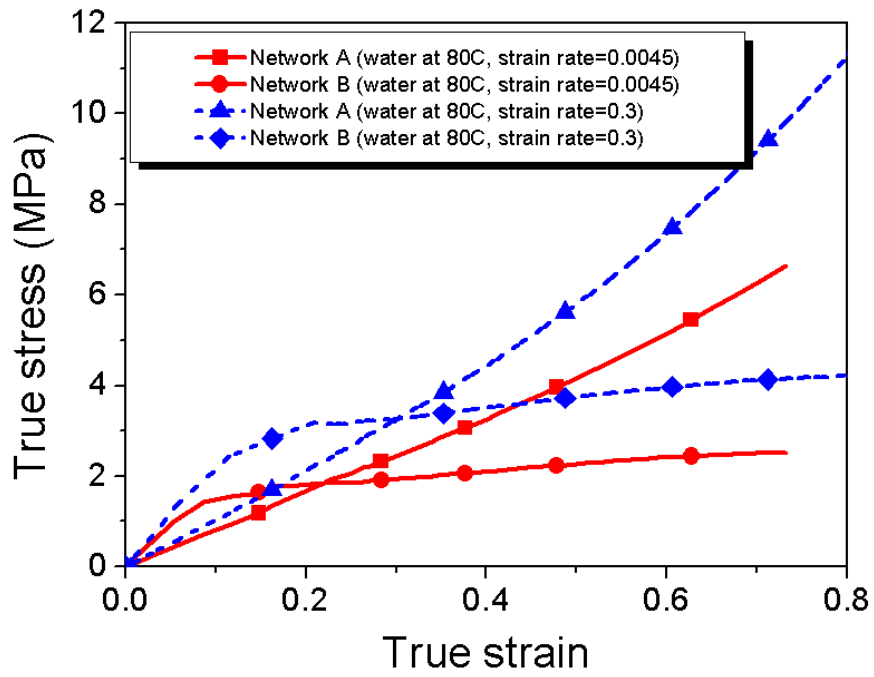
Figure 5-11 Comparison of contribution of each stress components for viscoelastic network A

and B from FEM simulation results for N111 at 80°C under the water at strain rate of 0.3/s

and 0.0045/s

Table 5-4 Material parameters for FEM simulation of water-equilibrated membranes at 80°C

C	-0.5
m	6
n	4.5
β	0.6
$\dot{\gamma}_0$	1
b	0.78
ε_0	0.01
s_{0A}	2.1
s_B	4
θ_{base}	100
κ	97MPa
λ_{lock}	6
E	25 MPa

Table 5-5 Material parameters adjusted for FEM simulation of water-equilibrated membranes

at 80°C

	Strain rate 0.3	Strain rate 0.0045
τ_{base}	$\mu_B *2$	$\mu_B *2.52$
a	0.1	0.2
σ_0	5MPa	3MPa
s_{0B}	0.077	0.0625

Finally, the stress acting on each component A and B are mainly determined by the magnitude of initial shear modulus μ_A which is hypothetically related to rubber like network such as the molecular chain entanglement in amorphous phase of ionomer membrane and is responsible for the hardening behavior, and μ_B being associated with intermolecular interaction including ionic clusters, polymer backbone, and side chains. It is observed that s_{0A}, a ratio of μ_A and μ_B is less than unity for the FEM analysis of the vapor-equilibrated membrane indicating that there is initial stiff response before the viscous flow come into play, but the magnitude of μ_A is almost two times greater than that of μ_B for the analysis of membrane immersed in a liquid water. Furthermore, the true strain at which the true stress components from network A and B intersect is approximately around 0.7 for the vapor

equilibrated membranes as can be seen in Figure 5-8 and Figure 5-9. However, the intersection point for the water equilibrated membranes is shifted down to a value less than 0.3. These observations suggest that a large amount of liquid water considerably weakens interactions in the hydrophilic domains, hence secondary interactions which might be present in the crystalline and amorphous phase dominates the stress-strain of the water equilibrated membrane, similar to the behavior of elastomeric materials.

CHAPTER 6   A MULTIPHYSICS MODEL FOR PEM FUEL CELL INCORPORATING THE CELL COMPRESSION EFFECTS

6.1 Introduction

The lifetime limitation of PEMs can result from a variety of factors, such as chemical degradation via radicals attack against the polymer backbone and side chain[182], and mechanical degradation due to swelling and shrink behavior via hygro-thermal cycling. It is reported that mechanical testing of fuel cell membranes subjected to hygro-thermal cycling shows permanent plastic deformation in the fuel cells due to thermal expansion and swelling [148, 151, 183], and that this could lead to crack initiation, membrane thinning, pinholes, and so on.   The mechanical stress can also result from assembly procedure of the cell, where clamping force may induce uneven deformation mostly in the gas diffusion layer (GDL) and membrane, which in turn, causes an uneven distribution of contact pressure, as well as the porosity and pore sizes under the channel and land areas of the bipolar plate. As a result, mass and charge transfer properties in the GDL can be affected [184]. Over compression of GDL impedes reactant transport and may damage GDL properties such as its hydrophobicity [185, 186]. Also, inhomogeneous contact pressure in the catalyst layer(CL)/ GDL and GDL/ bipolar plate (BP) interfaces can result in uneven electrical and thermal contact resistance, leading to decreased performance of fuel cells[112, 187, 188].

The influence of mechanical stress on membrane durability has been reported from different research groups and a lot of research efforts [148, 151, 183, 184, 189] have been made to simulate the stress and strain distribution in the membrane via fuel cell stack mechanical modeling. However there are very few papers discussing membrane stress and strain distribution in an operating fuel cell. Numerous research papers regarding fuel cell water and heat management, and stack mechanical modeling have been published, but many authors either disregards the effect of compression on the physical properties of the GDL or incorporates compression effect on electrical and thermal contact resistance analysis only[190-192]. This may be due to the complexity of the multiphysics coupling of the mechanical and fuel cell modeling and/or a limitation of commercial software capability to handle both the structural mechanics and fluid dynamics models together.

It was not until recently that relatively little attention has been paid to studying GDL's mechanical behavior under compression and its effect on fuel cell performance. Ihonan et al. [193] found that using high clamping pressures increases cell flooding, caused by a combination of decreased porosity and a temperature difference between GDL and current collector. The electrical conductivity of a GDL is also anisotropic and in- and through-plane conductivity are a function of compression force[111, 188]. Experimental approaches have been made to examine the mechanical, electrical, gas transport, and thermal properties of

126

GDLs [112, 113, 185, 188, 194-196] to better understand the complex problems involved in fuel cells. Kleemann et al. [19] performed mechanical testing to obtain orthotropic mechanical properties of several GDLs such as Poisson's ratio (v_{xy}), Young's modulus (E_x, E_y), and shear moduli (G_{xy}), which are independent material constants. A similar study was conducted by a different group [20] where they characterized GDLs in compressive, flexural, and shear tests and used the data in a finite element model to calculate the channel intrusion of GDL. Their study showed that a variation as little as 5% of GDL intrusion can result in a 20% drop of reactant flow in the most intruded channel and those results can generate more severe influence on performance in fuel cell stacks where there are multiple cells. Experiments were performed to obtain porosity and permeability data for compressed and uncompressed GDLs using a porosimetry technique and the data was used in a numerical simulation [113]. Hygro-thermal effect in PEMs along with the transport phenomena in fuel cells was studied with a non-isothermal and two-phase model[197], but the compression effects on gas transport and electrical properties of the GDL were not considered. Hottinen et al. [112] empirically obtained the geometric configuration of a compressed GDL and then utilized the data for fitting the permeability, porosity, in- and through-plane conductivities as a function of deformation. Recently, Zhou [114] implemented a sequential approach to investigate the effect of operating conditions such as temperature and RH on stack

127

deformation and other properties with respect to the assembly pressure by incorporating RH and temperature factors with GDL deformation. They developed a structural model first to investigate the stack deformation with respect to the clamping pressure, RH, and temperature and the change of material properties and contact pressure were calculated from the model. Then, these properties are used to solve the nonlinear multiphysics phenomena in fuel cells such as gas transport, electrochemical reactions, and charge transport.

In this research, we report an integrated multiphysics fuel cell model that incorporates the structural mechanics responses of fuel cell components including bipolar plate, gas diffusion layer, electrodes, and PEM. A two-dimensional, isothermal, and quasi-steady-state multiphysics fuel cell model was implemented with a finite element based numerical modeling package, COMSOL Multiphysics.

6.2 Model description
6.2.1 *Model assumptions*

The PEMFC model presented here is a 2D, isothemal, quasi-steady-state model of a sandwich domain denoted by an x-y coordinate system. The isothermal condition may not be a reasonable assumption due to the significant temperature gradient within the call, themal contact resistance, and coupled heat and mass transport processes, but in this research, the authors attempted to provide the general ideal of new FEM scheme to account for compression effect on fuel cell performance and non-isothermal study will be carried out near future. The model geometry is illustrated in Figure 6-1. Since the membrane mechanical model that we employed is a visco-elastic model, the time dependent solver was used to solve the mechanics sub-model. All other physics except for the structural mechanics are steady-state models and were solved with a stationary solver. A detailed description of the model is provided herein and the following are the main assumptions of our model:

(1) The fuel cell was operated under steady-state conditions.

(2) Phase change of water was considered only at the cathode GDE.

(3) The cell temperature was fixed at $80^{o}C$.

(4) The porous medium was assumed to have anisotropic and inhomogeneous

gas transport properties.

(5) No reactant cross-over through the PEM.

129

(6) The electrochemical reaction rates were described by the Butler-Volmer

     kinetic equations.

(7) A visco-elastic constitutive model, developed by the authors [198] and based on

     Bergström-Boyce model[164], was adopted for PEM mechanical model.

(8) The catalyst layer was modeled as an interface.

(9) Thermal contact resistance was ignored.

(10) A diffusion model was used for water content in membrane [199, 200].
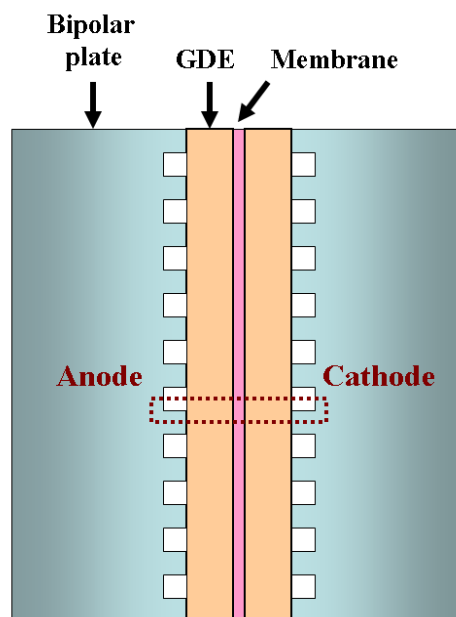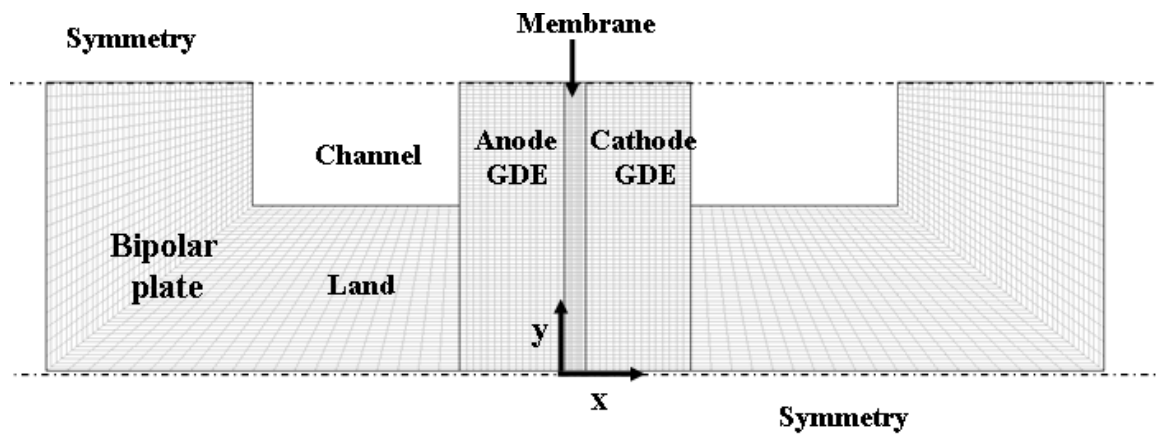
Figure 6-1 Computational domain for modeling

6.2.2 *Fuel cell model description*

6.2.2.1 Multicomponents gas transport

The conservation of momentum in the porous GDE can be described by Darcy's Law

(Eq. 6-1). Eq. 6-2 is obtained by combining Eq.6-1 with mass conservation equation,

$$u = -\frac{k_{th}}{\eta}\frac{\partial p}{\partial x}, \quad v = -\frac{k_{in}}{\eta}\frac{\partial p}{\partial y} \tag{6-1}$$

131

$$\frac{\partial}{\partial x}\left((1-s)\varepsilon_g \rho u\right) + \frac{\partial}{\partial y}\left((1-s)\varepsilon_g \rho v\right) = R_w \qquad (6\text{-}2)$$

where different through-plane and in-plane permeability are presented with subscripts *th* and *in*, respectively, and mass transfer in the form of evaporation ($R_w > 0$) and condensation ($R_w < 0$) is assumed, which is defined by the eq.(24). The ideal gas law gives the gas phase mixture density ρ:

$$\rho = \frac{p}{RT}\sum_i M_i x_i \qquad (6\text{-}3)$$

Due to the mechanical compression, change in volume of void space, not in volume of solid material is assumed and therefore, the porosity of the GDE can be calculated from the following equation[114]:

$$\varepsilon_g = \varepsilon_0 \left(\frac{V - V_s}{V_0 - V_s}\right) \qquad (6\text{-}4)$$

where ε_g is the porosity of GDE after the compression, ε_0 initial porosity of GDE, V the volume after the compression, V_{solid} volume of solid phase, and V_0 the uncompressed volume of GDE. In order to evaluate the volume of the compressed GDE, volume changes of individual mesh element before and after the compression were calculated from a deformation gradient F. The deformation gradient relates every material line element in the reference configuration to a corresponding element in the deformed configuration. The determinant of the deformation gradient represents the deformation of the volume element.

The volume of the solid phase is obtained from

$$V_s = (1 - \varepsilon_0) \cdot V_0 \tag{6-5}$$

The reduction of GDE porosity leads to a decrease in the gas permeability.

The permeability of porous materials is often described by the Carman-Kozeny equation[201, 202] and it is dependent on its porosity:

$$k = \frac{d_f^2 \cdot \varepsilon_g^3}{16 K_{CK}(1 - \varepsilon_g)^2} \tag{6-6}$$

where K_{CK} is Kozeny constant and d_f is fiber diameter. Therefore, the in- and through-plane gas permeability of the compressed GDE is evaluated as followings:

$$k_{th} = \frac{d_f^2 \cdot \varepsilon_g^{eff\,3}}{16 K_{CK\_x}(1 - \varepsilon_g^{eff})^2} , \tag{6-7}$$

$$k_{in} = \frac{d_f^2 \cdot \varepsilon_g^{eff\,3}}{16 K_{CK\_y}(1 - \varepsilon_g^{eff})^2} \tag{6-8}$$

$$\varepsilon_g^{eff} = \varepsilon_g(1 - s) \tag{6-9}$$

where s is liquid water saturation level.

The mass balance of gases in the GDE at anode and cathode is governed by the Stefan-Maxwell equation[197, 200, 203].

$$\nabla \cdot \left[(1 - s)\varepsilon_g \rho w_i \mathrm{u} - \rho w_i \sum_{j=1}^{n} D_{i,j}^{eff} \left\{ \left(\nabla x_j + (x_j - w_j)\frac{\nabla p}{p} \right) \right\} \right] = S_i \tag{6-10}$$

For the phase change in cathode GDE, R_w interfacial mass transfer rate between liquid and vapor water can be used as a source term for water vapor, which will be explained in the liquid water transport model below[197]. To account for different gas transport properties in the catalyst of the GDE, pseudo-thin layers were implemented between the GDE and membrane. All the source terms except the water vapor in cathode are set to zero. The sum of the mass fraction for the gases in the domain is unity, and therefore, the mass fractions of water at the anode and nitrogen at the cathode are expressed with respect to the mass fractions of other gases.

$$\sum_{i=1}^{n} w_i = 1 \tag{6-11}$$

In addition, the pressure and temperature corrections for binary diffusion coefficients were used and effective diffusion coefficients are calculated by a Bruggeman relation[204]:

$$D_{ij} = D_{ij}^0(p_0, T_0) \frac{p_0}{p} \left(\frac{T}{T_o}\right)^{1.5} \tag{6-12}$$

$$D_{i,j}^{eff} = D_{ij} \cdot \left(\varepsilon_g (1-s)\right)^{1.5} \tag{6-13}$$

The porosities and effective diffusion coefficients of the gases in the GDE are varied in position due to the volume change via compression and liquid water saturation s. The nominal values for diffusion coefficients at reference temperature and pressure are listed in Table 6-2.

Table 6-1 Material parameters and constant

Symbol	Description	Value	Reference
EW	Equivalent Weight of membrane	1.1 kg/mol	
ρ_m	Density of membrane	2000 kg m^{-3}	
ε_0	Porosity in the diffusion media of the GDE	0.6	
	Porosity in the catalyst of the GDE	0.3	
K$_{CK\_x}$	Carman-Kozeny constants for through plane direction	8.10	[201]
K$_{CK\_y}$	Carman-Kozeny constants for in plane direction	4.28	[201]
d$_f$	fiber diameter	9.2 μm	[201]
R	Gas constant	8.314 J mol^{-1} K^{-1}	
T	temperature	353K	
σ_{BPP}	Electron conductivity of bipolar plate	69700 S/m	[114]
$\sigma_{x,GDE}$	Electron conductivity of GDE in th-plane direction	1.4e+2 S/m	[114]
$\sigma_{y,GDE}$	Electron conductivity of GDE in in-plane direction	3.4e+4 S/m	[114]
A	Material parameter	3.72 mΩ cm^2	[205]
B	Material parameter	0.966 MPa	[205]
C	Material parameter	0.692	[205]
V_{H2}^{eq}	Equilibrium potential for Anode	0.0 V	[94]
$i_{o,H2}$	Exchange current density for hydrogen oxidation reaction	1.0e−3 A/cm$^2_{pt}$	[94]

135

Table 6-1

α_{H2}	Transfer coefficient	1.0	[94]
n_{H2}	Number of electron	2	[94]
V_{O2}^{eq}	Equilibrium potential for Cathode	1.23 V	[94]
$i_{o,O2}$	Exchange current density for oxygen reduction reaction	1.0e−9 A/cm²$_{pt}$	[94]
α_{O2}	Transfer coefficient	0.75	[94]
n_{O2}	Number of electron	4	[94]
L_{pt}	Platinum loading in electrode	4e−4 g/cm²	[94]
A_{pt}	Electrochemical Area of Pt	6e+5 cm²$_{pt}$/g	[94]
E_{BPP}	Young's modulus of bipolar plate	10,000 MPa	[114]
$v_{xy,BPP}$	Poisson ratio of bipolar plate	0.25	[114]
$E_{x,GDE}$	Young's modulus of GDE in th-plane	20 MPa	[195]
$E_{y,GDE}$	Young's modulus of GDE in in-plane	1000 MPa	[195]
$G_{xy,GDE}$	Shear modulus of GDE	10 MPa (estimated)	[195]
$v_{xy,GDE}$	Poisson ratio of GDE	0	[195]
k_c	Water condensation rate constant	100 s⁻¹	[206]
k_v	Water evaporation rate constant	9.869e-6 Pa⁻¹ s⁻¹	[206]
ρ_w	Water density at 80ºC	971.8 kg/m³	
μ_w	Viscosity of liquid water	3.5e-4 kg/m s	
$K_{w,0}$	Permeability of liquid water at 100% saturation level – diffusion media	1.1e-13 m²	[206]
	Permeability of liquid water at 100% saturation level – Catalyst of the GDE	3e-15 m²	[207]
$-\dfrac{dp_c}{ds}$	Diffusion media of the GDE	229.5 dyne/cm²	[206]
	Catalyst of the GDE	568.4 dyne/cm²	[207]

Table 6-2 Binary diffusivities at reference temperatures and 1 atm [200]

Gas pair	Reference temperature T_0 [K]	Binary diffusivity constant [m^2s^{-1}]
H_2-H_2O	307.1	0.915e-4
O_2-H_2O	308.1	0.282e-4
O_2-N_2	293.2	0.220e-4
H_2O-N_2	307.5	0.256e-4

6.2.2.2 Charge transport and electrochemical reaction kinetics

The charge conservation (for electrons) in GDEs and bipolar plates, and membrane (for protons) are assumed to be governed by the Ohm's law. The bulk electrical properties of the gas diffusion media, e.g., through-plane and in-plane conductivity, are dependent on compression [188]. The total cell electrical resistance (Ohmic) is dominated by the interfacial contact resistance[192], hence, the bulk electrical properties of the GDE were treated as constants for simplicity. The effect of the conductivity of GDE with respect to compression on fuel cell performance will be investigated in future study.

$$\nabla \cdot (\sigma_s \nabla \Phi_s) = 0 \quad \text{(s = bipolar plate, GDE)} \quad (6\text{-}14)$$

$$\nabla \cdot (\kappa_m \nabla \Phi_e) = 0 \quad (6\text{-}15)$$

The membrane proton conductivity is expressed by the following relationship between ionic conductivity and water content, λ [176].

137

$$\kappa_m = (0.5139\lambda - 0.326)\exp\left[1268\left(\frac{1}{303} - \frac{1}{T}\right)\right] \tag{6-16}$$

The rate of electrochemical reactions at the boundaries between GDE and membrane were expressed with the Tafel equations as follows[94] :

$$i_a = i_{o,H_2} L_{pt} A_{pt} \frac{p_{H_2}}{p_{H_2}^*} \exp\left\{\frac{\alpha_{H_2} n_{H_2} F}{RT}(V^a - \Phi_e - V_{H_2}^{eq})\right\} \qquad \text{for anode} \tag{6-17}$$

$$i_c = -i_{o,O_2}(1-s) L_{pt} A_{pt} \frac{p_{O_2}}{p_{O_2}^*} \exp\left\{-\frac{(1-\alpha_{O_2}) n_{O_2} F}{RT}(V^c - \Phi_e - V_{O_2}^{eq})\right\} \text{for cathode} \tag{6-18}$$

The effect of liquid water on the oxygen reduction reaction is accounted for in Tafel equation by the term $(1-s)$.

The interfacial contact resistance between the GDE and BP as function of the contact pressure is approximated by eq. 6-19, an empirical relationship reported by Mishra et al. [205]

$$\rho = A\left(\frac{B}{p}\right)^c \tag{6-19}$$

where p is the contact pressure which is calculated from the structural mechanics and A,B, and C are parameters determined by experimental data reported in the reference [190].

138

6.2.2.3 Water content in membrane and liquid water transport

In the membrane, the net water transport can be described by a back-diffusion process governed by the water concentration gradient, and an electro-osmotic migration proportional to the ionic current density.

$$N_w = \frac{i_+}{F} n_d - D_w^m \nabla C_w^m \qquad (6\text{-}20)$$

$$\nabla \cdot N_w = 0 \qquad (6\text{-}21)$$

$$D_w^m = \begin{cases} 3.1 \times 10^{-3} \lambda (e^{0.28\lambda} - 1) \cdot e^{-2436/T} & for\ 0 < \lambda < 3 \\ 4.17 \times 10^{-4} \lambda (1 + 161 e^{-\lambda}) \cdot e^{-2436/T} & otherwise \end{cases} \quad [208] \qquad (6\text{-}22)$$

$$\lambda = C_w^m \cdot \frac{EW}{\rho_m} \qquad (6\text{-}23)$$

For liquid water in the cathode GDE, the mass transfer rate of water per unit volume between the gas and liquid phases, R_w is defined as [206]

$$R_w = \left(k_c \frac{\varepsilon_g (1-s) x_w}{RT} (x_w p - p^{sat}) q + k_v \frac{\varepsilon_g s x_w}{M_w} (x_w p - p^{sat})(1-q) \right) \qquad (6\text{-}24)$$

where k_c and k_v are the condensation and evaporation rate constants, x_w mole fraction of vapor water in the gas phases, p and p^{sat} are operating pressure and water vapor saturation pressure at operating temperature. The switching function q is used to determine whether the water partial pressure exceeds the water saturation pressure [206, 209].

$$q = \frac{1 + \left| x_w p - p^{sat} \right| / (x_w p - p^{sat})}{2} \qquad (6\text{-}25)$$

139

In the cathode, the liquid water transport in the GDE is assumed to be driven by capillary force. Flow of liquid water in the porous media can be described by Darcy's law[197, 206, 207].

$$N_w = -\frac{\rho_w K_{w,0}}{M_w \mu_w}\left(-\frac{dp_c}{ds}\right) \cdot s\nabla s \qquad (6\text{-}26)$$

where ρ_w, μ_w, and $K_{w,0}$ are the density, viscosity, and permeability of liquid water, respectively. The capillary pressure p_c is a function of liquid water saturation level and in this model, dp_c/ds is assumed to be a constant for simplicity. The governing equation for the liquid water in the GDE is

$$-\nabla \cdot N_w + R_w = 0 \qquad (6\text{-}27)$$

6.2.3 *Structural modeling*

As for structural models, plane strain model was used for BP, GDE, and membrane. The BP was assumed to be isotropic linear elastic, the GDE orthotropic linear elastic [195], the membrane viscoelastic. The material parameters used for the above models are listed in Table 6-1 above. For the orthotropic material, four independent material parameters E_x, E_y, G_{xy}, and ν_{xy} must be determined as can be seen in Eq. 6-28 .

$$\begin{bmatrix} \sigma_x \\ \sigma_y \\ \tau_{xy} \end{bmatrix} = \begin{bmatrix} \dfrac{E_x}{1-\nu_{xy}\nu_{yx}} & \dfrac{\nu_{xy}E_y}{1-\nu_{xy}\nu_{yx}} & 0 \\ & \dfrac{E_y}{1-\nu_{xy}\nu_{yx}} & 0 \\ Symm & & G_{xy} \end{bmatrix} \begin{bmatrix} \varepsilon_x \\ \varepsilon_y \\ 2\varepsilon_{xy} \end{bmatrix} \qquad (6\text{-}28)$$

Details about the constitutive model for the ionomer membrane is given in our recent publication [198]. A brief mathematical description of the constitutive behavior of the ionomer membranes is presented here. The model is based on the breakdown of the overall deformation into the viscoelastic and hygrothermal deformation[210]. A rheological representation of the proposed model is shown in Figure 6-2. The deformation gradient F is multiplicatively decomposed into the viscoelastic part and the hygro-thermal part as shown below:

$$F = F^{ve}F^{ht} \qquad (6\text{-}29)$$

where F^{ht} is the deformation purely due to the hygro-thermal effect and $F^{ve} = F^A = F^B$ is the remaining contribution to F. Isotropic swelling due to temperature and RH was considered and a third degree polynomial was employed for the swelling strains[183].

The hygro-thermal strain is approximated to be infinitesimal strain for simplicity and the mathematical relation between the hygro-thermal strain and deformation gradient F^{ht} are shown below [148]:

$$\varepsilon^{ht}(T, RH) = \sum_{i,j=1}^{4} C_{ij} T^{4-j} RH^{4-i} \tag{6-30}$$

$$\mathrm{F}^{ht} = \begin{bmatrix} 1+\varepsilon^{ht} & 0 & 0 \\ 0 & 1+\varepsilon^{ht} & 0 \\ 0 & 0 & 1+\varepsilon^{ht} \end{bmatrix} \tag{6-31}$$
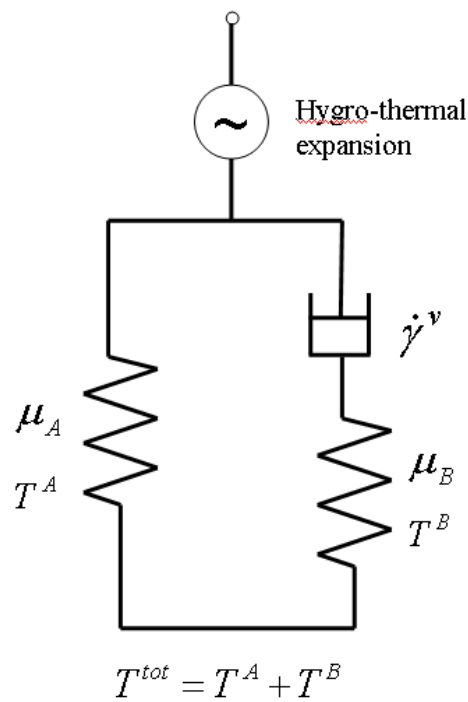
Figure 6-2 Schematic representation of membrane model

The viscoelastic deformation gradient is further decomposed into the elastic and the

viscous parts[164].

$$\mathrm{F}^{ve} = \mathrm{F}^{e}\mathrm{F}^{v} \tag{6-32}$$

142

Here, F^e is the elastic deformation gradient and F^v expresses the viscous deformation gradient. The spatial velocity gradient L is given by $L = \dot{F} \cdot F^{-1}$. The velocity gradient of the viscoelastic part can be decomposed into the elastic and the viscous components: $L^{ve} = \dot{F}^{ve}F^{ve-1} = L^e + \widetilde{L}^v$, where $\widetilde{L}^v = \widetilde{D}^v + \widetilde{W}^v$. The rate of deformation, $\widetilde{D}^v$ and spin tensors, $\widetilde{W}^v$ are defined as the symmetric and skew-symmetric parts of $\widetilde{L}^v$.

The rate kinetic for the hygro-thermal deformation was ignored due to the complex behavior of water absorption and desorption in ionomer membrane and therefore, the steady-state deformation was assumed and is determined by current relative humidity and temperature using eq.(6-30) and (6-31); $\dot{F}^{ht} = 0$.

The rate of viscous flow of the network B can be described by $\widetilde{D}^v = \dot{\gamma}^v N^v$. The tensor N^v represents the direction tensor of the driving deviatoric stresses of the relaxed configuration, and the terms $\dot{\gamma}^v$ indicates the flow rates being given by the reptation-inspired mechanism[164]:

$$\dot{\gamma}^v = \dot{\gamma}_0 [\overline{\lambda}^v - 1]^c \cdot \left(\frac{\tau^e}{\tau_{base} + \beta p^e} \right)^m \cdot \left(\frac{\theta}{\theta_{base}} \right)^n \tag{6-33}$$

where, $\tau^e = \left\| \mathbf{T^{e'}} \right\|_F \equiv (tr[\mathbf{T^{e'}T^{e'}}])^{1/2}$ is the Frobenius norm of $\mathbf{T^{e'}} = \mathbf{dev}[\mathbf{T^e}]$, the direction of the driving stress is described by $N^v = T^{e'}/\tau^e$, $\overline{\lambda}^v = \sqrt{tr(B^{v*})/3}$ is an effective viscous chain stretch, $\mathbf{B}^{v*} = (J^v)^{-2/3}\mathbf{F}^v(\mathbf{F}^v)^{\mathbf{T}}$ is the left Cauchy Green deformation tensor, $p^e = -(T_{11}^e + T_{22}^e + T_{33}^e)/3$ is the hydrostatic pressure, and

143

$C \in [-1,0], m > 0, n, \beta, \dot{\gamma}_0, \theta_{base}$ and τ_{base} are material parameters, which are defined at Table.3.

The parameters are associated with the reptational dynamics scaling law, and stress and temperature dependent deformation rate.[164, 211]

It should be noted that the intermediate configurations described by V are, in general, not uniquely determined[172], and one convenient way is to prescribe $\widetilde{W}^v = 0$, which means that the flow is irrotational [173]. In addition to that, viscous deformations are assumed to be incompressible, i.e., $\mathbf{det}(\mathbf{F}^v) = 1$.

The Cauchy stress tensor for network A and B is given by the eight-chain representation[144, 164, 198]:

$$T^A = f_{8ch}(F^{ve}) = \frac{\mu_A}{J^{ve}\overline{\lambda^{ve}}} \cdot \frac{\mathcal{L}^{-1}(\overline{\lambda^{ve}}/\lambda^{lock})}{\mathcal{L}^{-1}(1/\lambda^{lock})} \mathrm{dev}[\mathrm{B}^{ve*}] + \kappa[J^{ve}-1]\mathbf{1} \qquad (6\text{-}34)$$

$$T^B = s_B \cdot f_{8ch}(F^e) = s_B \cdot \left(\frac{\mu_B}{J^e\overline{\lambda^e}} \cdot \frac{\mathcal{L}^{-1}(\overline{\lambda^e}/\lambda^{lock})}{\mathcal{L}^{-1}(1/\lambda^{lock})} \mathrm{dev}[\mathrm{B}^{e*}] + \kappa[J^e-1]\mathbf{1} \right) \qquad (6\text{-}35)$$

where $J^{ve} = \mathrm{det}[\mathrm{F}^{ve}]$, μ_A and μ_B is a temperature and hydration level dependent initial shear modulus, λ^{lock} is the chain locking stretch, $\mathrm{B}^{ve*} = (J^{ve})^{-2/3}\mathrm{F}^{ve}(\mathrm{F}^{ve})^{\mathrm{T}}$ is the left Cauchy Green tensor, $\overline{\lambda^{ve}} = \sqrt{tr(\mathrm{B}^{ve*})/3}$ is the effective chain stretch based on the eight-chain representation, $\mathcal{L}^{-1}(x)$ is the inverse Langevin function, where $\mathcal{L}(x) = \coth(x) - 1/x$, and κ is the bulk modulus.   Then, the total Cauchy stress is the sum of the two resultants, namely $T = T^A + T^B$.

The reference condition for membrane deformation by hygro-thermal state is set to 25ºC and 30%RH.

Table 6-3 Material constants for ionomer membrane

C	-0.6
m	7
n	2.5
β	0.3
τ_{base}	11 MPa
$\dot{\gamma}_0$	1
μ_A	E / 40
μ_B	μ_A
s_B	8
θ_{base}	100 ºC
κ	97 MPa
λ_{lock}	6

6.2.4 *Boundary conditions*

The mole fractions of H_2, H_2O, and O_2 for Stefan-Maxwell equation and inlet pressure which is slightly higher than atmosphere for Darcy's Law are prescribed at GDE inlet (boundary 1 and 11). Flux boundary conditions are used for interfaces between electrode

145

and membranes (boundary 5 and 8) due to electrochemical reaction. All the other boundaries except for the inlet (1 and 11) and the interfaces are set to symmetry/insulation condition.

$$N_{H_2} = \frac{i_a}{2F} M_{H_2}, \quad N^a_{H_2O} = n_d \frac{i_a}{F} M_{H_2O}, \quad N_{O_2} = \frac{i_c}{4F} M_{O_2} \tag{6-36}$$

An electric potential is applied to the outer boundaries of the BP (not shown in Figure 6-3). The current flows i_a and i_c from the Tafel equations are set to boundary 5 and 8 and all other boundaries are set to insulation.

Water concentration at the anode and the cathode is set at the boundaries between GDE and membrane. Water concentration in the membrane is calculated by the following equation.

$$C_w = \lambda \cdot \frac{\rho_m}{EW}$$

$$\lambda = \begin{cases} 0.043 + 17.81a - 39.85a^2 + 36a^3 & for \ a \leq 1 \\ 14 + 1.4(a-1) & for \ otherwise \end{cases} \tag{6-37}$$
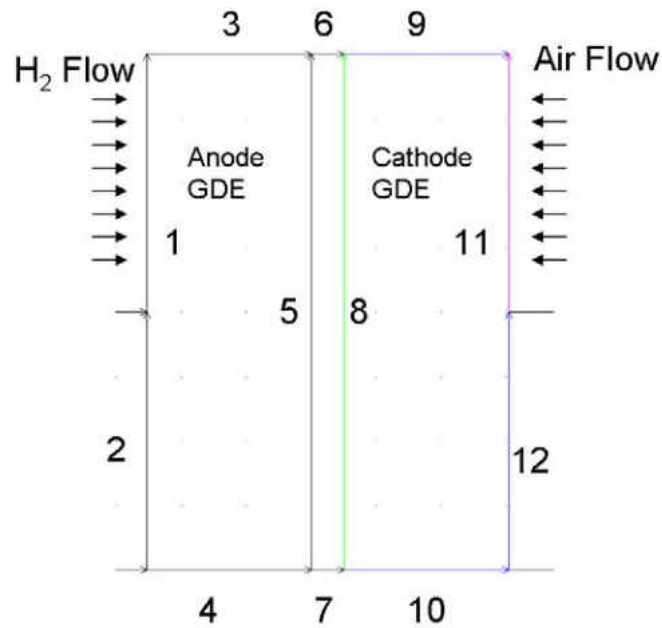
Figure 6-3 Boundaries of computational domain

Liquid water flux at boundary 8 in the cathode GDE is assumed to be related to the water generation rate and the electro-osmotic drag. The inlet water saturation level is set according to the gas humidification level.

$$N_w = -\frac{i_c}{F}(n_d + 1/2) \tag{6-38}$$

Displacement inputs (5, 25, and 50μm) are applied to both ends of bipolar plates and free and symmetry conditions are set to appropriate boundaries. We define the "pinch" of the GDE as the reduction of GDE thickness after compression (pinch = $t_{initial} - t_{compressed}$) and

147

define the percentage cell compression as the ratio of the pinch of the GDE over the initial thickness of the GDE.

6.3   Results and discussions

The governing equations for the structural mechanics along with their boundary conditions were solved first to compute an initial deformed mesh as illustrated in Figure 6-4. All other multiphysics equations were solved in the deformed configuration. Parameter such as volumetric ratio of GDL mesh elements before and after the compression was utilized as an initial condition for the calculation of the current GDL porosity. For membrane stress analysis, the structural mechanics equations were solved again with the current solutions after the above steps.
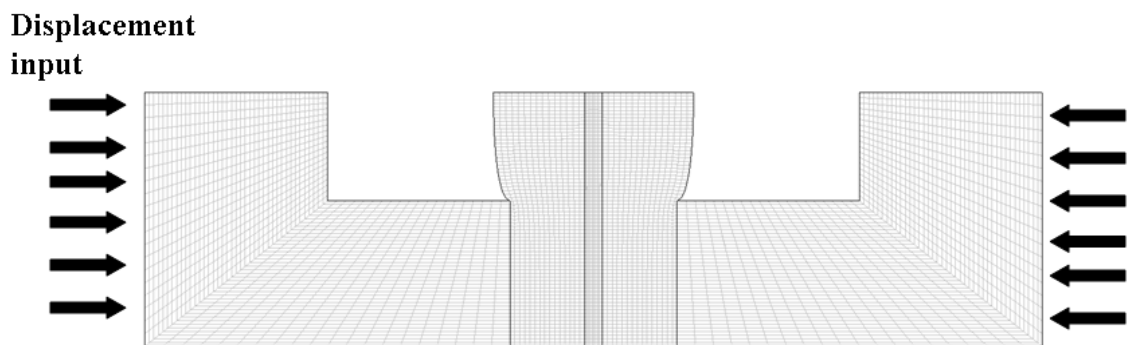
Figure 6-4 The deformed mesh used for fuel cell modeling

The fuel cell performance (I-V) curves at three levels of cell compression are shown in Figure 6-5. The reactant gases were fully humidified. Comparison of the polarization

148

curves exhibits that the effects of compression on I-V curves are more pronounced at high

current density and at higher cell compression, and the trend is consistent with experimental

results[212, 213]. Cell compression at 10% (25um pinch) lowers the electrical contact

resistance than that of the 5% cell compression, thus the total current density increased

slightly.
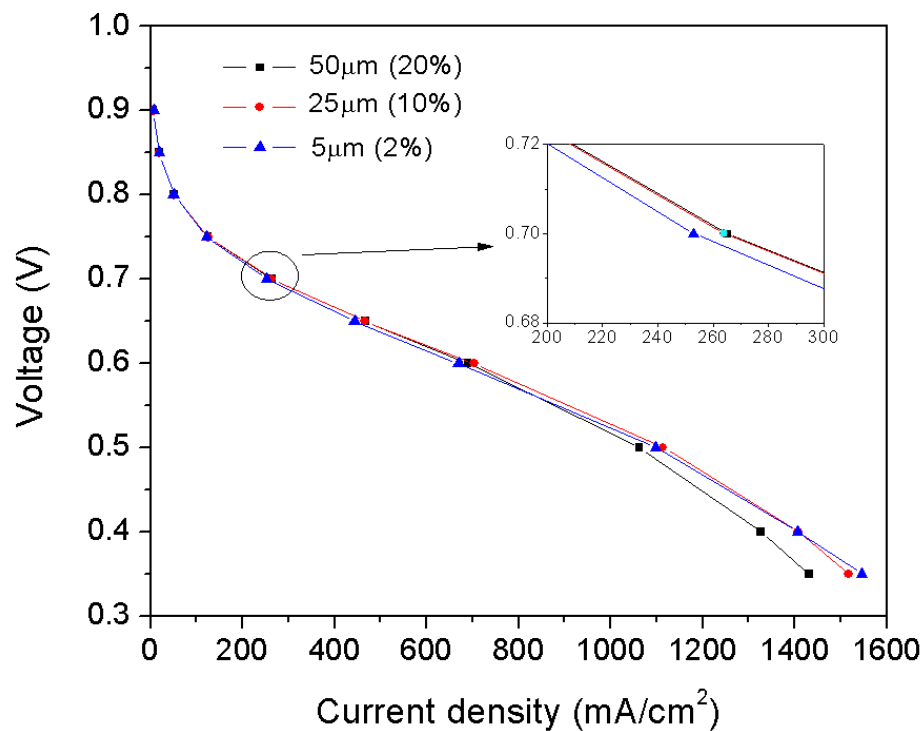
Figure 6-5 Polarization curves with respect to displacement input at 100% RH and 80°C

However, this trend become opposite at high current density, where total current

density from the 5% cell compression case exceeds the current density from the 10% cell

149

compression case due to the mass transport losses.   At 20% cell compression, the transport

limitation becomes more pronounced at high current density.
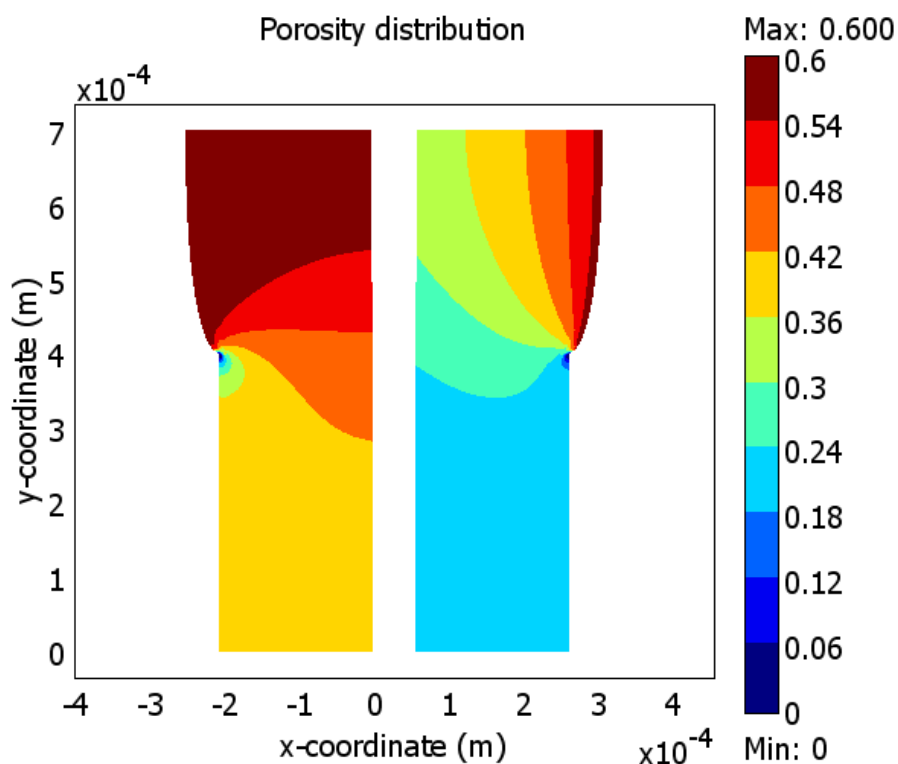
Figure 6-6 Porosity distribution at 0.6V (690 mA/cm^2), 100% RH, and 20% compression
(50μm) of initial thickness of GDE

Both the liquid water saturation and the compression affect GDE porosity distribution.

Figure 6-6 shows the distribution of anode and cathode GDE porosity at 20% cell

compression and a cell voltage of 0.6V.   Liquid water in the cathode GDE reduces the free

void space within the GDE, thus the porosity in the anode and cathode GDE shows different

distribution pattern.   At the area under the land in the cathode, it has higher liquid water

saturation than the area under the channel. Porosity at the upper edge of land becomes almost

zero because of stress concentration near the edge.
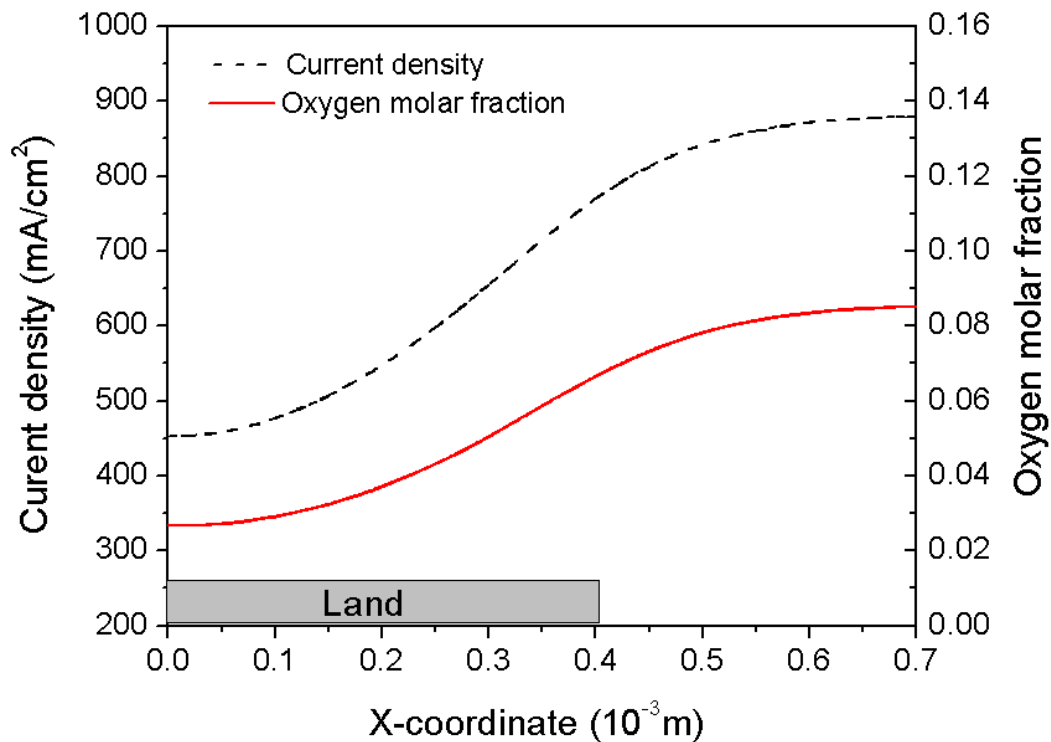
Figure 6-7   Current density profile and oxygen molar fraction at cathode at 0.6V

(690 mA/cm^2), 100% RH, and 20% compression (50μm) of initial thickness of GDL

The liquid water saturation and inhomogeneous porosity distribution affect gas

transport in the GDE and hence oxygen molar fraction at the catalyst layer as well.

Accordingly, the oxygen molar fraction profile and current density profile are affected, as can

be seen in Figure 6-7.

Figure 6-8 shows porosity distribution induced by purely mechanical compression.

Initial porosity of GDE is set to 0.6.   As the compression increases, the porosity of mesh

المنارة للاستشارات
www.manaraa.com

elements around a region closed to edge of the land decrease rapidly and GDE intrusion occurs at the GDE surface facing the reactant gas channel.   The compression can potentially damage the GDE structure severely, altering its hydrophobicity[214].   Furthermore, the porosity along the y-direction close to the cathode catalyst distributes widely in values with displacement input ($0.49 < \varepsilon_g < 0.6$ at 25μm, $0.40 < \varepsilon_g < 0.6$ at 50μm, $0.32 < \varepsilon_g < 0.6$ at 75μm), and the area of the region with the highest porosity keeps decreasing at the channel inlet as the displacement input is increased, implying that mass transport loss become a dominant factor on the performance degradation.   It has been shown[214] that irreversible damage to the GDL, such as fibers breaking and PTFE coating disintegrating, can occur at compression pressures as low as 0.18 MPa.   The compressive stress in the GDE under the land from our FEM analysis was more than 5MPa at 75μm displacement input.   This stress level is high enough to damage the GDE and consequently would affect liquid water and gas transport dynamics.

Porosity

(a)

Porosity

(b)

153
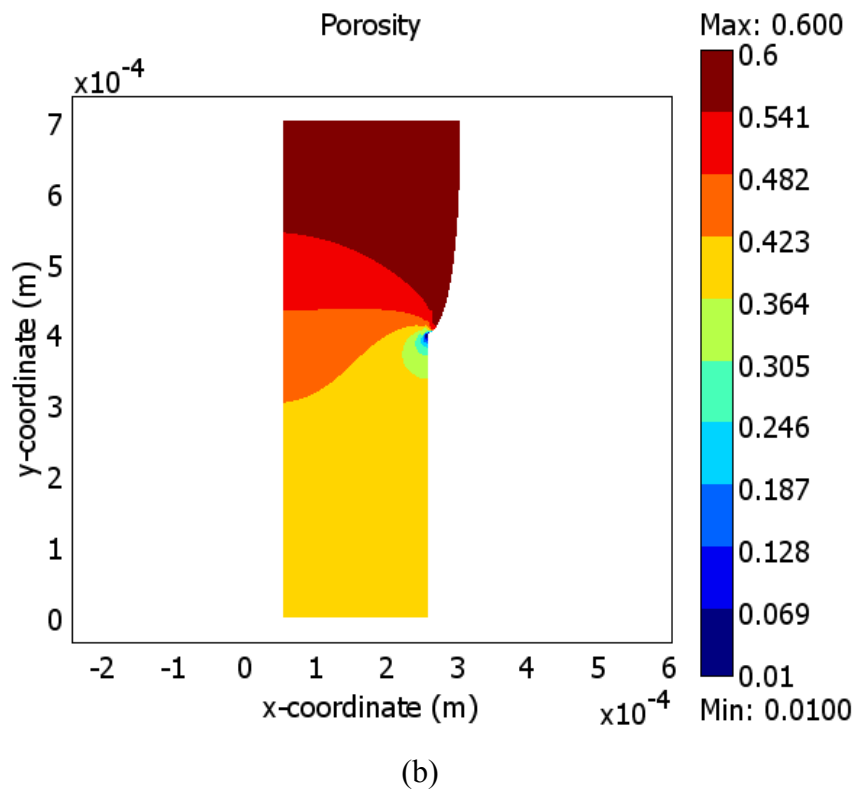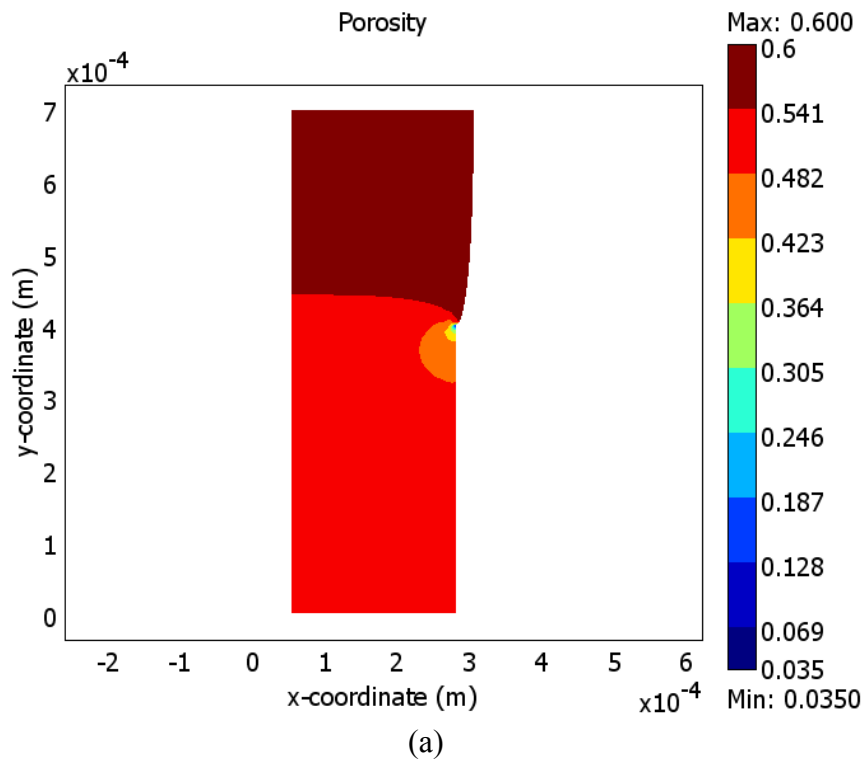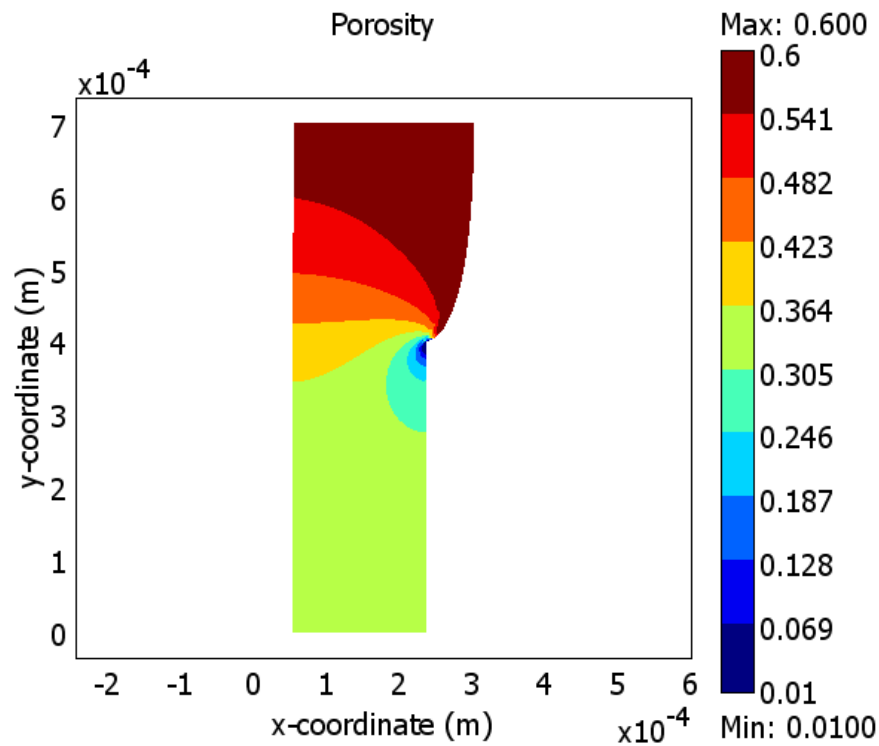
(c)

Figure 6-8 Porosity distribution in cathode GDE with respect to displacement input of (a) 25μm (10%), (b) 50μm(20%), and (c)75μm(30%)

Cell compression influences electrical properties of the GDL as well as its porosity and tortuosity. However, the fraction of the ohmic drop resulting from the change of the bulk electronic conductance of the GDE was reported to be negligible due to the intrinsic high electron conductivity [213] of the solid phase.

154

In order to further examine cell compression effect on fuel cell performance, current density profiles were compared with respect to displacement inputs. Figure 9 shows the change of the channel/land current distribution when the displacements are increased from 5 to 50μm at 0.65V and 0.5V and 100%RH. It is obvious that the maximum current density under the channel is increased with increasing displacement. The predicted pattern is expected to be caused by the change of gas reactant distribution due to the compression and this is consistent with the experimental results[213]. Since the gas transport properties are changed by the compression, in-plane reactant gas flow experienced more resistance than through-plane gas flow, and hence, more gases react at the catalyst layer under the channel.

0.65V at 100%RH
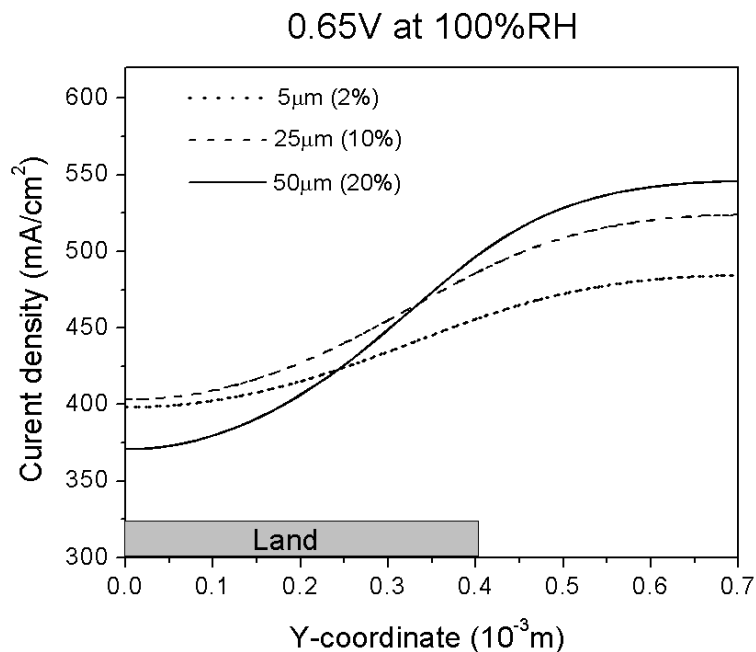
(a)
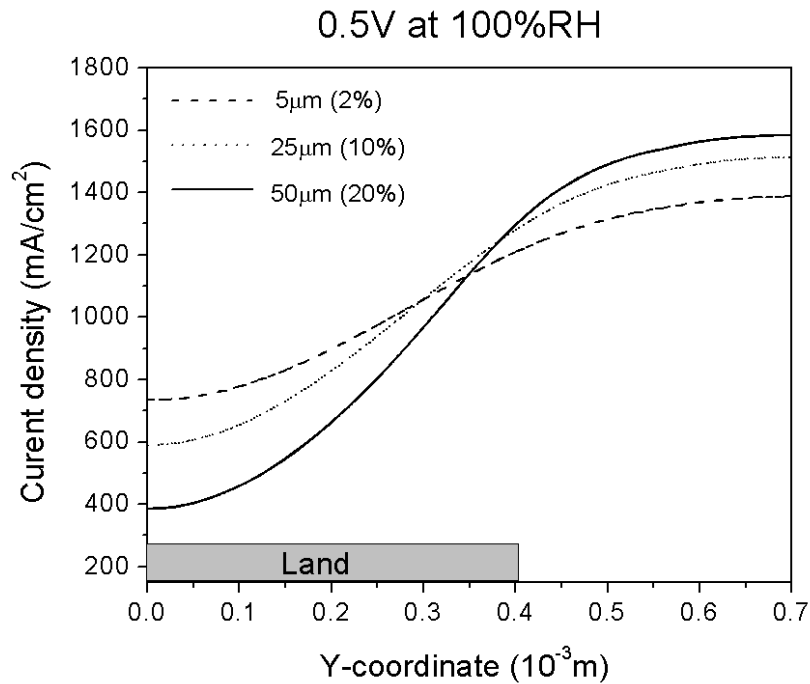
(b)

Figure 6-9 Current density distribution at (a) 0.65V, and (b) 0.5V and 100% RH with respect

to mechanical compression (displacement input of 5, 25, and 50μm)

On the other hand, moderate compression (25μm) can decrease contact resistance

between BP, CL, and GDL, and thus current density under the land can be increased.

However, further compression (50μm) impedes gas transport, eventually lowering the current

density to below the level at 5μm compression under the land.   At Figure 6-9(b), it appears

that higher current density negates the benefit from the lower contact resistance under the

land.   Even at 25um compression, the current density under the land is below that at 5um,

indicating that mass transport is impaired by the liquid water and compression.   Our results

156

show that the contact resistance and the mass transport loss are two competing factors that contribute to the variation of overall performance of fuel cells as well as the current density distribution under different level of cell compression. Our FEM model can be used as a simulation tool to optimize the cell compression level with respect to different GDLs with various gas transport, structural, and interfacial contact properties.

In addition, a large difference in values between the minimum and the maximum current density at high current greatly affects the distribution of membrane water content and proton conductivity. Apparently, the cell compression dramatically influences the channel/land current distributions by the changes of local transport properties and too much compression deteriorates overall performance by mass transport loss.

In the results presented so far, only the contact resistance between BPs and GDE was taken into account. It has been reported that the values of the contact resistance between the catalyst layer and GDL turned out to be more than one order of magnitude larger than the contact resistance between the GDL and BP [192]. In order to investigate the effect of the contact resistance between the GDL and the catalyst layer in fuel cells, contact resistance was applied to the pseudo-thin layer between the GDL and the membrane, the contact resistance values were taken from the literature[192]. The current density profiles with respect to two different voltage inputs of 0.7V and 0.3V were examined with 25μm displacement input.

157

The results are shown in Figure 6-10.   At low current, the current density at the land area is

higher than that at the channel, however, this trend becomes opposite at high current. This

trend is quite similar with the current density profile measured by experiment[111].   The

contact resistance between GDL and catalyst layer can affect the current density profile

considerably at both low and high current, which cannot be seen when the contact resistance

between GDL and BP is considered only.
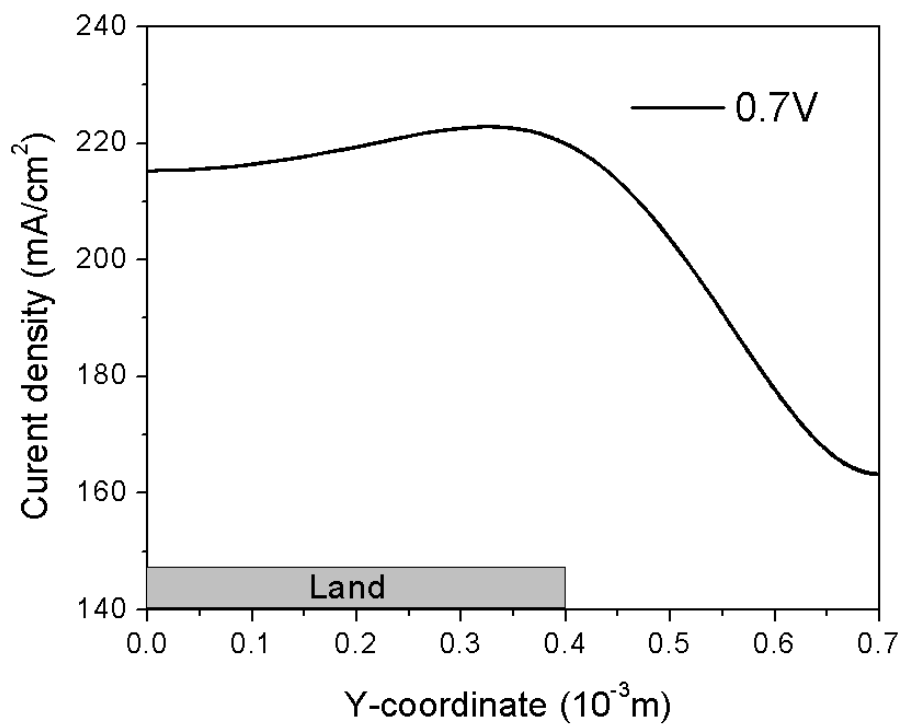
(a)
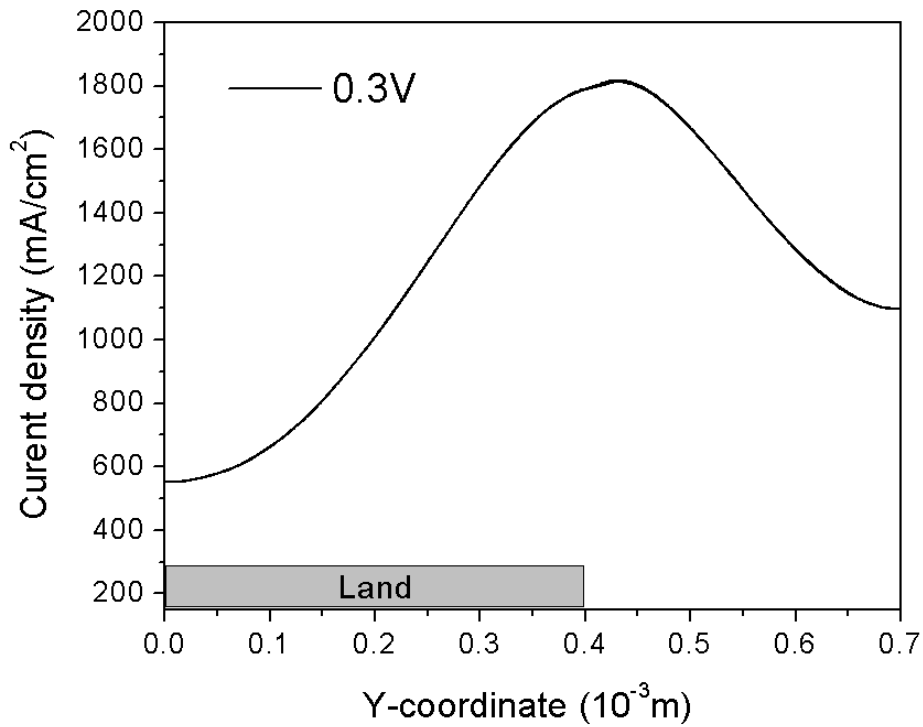
(b)

Figure 6-10 (a) Current density profile at 0.7V (207 mA/cm^2) and (b) 0.3V (1250 mA/cm^2) when the contact resistance between the GDE and membrane is considered (25μm displacement input)

Membrane mechanical failure itself is a critical factor limiting the lifetime of fuel cells. Mechanical stress is a factor in membrane mechanical failure. Other factors include the formation of cracks and pinholes. Membrane mechanical stress is dependent on hygro-thermal expansion as well as compression. In this model, the membrane elastic modulus can be calculated from temperature and water content profile, which is the solution of the water diffusion equation. Due to water generation at the cathode, the water content at the

cathode side is higher than that at the anode side.   As a result, the water content gradient

induces a gradient of membrane mechanical properties such as the elastic modulus.

(a)

(b)

160

Through-plane true stress [MPa]   Max: -0.215
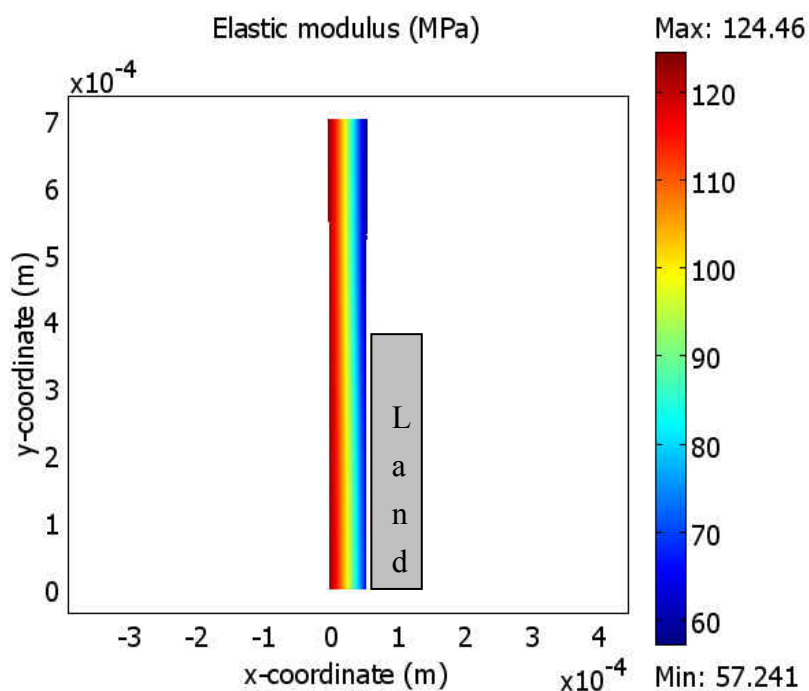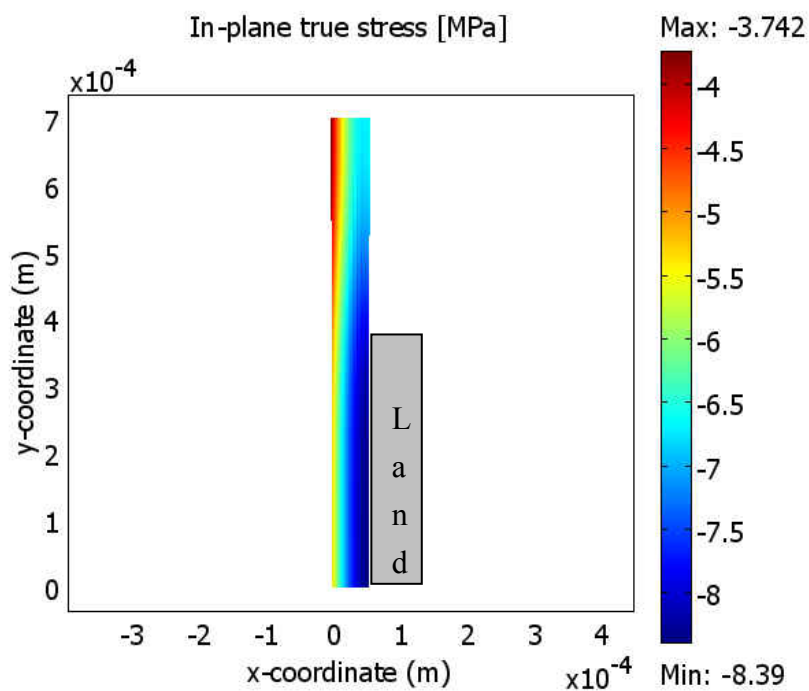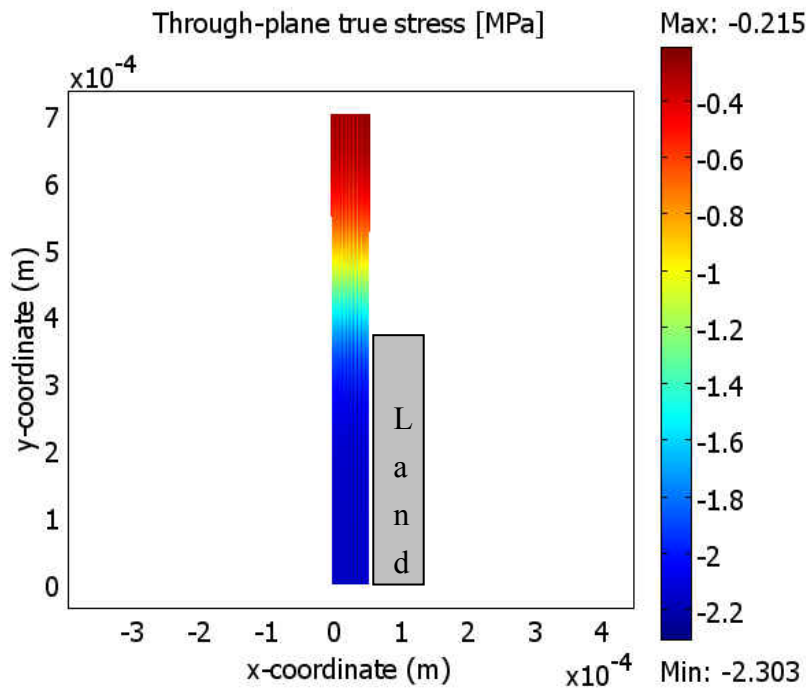
(c)

Figure 6-11 (a) Membrane elastic modulus (MPa) distribution and (b) in plane (y-direction) stress distribution and (c) through-plane stress distribution at 0.6V and 60% RH with displacement input of 25um

Figure 6-11(a) plots the elastic modulus distribution in a membrane at 0.6V and 60%RH. The through-plane deformation is expansive on both sides and in-plane deformation is compressive due to the symmetry boundary condition. The in-plane stress is typically larger than the through-plane stress and the compressive stress in membrane under the land is greater than that under the channel as can be seen in Figure 6-11(b) and (c); this result is attributed to the geometrical constraint of the membrane under the land, because

161

there is not much freedom for membrane to expand due to the GDL compression by the land.

The through plane stress distribution across the membrane in Figure 6-11(c) was compared

with pressure distribution measured by pressure sensitive film and the stress range calculated

by the FEM (31 ~ 333.98 psi)   is approximately within the pressure range (75 ~ 350 psi)

obtained from experiments[215]. The stress level and distribution due to hygro-thermal

expansion are also dependent on current density (as shown in Figure 12).

(a)

In-plane true stress [MPa]
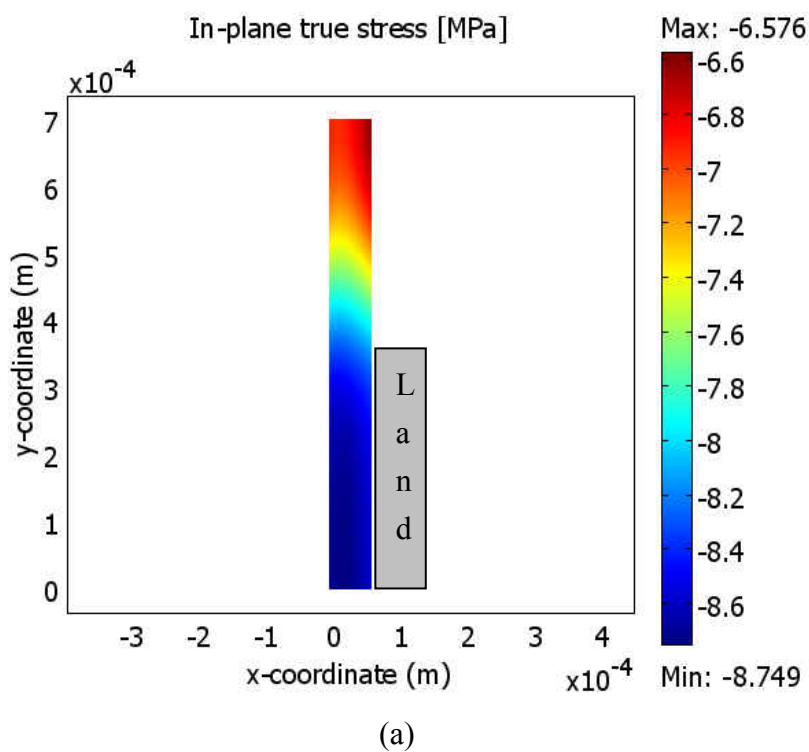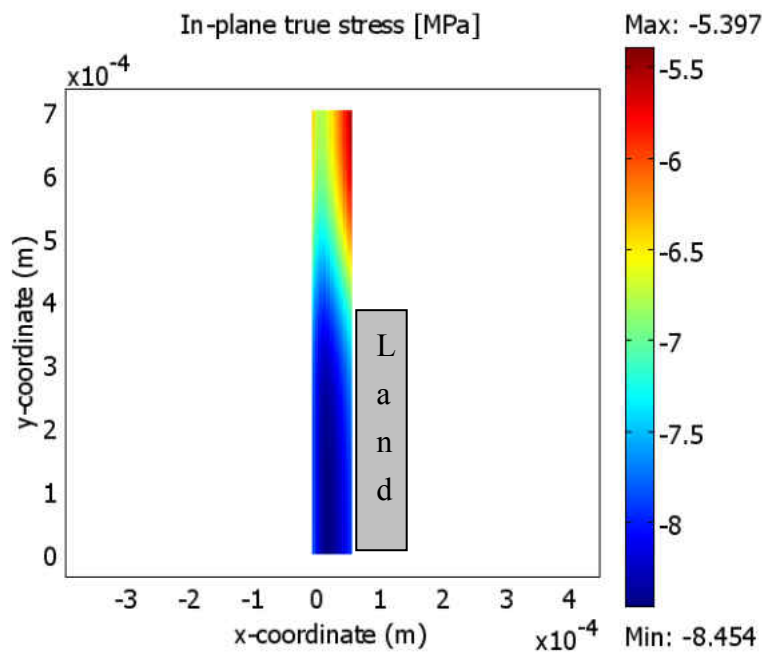
(b)

Figure 6-12 (a) In plane (y-direction) stress distribution at 0.7V (297 mA/cm^2) and (b) at

0.6V (656 mA/cm^2), and 80% RH with displacement input of 25um

During fuel cell operation, various electric load, temperature, and RH condition are

expected. Our simulation results show that a slight change of those conditions would affect

both the stress level and the stress distribution pattern in the electrolyte membranes

significantly.   Under our modeling assumptions, it is observed the dominant stress state

during cell operation is compressive both in-plane and through-plane.   Under the

compressive stress, the membrane can wrinkle at locations where there is insufficient

structural support by the GDL.   The tensile stress can occur when there is severe

dehydration in part of the fuel cell. The result is presented in Figure 6-13, where in-plane

163

stress state is tensile when the membrane is equilibrated at 10% RH (Structural mechanics model was solved only).
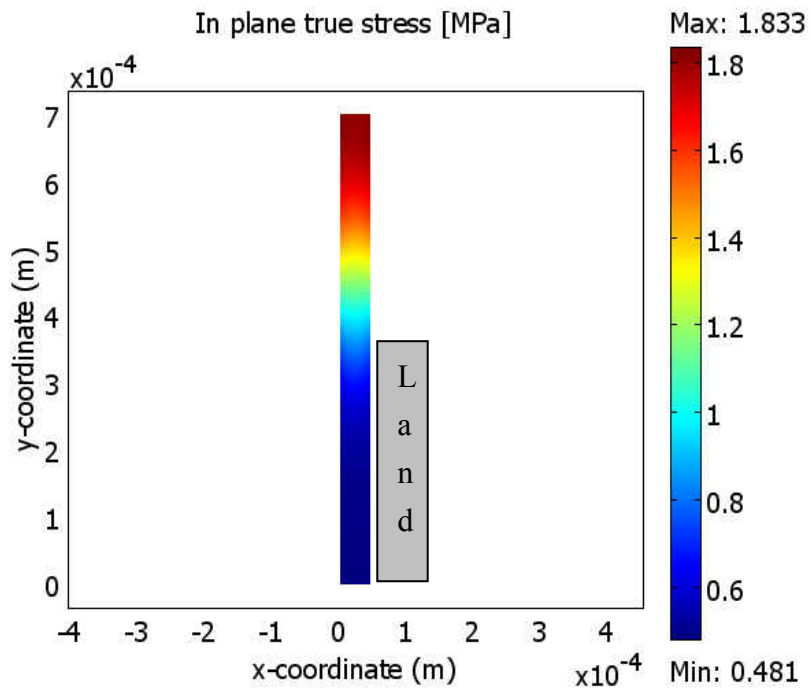
Figure 6-13 In plane (y-direction) stress distribution in membrane equilibrated at 10% RH with displacement input of 25um

CHAPTER 7   CONCLUSIONS AND FUTURE WORKS

The bi-layer membrane configuration for the study of the membrane degradation under the OCV was successfully demonstrated and generated interesting results for gaining further insights to the membrane degradation mechanisms.   The OCV tests at 30%RH and 80ºC were conducted to accelerate the membrane degradation in fuel cells and two different sets of gas composition at anode and cathode were employed to understand the differences in degradation pattern, which is suspected to be caused by radicals generated on or near the platinum particles[116].   From the SEM-EDS measurements, it is confirmed that the Pt band is formed at different location with two sets of gas composition based on several references[27, 65, 75, 92, 100] and it can provide main reaction sites for the crossover H_2 and O_2 to generate radicals. The FE, FTIR, and mechanical test results indicate that the cathode side membrane has been subjected to more degradation in H_2/Air OCV test and the opposite trend was observed in 4%H_2/O_2 OCV test, i.e., the anode-side membrane were degraded more than the cathode-side membrane. Both results imply that the membrane degradation is highly localized across the thickness direction of the membrane and qualitatively correlated with the location of the Pt band, which is expected to be formed mainly in the cathode side membrane under hydrogen and air OCV test, and mostly in the anode side membrane under diluted hydrogen and pure oxygen OCV test.   After OCV tests, in addition to the Pt band

165

formation, very fine (nanometer-sized) Pt particles are broadly distributed across the membrane[24]. However, these fine Pt particles do not result in a uniformly weakened membrane. So, whether Pt particles precipitated inside the membrane have notable catalytic effects on membrane degradation may depend on the size and/or the location of the Pt particles inside the membrane. The low FE observed when low H_2 partial pressure presents in the anode side suggests that the radical formation rate is limited by the amount of cross over hydrogen. It was found that the gas composition used in OCV test also affect the OCV decay behavior. Membrane can be severely degraded without a significant OCV decay under certain OCV hold conditions. Future study is necessary to help understand why there is an increase of membrane strength in the cathode side membrane when dilute H_2 and pure O_2 are used in the OCV test and exact role of Pt particles deposited in the membrane on membrane degradation.

We have also reported a significant synergistic interaction of mechanical stress and the rate of chemical degradation of PFSA membrane and the experimental results clearly show that a moderate tensile stress can increase the rate of radical-induced chemical decomposition of PFSA membrane by several times based on the total amount of fluoride emitted and the concentration of residual end groups (COOH) due to chain scission. We believe that, to the best of our knowledge, this is the first time that the existence of

166

interactions between mechanical stress and chemical reaction in PFSA membrane degradation has been studied and reported. The PFSA membrane degradation in the real fuel cell environment is extremely complicated. It is known that the mode and rate of membrane degradation is affected by temperature, RH, inlet gas composition, and so on. How these factors affect the membrane degradation reaction are still not fully understood, particularly the RH effect. Recent works from Ohma *et al.*[75, 100], as well as the authors[142], indicated that the platinum catalyst precipitated inside the membrane can impact the rate and loci of the membrane degradation. For ionomer membranes in a real polymer electrolyte membrane fuel cell, the RH not only affects the water contents in the membrane, but also the stress state of the membrane. Low RH can induce a bi-axial tensile stress[57], and the precipitated large platinum particles and crack and crazing due to the localized material degradation can introduce local stress concentration, further amplifying the local stress around the platinum particles. Such stress can potentially accelerate chemical decomposition of PFSA membranes locally, resulting in a local defect band and a mechanically weakened membrane. Further study is necessary to quantitatively understand the degree of acceleration of membrane degradation by mechanical stress.

We have developed a new constitutive model describing the finite deformation of the ionomer membrane for PEMFCs. The constitutive relationship is the nonlinear viscoelastic-viscoplastic and strain-rate, temperature, and hydration dependent. Micromechanism inspired Bergström-Boyce model was employed to capture the nonlinear viscoelastic behavior of the membrane and reptational dynamics inspired flow rule for viscous flow was used to describe the time dependent behavior. The proposed model can excellently predict the stress-strain behavior of vapor and liquid water equilibrated membranes, and rate-dependent mechanical behavior. The total stress is the summation of stresses in two different molecular networks (A & B) acting in parallel. Network A produce strain hardening/stiffening behavior resulting from molecular reorientation, entanglement, and locking up due to the large deformation and the network B generates the initially stiff response as well as the rate, temperature, and hydration dependence of initial flow. It was found that water softens the network B component and temperature affects significantly the material behavior of both network components.

After choosing the appropriate material parameters, the model accurately captured the mechanical behavior of ionomer membrane over a wide range of temperature and hydration level, implying that the deformation mechanisms we chosen well represent the material behavior of ionomer membrane. The future work will focus on improving the constitutive

168

model by incorporating the volumetric expansion of membrane material depending on the hydration level into the kinematic equation, and predicting the stress and strain responses of membranes subjected to complex loading conditions, such as creep, relaxation, and cyclic loading over the wide range of temperature and humidity conditions.

Fundamental understanding of polymer electrolyte membrane fuel cell (PEMFC) material degradation and performance variation under various operating conditions requires numerical models that accurately describe coupled electrochemical, charge, mass, and heat transport, as well the structural response (deformation) of fuel cells. An integrated model representing the charge and mass transport, electrochemical reactions, and structural response was attempted in this research based on a unified finite element modeling technique for analyzing these coupled phenomena. The authors developed a novel finite element modeling technique for a fuel cell assembly including multiphysics phenomena in fuel cells and structural mechanics models for fuel cell components. This model allows the investigation of the mechanical compression effects on gas transport properties and interfacial electrical contact properties of the components, and eventually fuel cell performance. It was found that cell compression affects GDL transport properties and contact resistance distribution, significantly altering the current density profile under the channel/land. Also, fuel cell models coupled with structural mechanics provided us a simulation tool for the prediction of

169

the in situ membrane stress subjected to various operating conditions, although we have no way of verifying the predicted stress magnitude at this time.   The simulation showed that the current density can induce different stress distribution patterns and stress levels in the membrane over the channel/land. The plan for the immediate future includes improving the current model by using more accurate material properties, more stable and efficient solution schemes, expanding the scope of the model study to three dimensional cases, and adding various degradation models for the catalysts and the membranes.

LIST OF REFERENCES

[1]   Rama P., Chen R., Andrews J., A review of performance degradation and failure modes for hydrogen-fuelled polymer electrolyte fuel cells, Proceedings of the I MECH E Part A: J of Power and Energy,   222(5), 421-41, 2008.

[2]   Wang C.-Y., Fundamental Models for Fuel Cell Engineering, Chemical Reviews,   104, 4727-66, 2004.

[3]   Solasi R. Mechanical Behavior, Modeling, Strength and Failure Analysis of Polyelectrolyte Membranes. Mechanical Engineering: University of Connecticut; 2008.

[4]   Borup R., Meyers J.P., Pivovar B., Scientific Aspects of Polymer Electrolyte Fuel Cell Durability and Degradation, Chemical Reviews,   107, 3904-51, 2007.

[5]   Kumbur E.C. Fundamental characterization of multi-phase transport in thin-film fuel cell diffusion media. Mechanical Engineering: Pennsylvania State University; 2007.

[6]   Stevens D.A., Hicks M.T., Haugen G.M., Dahn J.R., Ex Situ and In Situ Stability Studies of PEMFC Catalysts, Journal of The Electrochemical Society,   152(12), A2309-A15, 2005.

[7]   Zhang J., Tang Y., Song C., Zhang J., Wang H., PEM fuel cell open circuit voltage(OCV) in the temperature range of 23 to 120C, Journal of Power Sources,   163, 532-7, 2006.

[8]   Neyerlin K.C., Gasteiger H.A., Mittelsteadt C.K., Jorne J., Gu W., Effect of Relative Humidity on Oxygen Reduction Kinetics in a PEMFC, Journal of The Electrochemical Society,   152(6), A1073-A80, 2005.

[9]   Neyerlin K.C., Gu W., Jorne J., Clark A., Gasteiger H.A., Cathode Catalyst Utilization for the ORR in a PEMFC, Journal of The Electrochemical Society,   154(2), B279-B87, 2007.

[10]   Williams M.V., Kunz H.R., Fenton J.M., Analysis of Polarization Curves to Evaluate Polarization Sources in Hydrogen/Air PEM Fuel Cells, Journal of The Electrochemical Society,   152(3), A635-A44, 2005.

[11]   Wu J., Yuan X.Z., Martin J.J., Wang H., Zhang J., Shen J., Wu S., Merida W., A review of PEM fuel cell durability: Degradation mechanisms and mitigation strategies, Journal of Power Sources,   184, 104-19, 2008.

[12]   Yu P.T., Gu W., Makharia R., Wagner F.T., Gasteiger H.A. The impact of carbon stability on PEM fuel cell startup and shutdown voltage degradation,. 210th ECS meeting, Cancun, Mexico: 2006; 2006.

[13]   The US Department of Energy (DOE) Hydrogen R&D Plan, 2007.

[14]   Borup R., Davey J., Wood D., Garzon F., Inbody M., Guidry D., PEM fuel cell durability, DOE Hydrogen Program, FY 2004 Progress Report, 2004.

[15]   Frisk J., Boand W., Hicks M., Kurkowski M., Atanasoski R., Schmoeckel A. Fuel Cell Seminar San Antonio, TX, USA: 2004; 2004.

[16]   Davies D.P., Adcock P.L., Turpin M., Rowen S.J., Stainless steel as a bipolar pate material for solid polymer fuel cells, Journal of Power Sources,   86, 237, 2000.

[17]   Yoon W., Huang X., Fazzino P., Reifsnider K.L., Akkaoui M.A., Evaluation of coated metallic bipolar plates for polymer electrolyte membrane fuel cells, Journal of Power Sources,   179, 265-73, 2008.

[18]   Turner J.A., Wang H. Corrosion protection of Metallic Bipolar Plates for Fuel cells. DOE   Annual Progress Report; 2005.

[19]   Brady M.P., Weisbrod K., Paulauskas I., Buchanan R.A., More K.L., Wang H., Wilson M., Garzon F., Walker L.R., Preferential thermal nitridation to form pin-hole free Cr-nitirides to protect proten exchange membrane fuel cell metallic bipolar plates, Scripta Materialia,   50, 1017-22, 2004.

[20]   Fleury E., Jayaraj J., Kim C.H., Seok H.K., Kim K.Y., Kim J.B., Fe-based amorphous alloys as bipolar plates for PEM fuel cell, Journal of Power Sources,   159, 34-7, 2006.

[21]   Paik C.H., Jarvi T.D., O'Grady W.E., Extent of PEMFC Cathode Surface OXidation by Oxygen and Water Measured by CV, Electrochemical and Solid-State Letters,   7(4), A82-A4, 2004.

[22]   Ferreira P.J., la O' G.J., Shao-Horn Y., Morgan D., Makharia R., Kocha S., Gasteiger H.A., Instability of Pt/C Electrocatalysts in Proton Exchange Membrane Fuel Cells, Journal of The Electrochemical Society, 152(11), A2256-A71, 2005.

[23]   Wang X., Kumar R., Myers D.J., Effect of Voltage on Platinum Dissolution, Electrochemical and Solid-State Letters,   9(5), A225-A7, 2006.

[24]   Paik C.H., Saloka G.S., Graham G.W., Influence of Cyclic Operation on PEM Fuel Cell Catalyst Stability, Electrochemical and Solid-State Letters,   10(2), B39-B42, 2007.

[25]   Xu H., Kunz R., Fenton J.M., Investigation of Platinum Oxidation in PEM Fuel Cells at Various Relative Humidities, Electrochemical and Solid-State Letters,   10(1), B1-B5, 2007.

[26]   Darling R.M., Meyers J.P., Mathematical Model of Platinum Movement in PEM Fuel Cells, Journal of The Electrochemical Society,   152(1), A242-A7, 2005.

[27]   Yasuda K., Taniguchi A., Akita T., Ioroi T., Zyun S., Platinum dissolution and deposition in the polymer electrolyte membrane of a PEM fuel cell as studied by potential cycling, Physical Chemistry Chemical Physics, 8(746-752),   2005.

[28]   Curtin D.E., Lousenberg R.D., Henry T.J., Tangeman P.C., Tisack M.E., Advanced materials for improved PEMFC performance and life, Journal of Power Sources,   131, 41-8, 2004.

[29]   Schmittinger W., Vahidi A., A review of the main parameter influencing long-term performance and durability of PEM fuel cells, Journal of Power Sources,   180, 1-14, 2008.

[30]   Stanic V., Braun J., Hoberecht M. Durability of membrane electrode assemblies(MEAs) in PEM fuel cells operated on pure hydrogen and oxygen. 1st International Energy Conversion Engineering Conference (IECEC), Portsmouth, Virginia, Aug. 17-21: 2003; 2003.

[31]   Zhang J., Xie Z., High temperature PEM fuel cells, Journal of Power Sources,   160, 872-91, 2006.

[32]   Endoh E., Terazono S., Widjaja H., Takimoto Y., Degradation Study of MEA for PEMFCs under Low Humidity Conditions, Electrochemical and Solid-State Letters,   7(7), A209-A11, 2004.

[33]   Endoh E., Progress of Highly Durable MEA for PEMFC Under High Temperature and Low Humidity Conditions, ECS Transactions,   12(1), 41-50, 2008.

[34]   Cipollini N.E., Chemical Aspects of Membrane Degradation, ECS Transactions,   11(1), 1071-82, 2007.

172

[35] Young S.K., Trevino S.F., Beck Tan N.C., Small Angle Neutron Scattering Investigation of Structural Changes in Nafion Membranes Induced by Swelling with Various Solvents, Journal of Polymer Science Part B, Polymer Physics, 40(387-400), 2002.

[36] Gebel G., Lambard J., Small-Angle Scattering Study of Water-Swollen Perfluorinated Ionomer Membranes, Macromolecules, 30, 7914-20, 1997.

[37] Marx C.L., Caulfield D.F., L C.S., Morphology of Ionomers, Macromolecules, 6(3), 344-53, 1973.

[38] MacKnight W.J., Taggart W.P., Stein R.S., A model for the structure of ionomer, Journal of Polymer Science Part C, 45, 113, 1974.

[39] Elliott J.A., Hanna S., Elliott A.M., Cooley G.E., Interpretation of the Small-Angle X-ray Scattering from Swollen and Oriented Perfluorinated Ionomer Membranes, Macromolecules, 33, 4161-71, 2000.

[40] Hsu W.Y., Gierke T.D., Ion transport and clustering in nafion perfluorinated membranes, Journal of Membrane Science, 13(3), 307-26, 1983.

[41] Gebel G., Moore R.B., Small-Angle Scattering Study of Short Pendant Chain Perfuorosulfonated Ionomer Membranes, Macromolecules, 33, 4850-5, 2000.

[42] Gebel G., Structural evolution of water swollen perfluorosulfonated ionomers from dry membrane to solution, Polymer, 41, 5829-38, 2000.

[43] van der Heijden P.C., Rubatat L., Diat O., Orientation of Drawn Nafion at Molecular and Mesoscopic Scales, Macromolecules, 37, 5327-36, 2004.

[44] Schmidt-Rohr K., Chen Q., Parallel cylinderical water nanochannels in Nafion fuel cell membrane, Nature materials, 7, 75-83, 2008.

[45] Mauritz K.A., Moore R.B., State of Understanding of Nafion, Chemical Reviews, 104, 4535-85, 2004.

[46] Cable K.M., Mauritz K.A., Moore R.B., Anisotropic Ionic Conductivity in Uniaxially Oriented Perfluorosulfonate Ionomers, Chem Mater, 7, 1601-3, 1995.

[47] James P.J., Elliott J.A., Mcmaster T.J., Newton J.M., Elliott A.M., Hydration of Nafion studied by AFM and X-ray scattering, Journal of Materials Science, 35, 5111-9, 2000.

[48] Schnable W. Polymer degradation: Principles and Practical Applications. Hanser International; 1981.

[49] Huang X., Solasi R., Zou Y., Feshler M., Reifsnider K., Condit D., Burlatsky S., Madden T., Mechanical Endurance of Polymer Electrolyte Membrane and PEM Fuel Cell Durability, Journal of Polymer Science: Part B, 44, 2346-57, 2006.

[50] Huang X., Rodgers M., Yoon W., Bo L., Mohajeri N., Mechanical Degradation Behavior of Recast Composite PFSA Membrane and Nafion N112 Membrane under OCV Condition, ECS Transactions, 16(2), 1573-9, 2008.

[51] Tang H., Peikang S., Jiang S.P., Wang F., Pan M., A degradation study of Nafion proton exchange membrane of PEM fuel cells, Journal of Power Sources, 170, 85-92, 2007.

[52] Inaba M., Kinumoto T., Kiriake M., Umebayashi R., Tasaka A., Ogumi Z., Gas crossover and membrane degradation in polymer electrolyte fuel cells, Electrochemica Acta, 51(5746-5653), 2006.

173

[53] Sodaye H.S., Pujari P.K., Goswami A., Manohar S.B., Temperature dependent positron annihilation studies in Nafion-117 polymer, Radiation Physics and Chemistry, 58, 567-70, 2000.

[54] Sodaye H.S., Pujari P.K., Goswami A., Manohar S.B., Probing the Microstructure of Nafion-117 Using Positron Annihilation Spectroscopy, Journal of Polymer Science Part B, Polymer Physics, 35(5), 771-6, 1996.

[55] Sethuraman V.A., Weidner J.W., Haug A.T., Motupally S., Protsailo L.V., Durability of Perfluorosulfonic Acid and Hydrocarbon Membranes:Effect of Humidity and Temperature, Journal of The Electrochemical Society, 155(2), B119-B24, 2008.

[56] Doi M., Edwards S.F. The Theory of Polymer Dynamics. New York: Oxford University Press 1986.

[57] Solasi R., Zou Y., Huang X., Reifsnider K.L., Condit D., On mechanical behavior and in-plane modeling of constrained PEM fuel cell membranes subjected to hydration and temperature cycles, Journal of Power Sources, 167, 366-77, 2008.

[58] Majsztrik P.W., Bocarsly A.B., Benziger J.B., An instrument for environmental control of vapor pressure and temperature for tensile creep and other mechanical property measurements, Review of Scientific Instruments, 78, 103904, 2007.

[59] Bauer F., Denneler S., Willert-Porada M., Influence of Temperatue and Humidity on the Mechanical Properties of Nafion 117 Polymer Electrolyte Membrane, Journal of Polymer Science Part B, Polymer Physics, 43, 786-95, 2005.

[60] Liu W., Zuckerbrod D., In situ Detection of Hydrogen Peroxide in PEM Fuel Cells, Journal of The Electrochemical Society, 152(6), A1165-A70, 2005.

[61] Qiao J., Saito M., Hayamizu K., Okada T., Degradation of Perfluorinated Ionomer Membranes for PEM Fuel Cells during Processing with H2O2, Journal of The Electrochemical Society, 153(6), A967-A74, 2006.

[62] Mittal V.O., Kunz H.R., Fenton J.M., Is H2O2 involved in the Membrane Degradation Mechanism in PEMFC, Electrochemical and Solid-State Letters, 9(6), A299-A302, 2006.

[63] Pozio A., Silva R.F., De Francesco M., Giorgi L., Nafion degradation in PEFCs from end plate iron contamination, Electrchimica Acta, 48, 1543-9, 2003.

[64] Sethuraman V.A., Weidner J.W., Haug A.T., Motupally S., Protsailo L.V., Hydrogen Peroxide Fromation Rates in a PEMFC Anode and Cathode, Journal of Electrochemical Society, 155(1), B50-B7, 2008.

[65] Bi W., Gray G.E., Fuller T.F., PEM Fuel Cell Pt/C Dissolution and Deposition in Nafion Electrolyte, Electrochem Solid-State Lett, , 10(5), B101-B4, 2007.

[66] Panchenko A., Dilger H., Kerres J., Hein M., Ullrich A., Kaz T., Roduner E., In-situ spin trap electron paramagnetic resonance study of fuel cell processes, PCCP, 6, 2891-4, 2004.

[67] Teranishi K., Kawata K., Tsushima S., Hirai S., Degradation Mechanism of PEMFC under Open Circuit Operation, Electrochemical and Solid-State Letters, 9(10), A475-A7, 2006.

[68] Mittal V.O., Kunz R., Fenton J.M., Membrane Degradation Mechanisms in PEMFCs, Journal of The Electrochemical Society, 154(7), B652-B6, 2007.

174

[69]   Yu J., Matsuura T., Yoshikawa Y., Islam M.N., Hori M., Lifetime behavior of a PEM fuel cell with low humidification of feed stream, PhysChemChemPhys,   7, 373-8, 2005.

[70]   Wilkinson D.P., St-Pierre J. Handbook of Fuel Cells:Fundamentals Technology, and Applications. Wiley; 2003.

[71]   Kinumoto T., Inaba M., Nakayama Y., Ogata K., Umebayashi R., Tasaka A., Iriyama Y., Abe T., Ogumi Z., Durability of perfluorinated ionomer membrane against hydrogen peroxide, Journal of Power Sources,   158, 1222-8, 2005.

[72]   Zhao H., Huang X., Solasi R., Yoon W., Weiss R., Fundamental study of PFSA membrane degradation in Fenton's reagent, In preparation,   2008.

[73]   Xie T., Hayden C.A., A kinetic model for the chemical degradation of perfluorinated sulfonic acid ionomers: Weak end groups versus side chain cleavage, Polymer,   48, 5497-506, 2007.

[74]   Gowariker V.R., Viswanathan N.V., Sreedhar J. Polymer Science. New Age International 2003.

[75]   Ohma A., Suga S., Yamamoto S., Shinohara K., Membrane Degradation Behavior during Open-Circuit Voltage Hold Test, Journal of The Electrochemical Society,   154(8), B757-B60, 2007.

[76]   Vogel B., Aleksandrova E., Mitov S., Krafft M., Dreizler A., Kerres J., Hein M., Roduner E., Observation of Fuel Cell Membrane Degradation by Ex Situ and In Situ Electron Paramagnetic Resonance, Journal of The Electrochemical Society,   155(6), B570-4, 2008.

[77]   Hommura S., Kawahara K., Shimohira T., Teraoka Y., Development of a Method for Clarifying the Perfluorosulfonated Membrane Degradation Mechanism in a Fuel Cell Environment, Journal of The Electrochemical Society,   155(1), A29-A33, 2008.

[78]   Endoh E., Hommura S., Terazono S., Widjaja H., Anzai J., Degradation Mechanism of the PFSA Membrane and Influence of Deposited Pt in the Membrane, ECS Transactions,   11(1), 1083-91, 2007.

[79]   Kundu S., Fowler M., Simon L.C., Abouatallah R., Reversible and irreversible degradation in fuel cells during Open Circuit Voltage durability testing, Journal of Power Sources,   182, 254-8, 2008.

[80]   Delaney W.E., Liu W.K., The Use of FTIR to Analyze Ex-situ and In-situ Degradation of Perfluorinated Fuel Cell Ionomer, ECS Transactions,   11(1), 1093-104, 2007.

[81]   Inaba M., Kinumoto T., Kiriake M., Umebayashi R., Tasaka A., Ogumi Z., Gas crossover and membrane degradation in polymer electrolyte fuel cells, Electrochimica Acta,   51(26), 5746-53, 2006.

[82]   Mittal V.O., Russell Kunz H., Fenton J.M., Is H2O2 involved in the membrane degradation mechanism in PEMFC?, Electrochemical and Solid-State Letters,   9(6),   2006.

[83]   Hu?bner G., Roduner E., EPR investigation of HO· radical initiated degradation reactions of sulfonated aromatics as model compounds for fuel cell proton conducting membranes, Journal of Materials Chemistry,   9(2), 409-18, 1999.

[84]   Zhang L., Mukerjee S., Investigation of durability issues of selected nonfluorinated proton exchange membranes for fuel cell application, Journal of the Electrochemical Society,   153(6),   2006.

[85]   Kinumoto T., Inaba M., Nakayama Y., Ogata K., Umebayashi R., Tasaka A., Iriyama Y., Abe T., Ogumi Z., Durability of perfluorinated ionomer membrane against hydrogen peroxide, Journal of Power Sources, 158(2 SPEC. ISS.), 1222-8, 2006.

[86]   Qiao J., Saito M., Hayamizu K., Okada T., Degradation of perfluorinated ionomer membranes for PEM fuel cells during processing with H2 O2, Journal of the Electrochemical Society,   153(6),   2006.

[87]   Liu W., Zuckerbrod D., In situ detection of hydrogen peroxide in PEM fuel cells, Journal of the Electrochemical Society,   152(6),   2005.

[88]   Panchenko A., Dilger H., Mo?ller E., Sixt T., Roduner E., In situ EPR investigation of polymer electrolyte membrane degradation in fuel cell applications, Journal of Power Sources,   127(1-2), 325-30, 2004.

[89]   Collier A., Wang H., Zi Yuan X., Zhang J., Wilkinson D.P., Degradation of polymer electrolyte membranes, International Journal of Hydrogen Energy,   31(13), 1838-54, 2006.

[90]   Healy J., Hayden C., Xie T., Olson K., Waldo R., Brundage M., Gasteiger H., Abbott J., Aspects of the chemical degradation of PFSA ionomers used in PEM fuel cellsx, Fuel Cells,   5(2), 302-8, 2005.

[91]   Xie J., Wood D.L., Wayne D.M., Zawodzinski T.A., Atanassov P., Borup R.L., Durability of PEFCs at High Humidity Conditions, Journal of The Electrochemical Society,   152(1), A104-A13, 2005.

[92]   Iojoiu C., Guilminot E., Maillard F., Chatenet M., Sanchez J.Y., Claude E., Rossinot E., Membrane and Active Layer Degradation Following PEMFC Steady-State Operation, Journal of The Electrochemical Society, 154(11), B1115-B20, 2007.

[93]   Guilminot E., Corcella A., Chatenet M., Maillard F., Charlot F., Berthome G., Iojoiu C., Sanchez J.Y., Rossinot E., Claude E., Membrane and Active Layer Degradation upon PEMFC Steady-State Operation, Journal of The Electrochemical Society,   154(11), B1106-B14, 2007.

[94]   Reiser C.A., Bregoli L., Patterson T.W., Yi J.S., Yang D., Perry M.L., Jarvi T.D., A Reverse-Current Decay Mechanism for Fuel Cells, Electrochemical and Solid-State Letters,,   8(6), A273-A6, 2005.

[95]   Yasuda K., Taniguchi A., Akita T., Ioroi T., Siroma Z., Platinum dissolution and deposition in the polymer electrolyte membrane of a PEM fuel cell as studied by potential cycling, PCCP,   8(746-752),   2005.

[96]   Darling R.M., Meyers J.P., Kinetic Model of Platinum Dissolution in PEMFCs, Journal of The Electrochemical Society,   150(11), A1523-A7, 2003.

[97]   Guilminot E., Corcella A., Charlot F., Maillard F., Chatenet M., Detection of Pt+ Ions and Pt Nanoparticles Inside the Membrane of a Used PEMFC, Journal of The Electrochemical Society,   154(1), B96-B105, 2007.

[98]   Patterson T.W., Darling R.M., Damage to the Cathode Catalyst of a PEM Fuel Cell Caused by Localized Fuel Starvation, Electrochemical and Solid-State Letters,   9(4), A183-5, 2006.

[99]   Sompalli B., Litteer B.A., Gu W., Gasteiger H.A., Membrane Degradation at Catalyst Layer Edges in PEMFC MEAs, Journal of The Electrochemical Society,   154(12), B1349-B57, 2007.

[100]   Ohma A., Yamamoto S., Shinohara K., Membrane degradation mechanism during open-circuit voltage hold test, Journal of Power Sources,   182, 39-47, 2008.

[101]   Beyer M.K., Clausen-Schaumann H., Mechanochemistry: The Mechanical Activation of Covalent Bonds, Chemical Reviews,   105(8), 2921-44, 2005.

[102]   Butyagin P.Y., Kinetics and Nature of Mechanochemical Reactions, Russian Chemical Reviews, 40(11), 901-11, 1971.

[103]   Zarkhin L.S., Sheverstov S.V., Panfilovich N.V., Manevich L.I., Mechanodegradation of Polymers. The method of molecular dynamics, Russian Chemical Reviews,   58(4), 381, 2989.

[104]   Endoh E., Development of Highly Durable PFSA Membrane and MEA for PEMFC Under High Temperature and Low Humidity Conditions, ECS Transactions,   16(2), 1229-40, 2008.

[105]   Meijer H.E.H., Govaert L.E., Mechanical performance of polymer systems:The relation between structure and properties, Progress in Polymer Science,   30, 915-38, 2005.

[106]   Rubinstein M., Colby R. Polymer Physics. Oxford; 2003.

[107]   Mocherla K.K.R. Stress-strain behavior of oriented crystalline polymers: a molecular approach by dynamic infrared techniques. Material science and Engineering: University of Utah; 1976.

[108]   Gierke T.D., Munn G.E., Wilson F.C., The morphology in nafion perfluorinated membrane products, as determined by wide and small angle x-ray studies, Journal of Polymer Science: Polymer Physics Edition, 19(11), 1687-704, 1981.

[109]   Haward R.N., Thackray G., The Use of a Mathematical Model to Describe Isothermal Stress-Strain Curves in Glassy Thermoplastics, Proceedings of the Royal Society of London Series A,   302(1471), 453-72, 1968.

[110]   Bergstrom J.S., Boyce M.C., Constitutive modeling of the large strain time-dependent behavior of elastromers, JMechPhysSolids,   46(5), 931-54, 1998.

[111]   Freunberger S.A., Reum M., Evertz J., Wokaun A., Buchi F., N, Measuring the Current Distribution in PEFCs with Sub-millimeter Resolution, J of the Electrochemical Society,   153(11), A2158-A65, 2006.

[112]   Hottinen T., Himanen O., Karvonen S., Nitta I., Inhomogeneous compression of PEMFC gas diffusion layer. Part2. Modeling the effect, Journal of Power Sources,   171, 113-21, 2007.

[113]   Su Z.Y., Liu C.T., Chang H.P., Li C.H., Huang K.J., Sui P.C., A numerical investigation of the effects of compression force on PEM fuel cell performance, Journal of Power Sources,   183, 182-92, 2008.

[114]   Zhou Y., Lin G., Shih A.J., Hu S.J., Assembly pressure and membrane swelling in PEM fuel cells, Journal of Power Sources,   192, 544-51, 2009.

[115]   Atrazhev V.V., Timokhina E.N., Burlatsky S.F., Sultanov V.I., Madden T.H., Gummalla M., Direct Mechanism of OH Radicals Formation in PEM Fuel Cells, ECS Transactions,   6(25),   2008.

[116]   Madden T.H., Weiss D., Cipollini N., Condit D., Gummalla M., Burlatsky S.F., Atrazhev V.V., Degradation of Polymer-Electrolyte Membranes in Fuel Cells, ECS,   156(5), B657-B62, 2009.

[117]   Zhurkov S.N., Korsukov V.E., Atomic Mechanism of Fracture of Solid Polymers, Journal of Polymer Science:Polymer Physics Edition,   12, 385-98, 1974.

177

[118]   Yoon W., Huang X., Evidences of Stress-induced-Chemical degradation of Polymer Electrolyte Membrane for Fuel cells, Submitted, 2009.

[119]   Rodgers M.P., Agarwal R., Pearman B., Li B., Slattery D., Choi P., Mohajeri N., Bonville L., Kunz H.R., Fenton J.M., Accelerated Durability Testing of Perfluorosulfonic Acid MEAs for PEMFCs, ECS Transactions, 16(2), 1951-9, 2008.

[120]   Sugawara S., Maruyama T., Nagahara Y., Kocha S.S., Shinohra K., Tsujita K., Mitsushima S., Ota K.-i., Performance decay of proton-exchange membrane fuel cells under open circuit conditions induced by membrane decomposition, Journal of Power Sources, 187, 324-31, 2009.

[121]   Kuksenko V.S., Tamuzs V.P. Fracture micromechanics of polymer materials. Martinus Nijhoff 1981.

[122]   Kausch H.H. Polymer Fracture. Springer-Verlag Berlin Heidelberg; 1987.

[123]   Laporta M., Pegoraro M., Zanderighi L., Perfluorosulfonated membrane(Nafion) : FT-IR study of the state of water with increasing humidity, PhysChem ChemPhys, 1, 4619-28, 1999.

[124]   Ludvigsson M., Lindgren J., Tegenfeldt J., FTIR study of water in cast Nafion films, Electrochimica Acta 45, 2267-71, 2000.

[125]   Chen C., Levitin G., Hess D.W., Fuller T.F., XPS investigation of Nafion membrane degradation, Journal of Power Sources, 169, 288-95, 2007.

[126]   Hoare J.P., Rest Potentials in the Platinum-Oxygen-Acid System, ECS, 109(9), 858-65, 1962.

[127]   Struik L.C.E. Physical aging in amorphous polymers and other materials. Elsevier; 1978.

[128]   Coms F.D., The Chemistry of Fuel Cell Membrane Chemical Degradation, ECS Transactions, 16(2), 235-55, 2008.

[129]   Coms F.D., Liu H., Owejan J.E., Mitigation of Perfluorosulfonic Acid Membrane Chemical Degradation Using Cerium and Manganese Ions, ECS Transactions, 16(2), 1735-47, 2008.

[130]   Beyer K.M., Clausen-Schaumann H., Mechanochemistry: The Mechanical Activation of Covalent Bonds, Chemical Reviews, 105(8), 2921-044, 2004.

[131]   Aktah D., Frank I., Breaking Bonds by Mechanical Stress: When Do Electrons Decide for the Other Side?, Journal of American Chemical Society, 124, 3402-6, 2002.

[132]   Wiita A.P., Ainavarapu S.R.K., Huang H.H., Fernandez J.M., Force-dependent chemical kinetics of disulfide bond reduction observed with single-molecule techniques, Preceedings of the National Academy of Science, 103(19), 7222-7, 2005.

[133]   Beyer M.K., Coupling of Mechanical and Chemical Energy: Proton Affinity as a Function of External Force, Angew, Chem,Int Ed, 42, 4913-5, 2003.

[134]   Sohma J., Mechanochemistry of Polymers, Progress in Polym Science, 14(4), 451-596, 1989.

[135]   Zhurkov S.N., Kuksenko V.S., The micromechanics of polymer fracture, Internaltional Journal of Fracture, 11(4), 629-39, 1975.

[136]   Available at http://www.ozonelab.com/articles/004.htm. Available at http://www.ozonelab.com/articles/004.htm.

178

[137] DuPont, Dispersions Properties and Processing Guide, Technical bulletin.

[138] Lin J., Wycisk R., Pintauro P.N., Kellner M., Stretched Recast Nafion for Direct Methanol Fuel Cells, Electroand Solid-State Letters, 10(1), B19-B22, 2007.

[139] Silberstein M. Mechanics of Proton Exchange Membranes: Time,Temperature, and Hydration Dependence of the Stress-Strain Behavior of Persulfonated Polytetrafluorethylene. Mechanical Engineering: MIT; 2008.

[140] Ugural A. Mechanical Design: An Integrated Approach Mcgraw-Hill 2003.

[141] Kawano Y., Wang Y., Palmer R.A., R A.S., Stress-Strain Curves of Nafion Membranes in Acid and Salt Forms, Polim Cien Tecnol 12(2), 96-101, 2002.

[142] Yoon W., Huang X., Study of Polymer Electrolyte Membrane Degradation under OCV Hold using Bi-layer MEAs, J ElectrochemSoc, Reviewed and Accepted, 2009.

[143] Bergstrom J.S., Hilbert Jr L.B., A constitutive model for predicting the large deformation thermomechanical behavior of fluoropolymers, Mechanics of Materials 37, 899-913, 2005.

[144] Arruda E.M., Boyce M.C., A Three-Dimensional Constitutive Model For The Large Stretch Behavior of Rubber Elastic Materials, JMechPhysSolids, 41(2), 389-412, 1993.

[145] Vettegren V.I., Novak I.I., Friedland K.J., Overstressed interatomic bonds in stressed polymers, Internaltional Journal of Fracture, 11(5), 789-801, 1975.

[146] Korsukov V.E., Vettegren V.I., Novak I.I., Spectroscopic method of measuring the stresses at stress raisers in polymers, Polymer Mechanics, 6(1), 156-9, 1972.

[147] Vettegren V.I., Novak I.I., Determination of Atomic Stress Distribution in Stressed Polymers by Infrared Spectroscopy, Journal of Polymer Science:Polymer Physics Edition, 11, 2135-42, 1973.

[148] Kusoglu A., Karlsson A.M., Santare M.H., Cleghorn S., Johnson W.B., Mechanical response of fuel cell membranes subjected to a hygro-thermal cycle, Journal of Power Sources, 161, 987-96, 2006.

[149] Tang Y., Karlsson A.M., Santara M.H., Gilbert M., Cleghorn S., B J.W., An experimental investigation of humidity and temperature effects on the mechanical properties of perfluorosulfonic acid membrane, Materials Science and Engineering A, 425, 297-304, 2006.

[150] Majsztrik P.W., Bocarsly A.B., Benziger J.B., Viscoelastic Response of Nafion. Effects of Temperature and Hydration on Tensile Creep, Macromolecules, 41(24), 9849-62, 2008.

[151] Bograchev D., Gueguen M., Grandidier J.-C., Martemianov S., Stress and plastic deformation of MEA in fuel cells Stresses generated during cell assembly, Journal of Power Sources, 180, 393-401, 2008.

[152] Bograchev D., Gueguen M., Grandidier J.-C., Martemianov S., Stress and plastic deformation of MEA in running fuel cell, IntJHydrogen Energy, 33, 5703-17, 2008.

[153] Satterfield M.B., Benziger J.B., Viscoealstic Properties of Nafion at Elevated Temperature and Humidity, J of Polymer Science:Part B, 47, 11-24, 2009.

[154]   Tang Y., Santare M.H., Karlsson A.M., Cleghorn S., Johnson W.B., Stresses in Proton Exchange Membranes Due to Hygro-Thermal Loading, Journal of Fuel Cell Science and Technology, ASME,   3, 119-24, 2006.

[155]   Solasi R., Zou Y., Huang X., Reifsnider K., A time and hydration dependent viscoplastic model for polyelectrolyte membranes in fuel cells, Mech Time-Depend Mater,   12, 15-30, 2008.

[156]   Arruda E.M., Boyce M.C., Jayachandran R., Effects of strain rate, temperature and thermomechanical coupling on the finite strain deformation of glassy polymers, Mechanics of Materials,   19, 1993-212, 1995.

[157]   Raha S., Bowden P.B., Birefringence of plastically deformed poly(methyl methacrylate), Polymer, 13(4), 174-83, 1972.

[158]   Wool R.P., Polymer Entanglements, Macromolecules,   26, 1564-9, 1993.

[159]   de Gennes P.G. Scaling Concepts in Polymer Physics. Cornell University Press; 1979.

[160]   Capaldi F.M., Boyce M.C., Enhanced Mobility Accompanies the Active Deformation of a Glassy Amorphous Polymer, Physical Review Letters,   89(17), 175505, 2002.

[161]   Trevino S.F., Young S.K., Morphology and Morphological Changes Within Nafion Membranes Induced by Mechanical Orientation, Army Research Laboratory Report,   2002.

[162]   Barbi V., Funari S.S., Gehrke R., Scharnagl N., Stribeck N., Nanostructure of Nafion membrane material as a function of mechanical load studied by SAXS, Polymer,   44, 4853-61, 2003.

[163]   Boyce M.C., Socrate S., Llana P.G., Constitutive model for the finite deformation stress-strain behavior of poly(ethylene terephthalate) above the glass transition, Polymer,   41, 2000, 2000.

[164]   Bergstrom J.S., Boyce M.C., Large strain time-dependent behavior of filled elastomers, Mechanics of Materials,   32, 627-44, 2000.

[165]   Bergstrom J.S., Kurtz S.M., Rimnac C.M., Edidin A.A., Constitutive modeling of ultra-high molecular weight polyethylene under large-deformation and cyclic loading conditions, Biomaterials,   23, 2329-43, 2002.

[166]   Bergstrom J.S. Large Strain Time-Dependent Behavior of Elastomeric Materials. MIT; 1999.

[167]   Lee E.H., Elastic-Plastic deformation at finite strains, J of Appl Mech,   36, 1-6, 1969.

[168]   Moran B., Ortiz M., Shih C.F., Formulation of implicit finite element methods for multiplicative finite deformation plasticity, Int J Numer Methods Eng,   29, 483-514, 1990.

[169]   Dommelen J.A.W., Parks D.M., Boyce M.C., Brekelmans W.A.M., Baaijens F.P.T., Micromechanical modeling of the elasto-viscoplastic behavior of semi-crystalline polymers, Journal of the Mechanics and Physics of Solids,   51, 519-41, 2003.

[170]   Anand L., Gurtin M.E., A theory of amorphous solids underging large deformations, with appplication to polymeric glasses, Int J Solids and Structures,   40, 1465-87, 2003.

[171]   Gurtin M.E., Anand L., The decompostion F=FeFp, material symmetry, and plastic irrotationality for solids that are isotropic-viscoplastic or amorphous, Int J Plasticity,   21, 1686-719, 2005.

[172]   Khan A.S., Sujian H. Continuum theory of plasticity. John Wiley & Sons; 1995.

[173]   Boyce M.C., Weber G.G., Parks D.M., On the kinematics of finite strain plasticity, J Mech Phys Solids, 37(5), 647-65, 1989.

[174]   Hsu W.Y., Gierke T.D., Elastic Theory for Ionic Clustering in Perfluorinated Ionomers, Macromolecules,   15, 101-5, 1982.

[175]   Zou Y. Hygrothermal Mechanical Properties and Durability of Ionomer Membranes. Mechanical Engineering: Univ. of Connecticut; 2007.

[176]   Springer T.E., Zawodzinski T.A., Gottesfeld S., Polymer Electrolyte Fuel Cell Model, J ElectrochemSoc, 138(8), 2334-42, 1991.

[177]   Areias P., Matous K., Finite element formulation for modeling nonlinear viscoelastic elastomers, Comput Methods Appl Mech Engrg,   197, 4702-17, 2008.

[178]   DuPont, Nafion PFSA Membranes NRE211 and NRE-212 Product information.

[179]   Ames N.M. An Internal Variable Theory for Isotropic Visco-elastic-plastic Solids Mechanical Engineering: M.I.T; 2003.

[180]   Miehe C., Goktepe S., Diez J.M., Finite viscoplasticity of amorphous glassy polymers in the logarithmic strain space, InterJ of Solids and Structures,   46, 181-202, 2009.

[181]   Kundu S., Simon L.C., Fowler M., Grot S., Mechanical properties of Nafion electrolyte membranes under hydrated conditions, Polymer,   46, 11707-15, 2005.

[182]   Yoon W., Huang X., Study of Polymer Electrolyte Membrane Degradation under OCV Hold using Bi-layer MEAs, J of the Electrochemical Society,   Reviewed and accepted,   2009.

[183]   Kusoglu A., Karlsson A.M., Santare M.H., Cleghorn S., Johnson W.B., Mechanical behavior of fuel cell membranes under humidity cycles and effect of swelling anisotropy on the fatigue stresses, Journal of Power Sources,   170, 345-58, 2007.

[184]   Huang C., Liu Z.S., Mu D.Q., The Mechanical Changes in the MEA of PEM Fuel Cells due to Load Cycling, ECS Transactions,   16(2), 1987-96, 2008.

[185]   Escribano S., Blachot J.-F., Etheve J., Morin A., Mosdale R., Characterization of PEMFCs gas diffusion layers properties, Journal of Power Sources,   156, 8-13, 2006.

[186]   Lee C., Merida W., Gas diffusion layer durability under steady-state and freezing conditions, Journal of Power Sources,   164, 141-53, 2007.

[187]   Wang L., Liu H., Separate measurement of current density under the channel and the shoulder in PEM fuel cells, Journal of Power Sources,   180, 365-72, 2008.

[188]   Nitta I., Hottinen T., Himanen O., Mikkola M., Inhomogeneous compression of PEMFC gas diffusion layer:Part 1. Experimental, Journal of Power Sources,   171(1), 26-36, 2007.

[189]   Bograchev D., Gueguen M., Grandidier J.-C., Martemianov S., Stress and Plastic deformation of MEA in running fuel cells International J of Hydrogen Energy,   33, 5703-17, 2008.

[190]   Zhou P., Wu C.W., Ma.G.J, Contact resistance prediction and structure optimization of bipolar plates, Journal of Power Sources,   159, 1115-22, 2006.

[191]   Lai X., Liu D.a., Peng L., Ni J., A mechanical-electrical finite element method model for prediction contact resistance between bipolar plate and gas diffusion layer in PEM fuel cells, Journal of Power Sources, 182, 153-9, 2008.

[192]   Nitta I., Himanen O., Mikkola M., Contact resistance between gas diffusion lasyer and catalyst layer of PEM fuel cell, Electrochemistry Communications,   10, 47-51, 2008.

[193]   Ihonen J., Mikkola M., Lindbergh G., Flooding of Gas Diffusion Backing in PEFCs, J of the Electrochemical Society,   151(8), A1152-A61, 2004.

[194]   Nitta I., Himanen O., Mikkola M., Thermal Conductivity and Contact Resistance of Compressed Gas Diffusion Layer, Fuel Cells,   8(2), 111-9, 2008.

[195]   Kleemann J., Finsterwalder F., Tillmetz W., Characterisation of mechanical behaviour and coupled electrical properties of polymer electrolyte membrane fuel cell gas diffusion layers, Journal of Power Sources, 190, 92-102, 2009.

[196]   Lai Y.-H., Rapaport P.A., Ji C., Kumar V., Channel intrusion of gas diffusion media and the effect on fuel cell performance, Journal of Power Sources,   184, 120-8, 2008.

[197]   Sadiq Al-Baghdadi M.A.R., Shahad Al-Janabi H.A.K., Effect of operating parameters on the hygro-thermal stresses in proton exchange membranes of fuel cellsE, International J of Hydrogen Energy,   32, 4510-22, 2007.

[198]   Yoon W., Huang X., A Nonlinear Viscoelastic-Viscoplastic Constitutive Model for Ionomer Membrane in Polymer Electrolyte Membrane Fuel Cell (PEMFC), In Progress,   2009.

[199]   Berg P., Promislow K., Pierre J.S., Stumper J., Wetton B.R., Water management in PEM Fuel Cells, J of the Electrochemical Society,   151(3), A341-A53, 2004.

[200]   Serincan M.F., Yesilyurt S., Transient Analysis of Proton Electrolyte Membrane Fuel Cells at Start-Up and Failure, Fuel Cells,   2(118-127),   2007.

[201]   Gostick J.T., Fowler M.W., Pritzker M.D., Ioannidis M.A., Behra L.M., In-Plane and through-plane gas permeability of carbon fiber electrode backing layers, Journal of Power Sources,   162, 228-38, 2006.

[202]   Tomadakis M.M., Robertson T.J., Viscous Permeability of Random Fiber Structures : Comparison of Electrical and Diffusional Estimates with Experimental and Analytical Results, Journal of Composite Materials, 39(2), 163-88, 2005.

[203]   Stockie J.M., Promislow K., Wetton B.R., A finite volume method for multicomponent gas transport in a porous fuel cell electrode, Int J Numerical Methods In Fluid,   00, 1-35, 2001.

[204]   Bird R.B., Stewart W.E. Transport Phenomena. New York: Wiley; 2002.

[205]   Mishra V., Yang F., Pitchumani R., Measurement and Prediction of Electrical Contact Resistance Between Gas Diffusion Layers and Bipolar Plate for Applications to PEM Fuel Cells, Journal of Fuel Cell Science and Technology,   1(1), 2-9, 2004.

[206]   Lin G., Nguyen T.V., A Two-Dimensional Two-Phase model of a PEM Fuel Cell, J of the Electrochemical Society,   153(2), A372-A82, 2006.

[207]   Lin G., He W., Nguyen T.V., Modeling Liquid Water Effects in the Gas Diffusion and Catalyst Layers of the Cathode of a PEM Fuel Cell, J of the Electrochemical Society,   151(12), A1999-A2004, 2004.

[208]   Wang Y., Wang C.-Y., A Nonisothermal, Two-Phase Model for Polymer Electrolyte Fuel Cells, J of the Electrochemical Society,   153(6), A1193-A200, 2006.

[209]   He W., Yi J.S., Nguyen T.V., Two-Phase Flow Model of the Cathode of PEM Fuel Cells Using Interdigitated Flow Fields, Matls, Inter, and ElectrochPhen,   46(10), 2053, 2000.

[210]   Arruda E.M., Boyce M.C., Jayachandran R., Effects of strain rate, temperature and thermomechanical coupling on the finite strain deformation of glassy polymers, Mechanics of Materials,   19, 193-212, 1995.

[211]   Bergstrom J.S., Hillbert L.B., A constitutive model for prediction the large deformation thermomechanical behavior of fluoroplymers, Mechanics of Materials,   37(8), 899-913, 2005.

[212]   Ge J., Higier A., Liu H., Effect of gas diffusion layer compression on PEM fuel cell performance, Journal of Power Sources,   159(922-927),   2006.

[213]   Reum M., Freunberger S.A., Wokaun A., Buchi F., N, Measuring the Current Distribution with Sub-Millimeter Resolution in PEFCs, J of the Electrochemical Society,   156(3), B301-B10, 2009.

[214]   Bazylak A., Sinton D., Liu Z.-S., Djilali N., Effect of compression on liquid water transport and microstructure of PEMFC gas diffusion layers, J of Power Sources,   163, 784-92, 2007.

[215]   Wang X., Song Y., Zhang B., Experimental study on clamping pressure distribution in PEM fuel cells, J of Power Sources,   179, 305-9, 2008.

183